Using Crustal Thickness Modeling to study Mars' Crustal and Mantle Structures

Karina Kawing Cheung

Thesis submitted to the Faculty of the Virginia Polytechnic Institute and State University
in partial fulfillment of the requirements for the degree of

Master of Science
In
Geosciences

Scott D. King, Chair
John A. Hole
Robert J. Tracy

May 7th, 2012
Blacksburg, Virginia

Keywords: Mars, gravitational potential, topography, crustal and mantle structures, density, isostacy, modeling

Using Crustal Thickness Modeling to study Mars' Crustal and Mantle Structures

Karina Kawing Cheung

ABSTRACT

Mars has an intriguing topographic and crustal dichotomy that divides the planet into a Northern Hemisphere and a Southern Hemisphere. The biggest question is to understand how this dichotomy was formed and what are the implications to the interior evolution of the planet. This study uses topography and gravity data obtained from the Mars Global Surveyor satellite observations in a crustal thickness program written by Mark Wieczorek. This program uses an algorithm that incorporates spherical harmonic coefficients of topography and gravity and calculates the Moho topography given a set of user-input parameters; it also generates crustal thickness maps. I modified the code to produce gravity misfit maps for interpretation of crustal and mantle structures.

Experiments were performed to test various parameters in the program and observe their effects on the resulting crustal thickness. The algorithm assumes a uniform density for the crust and mantle. A crustal density of 2900 kg/m^3 and a mantle density of 3500 kg/m^3 were used to represent a basaltic crust and an olivine mantle, derived from petrologic studies of meteorites assumed to have originated from Mars. As the crustal density is held constant while varying the mantle density (and vice versa), it is the total density contrast that changes the crustal thickness; the larger the density contrast, the smaller the crustal thickness.

Higher-order terms in the algorithm equation were also tested. Results show that the higher-order terms do not affect the overall crustal thickness by much thus are negligible. In modeling the crustal thickness, a minimum crustal thickness of 5 km was used to anchor the topography so that the resulting crust do not have negative or zero thickness. By using this minimum thickness, there is about 40 km thickness difference between the Northern Lowlands and the Southern Highlands.

Crustal thickness and gravity misfit maps show a plume-like track from the South Pole to the Tharsis Rise region, consistent with the theory proposed by Zhong (2010) on a mantle plume track. A ring-like feature in the misfit maps resembles a regional-scale impact crater that may have created the Borealis Basin in the Northern Lowlands, also consistent with current hypotheses about the formation of the Northern Lowlands.

A result of Airy isostacy (with only the linear terms in topography) is that the Moho topography will be related to the surface topography with a scale factor depending on the crust-mantle density contrast. Isostatic studies here reveal that Mars may be more or less isostatic at spherical harmonic degree-1 wavelength scale where as at spherical harmonic degree-2, an impact-like structure is revealed just east of the Tharsis Rise region, suggesting a possible impact. Due to the non-uniqueness of gravity, these models have a limited constraint on the crustal thickness and further studies involving a seismometer are needed to get a more precise look into Mars' interior.

ACKNOWLEDGEMENTS

Most importantly, I'd like to thank my advisor, Dr. Scott King. Scott: thank you for everything; if it was not for you, I would not have made it this far to complete my master's in geophysics. Thanks for teaching me how to "be a master" of my own project and let me work on a Mars project, when our department is mostly focused on topics on the Earth. I have always loved planetary science, so thank you for helping me realize that dream and made me a junior member of the planetary community when I didn't think I was one. Before the project, I had thought I was just another grad student working on an out-of-this-world project, but by the end, I realized that no matter how small a part, I have become a junior scientist. I thank you for all this time in mentoring me, taking out extra time to help me with gravity theory (even though you're probably sick of that by now). I hope we will keep in touch in the future.

I want to thank my committee members, Dr. John Hole and Dr. Robert Tracy. Not only have you guys helped by reading my thesis and providing very interesting and constructive suggestions during my defense, but for being great professors. I thoroughly enjoyed taking and learning from your classes when I was an undergrad in this department, and it is so nice that I got to have the two of you on my master's thesis committee to see me through to finish my graduate degree. Although I may not necessarily remember everything I learned in those classes (though I will never forget the field work in using a GPR or the trip to Mount Rogers), your upbeat and inspiring personalities will always remind me that geology is a lot of fun, even when there are bad days. This brings me to thank Dr. Nancy Ross. Nancy: I would not be here at all or starting from 9 years ago if it wasn't for you. I took your Resources Geology class and fell in love with geology and thus leading me to getting my bachelor's and now a master's degree in this field. Whether my passion for planetary science or resources and energy industry becomes my career path, I know getting a degree in geosciences will always serve me well in either field.

Given that our department does not have a planetary group, I like to thank Dr. Robert Lowell, Kate Craft, Pavithra Sekhar, and Tannistha Maiti for our own planetary group meetings. We are a very small tight-knit support group that has limited resources in the field we work in and I'm grateful for your constant support and feedback on planetary topics. Kate: you are truly a great role model, juggling graduate school, working on a Mars project, and balancing two kids at the same time. You're one of my superheroes that remind me we women scientists can indeed have it all! Pavithra: your friendship is priceless and your cheerful, fun-filled personality always remind me to take a step back and breathe and relaxed, that there is more to life than grad school when things get tough. Tannistha: you are the absolute greatest officemate and friend I could ever ask for. Although you do not work in planetary, your support and friendship has gotten me through tough times as well as through joyful times. I thank all of you and the graduate student colleagues especially Aida Farough, Lindsay Kolbus, Cable Warren, all geophysics friends in the 1070 and 1068 offices, geology friends in 5050 for all your support. Without you guys, I would not have come this far to finish.

There are not enough words in the English language that are synonyms to the words "thank you" for Ms. Connie Lowe. Throughout my undergraduate and graduate

years here in the department, you have gone above and beyond to help me, not only in paperwork or anything pertaining to academics, but your unfailing support and friendship always kept me grounded and taught me how to be a strong and successful person, not just a student. The many things we all go through in graduate school have taught us so much more about life, rather than the actual academics. I am truly humbly yours, grateful for your guidance and support. I cannot thank you enough.

No graduate student can live on ramen forever for the course of their graduate program. I want to thank Ms. Linda Bland, Ms. Ellen Mathena, and Ms. Mary McMurray for being awesome administrative staff that helped me get my paycheck, let us know when there's a speaker luncheon, and helped with office equipment (the copier is jammed again?). The department would be in a total mess if it weren't for you ladies.

I would also like to thank NASA for the funding of this research project and the Department of Geosciences's GSAC committee for extra funding, so that I could complete my project. I want to extend my gratitude to Dr. Maddy Schreiber, Dr. Fred Read, for their always supportive, inspiring, and cheery personalities that makes me feel proud to be part of this department. You have always lent an ear as understanding mentors, someone who I could go to for advice and when I needed a friend.

Last but not least, and certainly the most important people in my life: my parents and my fiancé. My parents, Johnny and Karen, you have never been science people yet you have always supported me since day 1 when I said I wanted to get into physics, study the stars, study rocks, study topics that you may never understand. Despite that, you two have always supported me, guided me through life, teaching me that hard work will always pay off, if that means work first, play later. You were right, it has paid off. Being the first person in the family to get a college education, I had an extra hard time adapting to college, save the fact graduate school. You have taught me that I could do anything I wanted, even things you guys would never comprehend, you still cheered me on. Thank you for bringing me up to be a strong, versatile, yet sensitive and well-rounded person, for putting up with so many times I could not come home to visit because of school. Most importantly, thank you for loving and believing in me and made sure that I continue to believe in myself. I love you guys.

My fiancé, Dr. Ian McGlynn, you are my Martian partner in crime. Although my studies at Tennessee did not work out, I am still so grateful I went there and met you and now I am successful. You are my utmost role model in planetary research. I learned so much from you from reading difficult journal papers, to attending research conferences, and thinking professionally in the planetary field early on. Thank you for putting up with my many insane grad-school-induced moods and crazy sleeping habits. But also thank you for opening up my mind to the many possibilities and perspectives of science and good food. As you have just finished your PhD and I my MS, I cannot wait to embark on our next chapter in life bouncing around as geophysicist and geochemist in Houston!

TABLE OF CONTENTS

LIST OF TABLES AND FIGURES

Chapter 1: Introduction

1.1 The Red Planet: Earth's Smaller Neighbor

Being the second closest planet to Earth, Mars has always been a target of curiosity and exploration. Throughout history, the small, red planet that is named after the Roman god of war has always revealed just enough to pique man's curiosity, while shrouding the rest of its secrets in mystery, beckoning to be discovered. For the last few decades, many planetary spacecraft missions have visited the red planet including fly-bys, orbiters, landers and rovers. These spacecraft included the Mariner and Viking missions in the 1960's and 1970's to the Mars Global Surveyor (MGS) and Mars Pathfinder missions both in 1996, the Mars Exploration Rovers (MER) mission in 2003, the Mars Reconnaissance Orbiter (MRO) in 2005, and the Phoenix Mars mission in 2007 (Barlow, 2008). These spacecraft have collected observations and data enabling the study of topics ranging from rock and mineral compositions to the intriguing volcanoes and canyons, as well as global internal and external structures. A tremendous amount of data has been gathered from each of these, and other, missions and has resulted in numerous studies and publications on the planet. Yet, with this influx of new knowledge about our neighbor, there is still much to be learned about Mars.

Mars is the fourth terrestrial planet from the Sun. While Venus and Earth are approximately the same in mass and size, Mars is less than one-third the volume of Earth, with a mean radius of 3390 km. Having only about one-tenth the mass of Earth, Mars also possesses a smaller gravitational acceleration (3.71 m/s^2 versus Earth's 9.8 m/s^2) and, unlike Earth, Mars does not presently possess an internally generated magnetic field (Zuber, 2001). However, there are many similarities between Earth and Mars. The 24.62 hour rotational period of Mars is just a bit longer than Earth's 23.93 hours, and Mars' axial tilt is 25.2 degrees while Earth's is 23.5 degrees (Barlow, 2008). In addition to these shared orbital characteristics, Mars also has many geological features and processes including mountains, volcanoes, canyons, and basins, all of which are comparable to those on Earth.

1.2 Surface Features and Topography

Of the four terrestrial planets, Mars is home to some of the most spectacular geological features in the Solar System. One of the most striking surface features is the enormous volcanic construct, the Tharsis Bulge or the Tharsis Rise, home to Olympus Mons, the largest volcano in the Solar System (Figure 1.1 and 1.2). Olympus Mons is one of five large shield volcanoes in the region and is about the size of the state of Washington, spanning about 600 km across and reaching to a height of about 24 km from the base (Francis and Oppenheimer, 2004). Another geologic feature that is clearly visible from space is Valles Marineris, named after the Mariner spacecraft. Valles Marineris is a great canyon system that has the distinction of being the largest canyon in the Solar System. It extends to about 4000 km in length, almost the width of the United States, and cuts up to 10 km deep into the planet (Carr, 2006). These large features seem out of proportion to the planet's relatively small size. There are also a few prominent, large impact basins that have deformed the surface. These include the Hellas Basin, Isidis Basin, and Argyre Basin (Figure 1.2). In addition, Mars also has two seasonally varying polar ice caps at each pole. Other geological features including outflow channels at the base of Valles Marineris, fluvial systems, valley networks, sand dunes, and other lithological structures are also found on Mars (Carr, 2006).

At present we have a more precise topographic model of the planet Mars than we do with Earth. Thanks to the Mars Orbiter Laser Altimeter (MOLA) instrument aboard the Mars Global Surveyor (MGS) spacecraft, we have an unprecedented view of the topographic lows and highs of Mars (Smith et al., 1999a). The highest elevation is at about 21.3 km at the peak of Olympus Mons and the lowest elevation is at about -8.2 km on the floor of the Hellas Basin (Barlow, 2008). The MGS spacecraft emits an infrared laser pulse at the Martian surface; by measuring the two-way travel time of the laser energy transmitted and reflected off the planet's surface, the laser altimeter collects a single track of data for each orbit. These data have a spatial resolution of 330 m and a vertical resolution of 37.5 cm on smooth surfaces or up to 10 m on 30° slopes. The estimated errors in the global surface elevations include radial orbit error of 7 m, instrument error of 3 m, and geoid error of ± 10 m (Zuber et al., 1992, Smith et al., 1998,

Smith et al., 1999a, and Wieczorek, 2007). The MOLA instrument tracks have been processed into digital elevation models or sets of spherical harmonic coefficients that are available from the Planetary Data System node.

The gravitational potential data is obtained from the Radio Science experiment. The Radio Science experiment tracks the Mars Global Surveyor (MGS) spacecraft using the Deep Space Network (DSN) ground antenna on Earth's surface. As MGS orbits Mars, the Radio Science instrument transmits a radio signal to DSN and DSN records the two-way travel-time; the received signal shows phase variations in the signal propagation between the spacecraft and the tracking station on Earth. This gives a line-of-sight velocity for the spacecraft and changes in the spacecraft's motions (i.e. velocity) revealing the planet's mass distribution (Tyler et al., 1992). The accuracy in MGS's velocity is 0.1 mm/s (Smith et al., 1999b). Uncertainties in radial gravity are 10 mGal and uncertainties in the geoid are 2 m (Wieczorek, 2007). The resolution of the gravitational potential model depends on the maximum degree of the spherical harmonic that is used in the expansion; for example, a gravity model resolved to spherical harmonic degree and order 48 is about 220 km (Smith et al., 1999b). This will be discussed further in Chapter 2. The gravitational potential models are represented as sets of spherical harmonic coefficients that are available on the Planetary Data System.

Most planetary scientists would agree that the most prominent geologic feature on Mars is the topographic crustal dichotomy. It is a topographic boundary (Figures 1.3a, b) that runs along the equator, separating the planet into two distinct hemispheres: the Northern Lowlands and the Southern Highlands (Carr, 2006). The Northern Lowlands are characterized by low elevation terrain, with smooth, resurfaced sedimentary deposits and lava plains and few craters, while the Southern Highlands are characterized by high elevation topography with heavily-cratered terrains that include the planet's volcanic regions and canyons. The average difference in elevation between the two hemispheres is about 5 km (Smith et al., 1999a). In addition, the Northern Lowlands are presumably underlain by a thinner crust averaging about 32 km, whereas the Southern Highlands are underlain by a thicker crust averaging about 58 km (Neumann et al., 2004). The surface expressions of the two hemispheres differ in elevation, thickness, crater density, and roughness (Smith et al., 1999a).

In order to describe the relative timing of events on the Martian surface, we refer to the Martian geologic timescale which is divided into three epochs (Tanaka, 1986). The oldest is called the Noachian epoch, which is estimated to be 3.7 billion years ago (Ga) and older. The middle epoch is the Hesperian, which spans the time period from 3.7 Ga to 3.0 Ga. Lastly, the youngest epoch is the Amazonian, which spans the period from 3.0 Ga to the present. The 3.7 Ga boundary is set based on crater density studies and corresponds to the end of the Late Heavy Bombardment that occurred in the Solar System around the same time (Hartmann and Neukum, 2001).

1.3 Previous and Current Studies

With so many studies that have been conducted, one question has always lingered: how did the enigmatic crustal dichotomy form and what are its implications for the evolution of Mars? At first, the Northern Lowlands seemed to be younger in relative age (in the Hesperian epoch) than the Southern Highlands due to the smaller number of visible craters in the Northern Lowlands. Subsequent studies have shown that the Northern Lowlands has a base that is just as old as the Southern Highlands (in the Noachian epoch), with the exception that the north is covered by a younger layer of sedimentary and volcanic deposits, which give it the resurfaced, smoother texture (Frey et al., 2002; Solomon et al., 2005). Thus, it is suggested that the crustal dichotomy, which straddles both the northern and southern hemispheres, must have been formed very early on in Martian history -- sometime in the early Noachian (Zuber, 2001) and even as early as about 100 Myr after accretionary formation of the planet (Nimmo et al., 2008).

Many theories have been proposed for the formation of the crustal dichotomy. These include an impact theory (Wilhelms and Squyres, 1984; Frey and Schultz, 1988), which claims that a giant body had impacted the northern hemisphere (Figure 1.4), creating the hemispheric basin called Borealis Basin (Andrews-Hanna et al., 2008; Marinova et al., 2008), and giving rise to the Northern Lowlands and the Southern Highlands. Although the studies by Andrews-Hanna et al. (2008) and Marinova et al. (2008) provide support to each other, the remnant ejecta materials predicted from such a large impact have not been found. Another theory is that the thick crust of the southern

hemisphere formed from an early phase of spherical harmonic degree-1 mantle convection (Figure 1.5) (Zhong and Zuber, 2001; Roberts and Zhong, 2006), involving a single one-plume upwelling that formed due to viscosity stratification in the mantle. Another related hypoothesis is a global mantle overturn (Elkins-Tanton et al., 2005), where a change in the composition of melt in the mantle can make the fluid magma unstable, therefore "overturning" the mantle and creating an upwelling in one hemisphere and a downwelling in the other hemisphere, contributing to the different amount of material buildup, thus the different thicknesses of each hemisphere (Zuber, 2001). Each of these theories provide us with testable observations that will help us better understand how the crustal dichotomy could have formed, but each of them is incomplete and requires further investigation.

In addition to the prominent question on the origin of the dichotomy is another important and perhaps related question: did the Tharsis Rise volcanic construct form from one or more mantle plumes (Kiefer, 2003)? One theory suggests that a mantle plume may have formed in the middle of the Southern Highlands, near the present day South Pole, and migrated to the current location of Tharsis Rise near the dichotomy boundary at the equator (Zhong, 2009; Sramek and Zhong, 2010), not unlike the formation and migration of the chain of Hawaiian islands/hotspot. Given that Mars is considered to be a one-plate planet, it is unlikely for the entire lithosphere to migrate as plates do on Earth; they suggest that this phenomenon may be connected with the concept of true polar wander, TPW (Figure 1.6). Roberts and Zhong (2007) and Zhong's (2009) studies suggest that since the Tharsis Rise region has a dichotomy asymmetry on its own with more volcanism in the western hemisphere than the eastern hemisphere, that this asymmetry, which is about 90 degrees offset from the North-South topographic dichotomy, may be reason to support his plume migration theory that started at the South Pole and migrated to about 90 degrees toward the dichotomy boundary at the equator. I will return to this theory and provide possible supporting evidence for the migrating plume in Chapter 3.

The work described in this thesis follows in the footsteps of previous studies conducted by Zuber et al. (2000) and Neumann et al. (2004). Both of those studies utilized MGS topography (MOLA) and gravity (Radio Science) data to understand the

crustal thickness of Mars, thereby examining the internal structure and the thermal evolution of the planet. Both studies, along with my work, are based on the method of Wieczorek and Phillips (1998) and my study uses the crustal thickness program and freely available software archive SHTOOLS developed by Mark Wieczorek (available at http://www.ipgp.fr/~wieczor/SHTOOLS/SHTOOLS.html). The MGS topography and gravity data sets used in this work are computed models that are represented as sets of spherical harmonic coefficients, which will be explained and discussed in further detail in Chapter 2.

The previous work of Zuber et al. (2000) and Neumann et al. (2004) both solved for the crustal thickness of Mars using a set of assumptions. One major assumption is that the densities of the crust and mantle are uniform and based on petrologic properties of a special set of meteorites called the SNC meteorites (Goettel, 1981; McSween, 1985; Sohl and Spohn, 1997; Bertka and Fei, 1998; McKenzie et al., 2002), assumed to have originated from Mars. The SNC meteorites, short for Shergottites, Nakhlites, and Chassignites are achondritic meteorites that are thought to derive from a basaltic crust (Shergottites and Nakhlites) and an olivine upper mantle (Chassignites) of Mars (McSween, 1985; Dreibus and Wanke, 1985; Bertka and Fei, 1998). They agree with the proposed crystallization age of the Martian silicate crust and a chondritic bulk composition of the Martian mantle. The densities constrained from these meteorites give a value of 2900 kg/m^3 for a silicate, basaltic crust and 3500 kg/m^3 for an olivine upper mantle, which are the densities that were adopted by both previous studies and the work in this thesis. Table 1 shows the density ranges of each meteorite and associated compositions. As shown in the table, these densities are larger than would be expected based on terrestrial settings. This is due to the more iron-rich crust and mantle of Mars; a study by McGovern et al. (2002) also suggests that the bulk density of 2900 kg/m^3 gave the best fit for admittance over Mars.

Both previous studies assumed the above crustal and mantle densities and a minimum crustal thickness then used the method of Wieczorek and Phillips (1998) with a density contrast of 600 kg/m^3. The method of Wieczorek and Phillips (1998) calculates the Bouguer gravity anomaly from the surface topography then solves for the relief on the crust-mantle interface, or the Moho, that is needed to explain the Bouguer gravity

anomaly. By subtracting the relief on the Moho from surface topography, they estimate the crustal thickness of the planet. This approach differs from many Earth-based gravity studies that begin with an assumption of isostacy. The results of Zuber et al. (2000) and Neumann et al. (2004) show that the planet has a bimodal crustal thickness, with the southern hemisphere possessing a thicker crust of about 58 km and the northern hemisphere possessing a thinner crust of about 32 km (Figure 1.3b). The thicker crust of the southern hemisphere thins toward the crust of the northern hemisphere, giving rise to not only the topographic dichotomy, but also a crustal thickness dichotomy, indicating an overall planetary mass redistribution to one side of the planet.

In Neumann et al.'s (2004) study, a higher density for specific volcanic regions and a lower density for the polar caps at both poles were adopted. They find that the crust in the northern hemisphere tends to vary more than the crust in the southern hemisphere. For example, the Tharsis Rise region exhibits a much thicker crust, which is likely due to volcanism and tectonism. Combining their crustal thickness models with the observed gravity anomalies they find that certain features such as Olympus, Ascraeus, and Pavonis Mons in the Tharsis Rise region may not be isostatically compensated while other regions such as Hellas and Isidis Basins are in isostatic equilibrium. My study follows similar procedure although I test the additional assumption of global isostacy at long wavelengths. I also test the sensitivity of the crustal thickness to the assumed density contrast between the crust and the mantle. The detailed steps taken in the modeling will be developed further in the methods section, Chapter 2 and results and further discussion will be presented in Chapters 3. I will provide some thoughts on future directions in Chapter 4.

1.4 Limited Data

Since the first mission to Mars, many missions have brought with them the indispensible instruments that helped decipher the chemical compositions of rocks and minerals on the red planet. While other instruments gathered topographic data (MOLA) and gravity measurements (Radio Science instrument) with accumulating success, one instrument that would have given us an immense amount of information about the

interior structure of Mars failed to do its job. The Viking 1 and Viking 2 landers both carried with them a seismometer that measured seismic waves that would have recorded reflections and refractions off boundaries within Mars' interior. Unfortunately, the seismometer failed to work properly in both missions, giving us no useful seismic data to work with (Barlow, 2008).

Seismic data would have given us important constraints on the internal structures including the exact size of the core and the thickness of the mantle; it would have helped us deduce whether active mantle convection is present. Seismic results could also contribute to answering the mystery on the formation of the crustal dichotomy and the Tharsis Rise region. Since the two Viking missions, no subsequent successful missions to Mars have had a seismometer.

A piece of evidence that can help us infer about the internal structure of Mars is the presence of a scattered, remnant magnetic field (Acuna et al., 1999; Stevenson, 2001; Solomon et al., 2005), which may indicate a former active core dynamo. This means mantle dynamics and possible plumes could have existed and played a crucial role in the thermal history and evolution of the planet. Although this is an important fact to note, it is outside the scope of this study and will not be further discussed. However, a more comprehensive study of the planet's interior should certainly consider using such supplementary data to better understand and constrain the Martian interior. Thus, most of what we know of the Martian interior comes from geophysical modeling such as the work presented in this thesis.

Figure 1.1

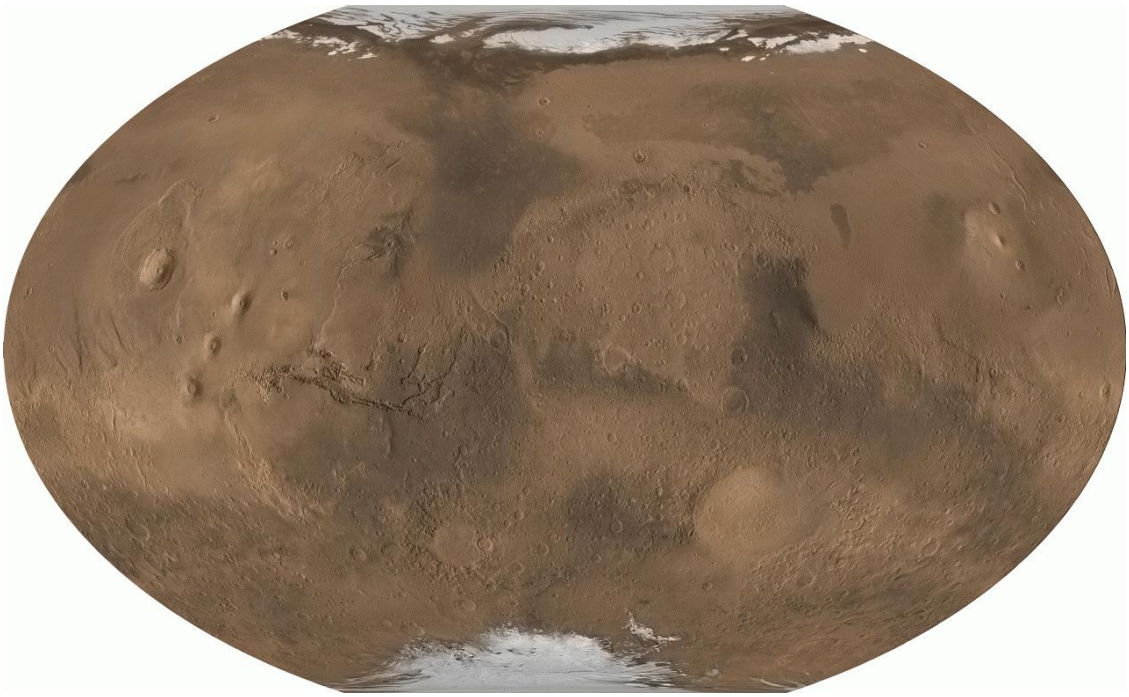

Terrain map of Mars, produced by data and images obtained from the Mars Global Surveyor (MGS) spacecraft. Image obtained from NASA available at this website, found on October 19, 2009: http://mola.gsfc.nasa.gov/images/ngs.gif.

Figure 1.2

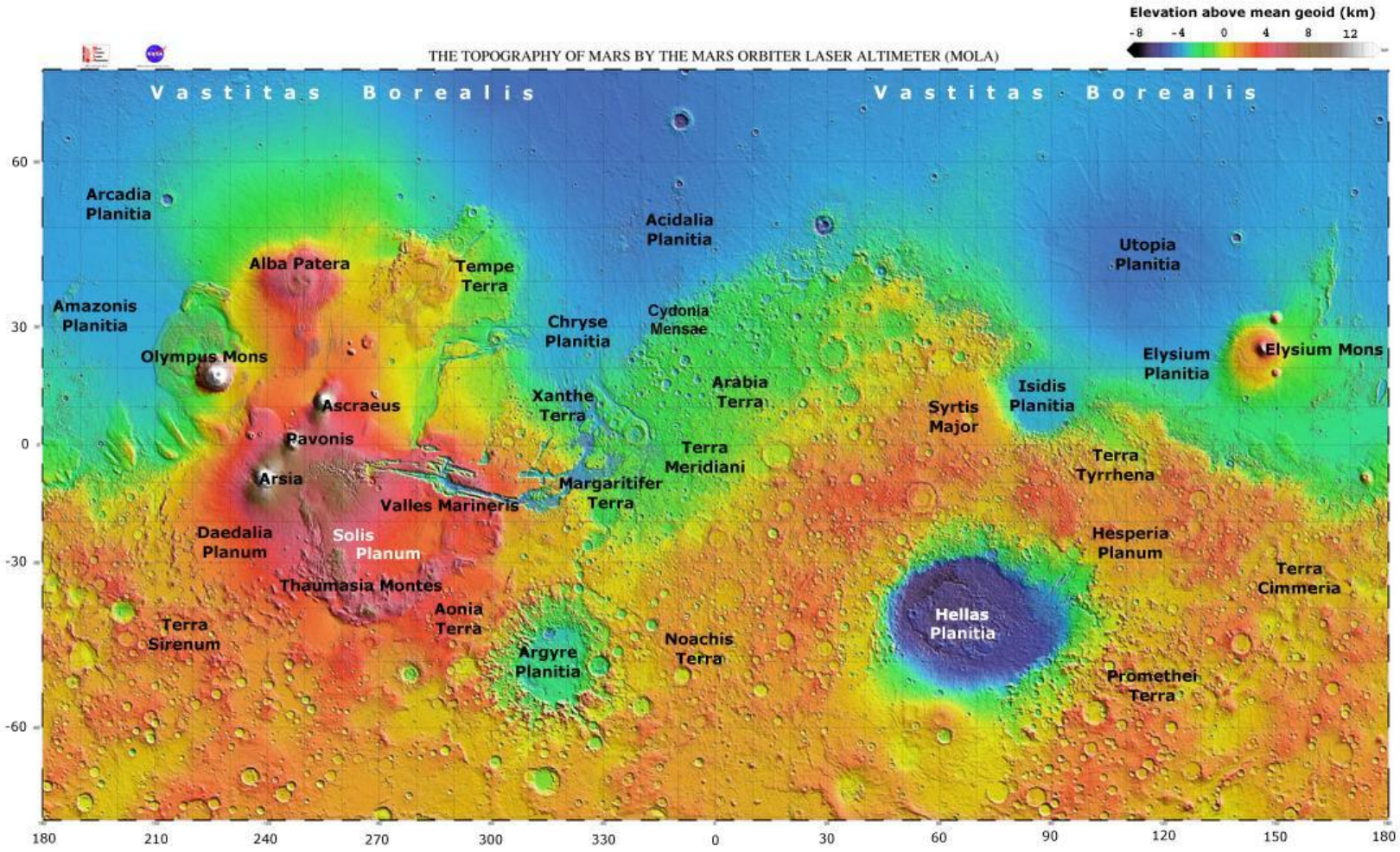

A MOLA elevation map showing the two distinct hemispheres on Mars. Various features discussed and of interest are labeled. Figure from C. M. Rodrigue, Geography, CSULB, 2007, available at this website, found on January 25, 2010: http://www.csulb.edu/~rodrigue/mars/MOLAmercatorlabel.jpg.

Figure 1.3

a.

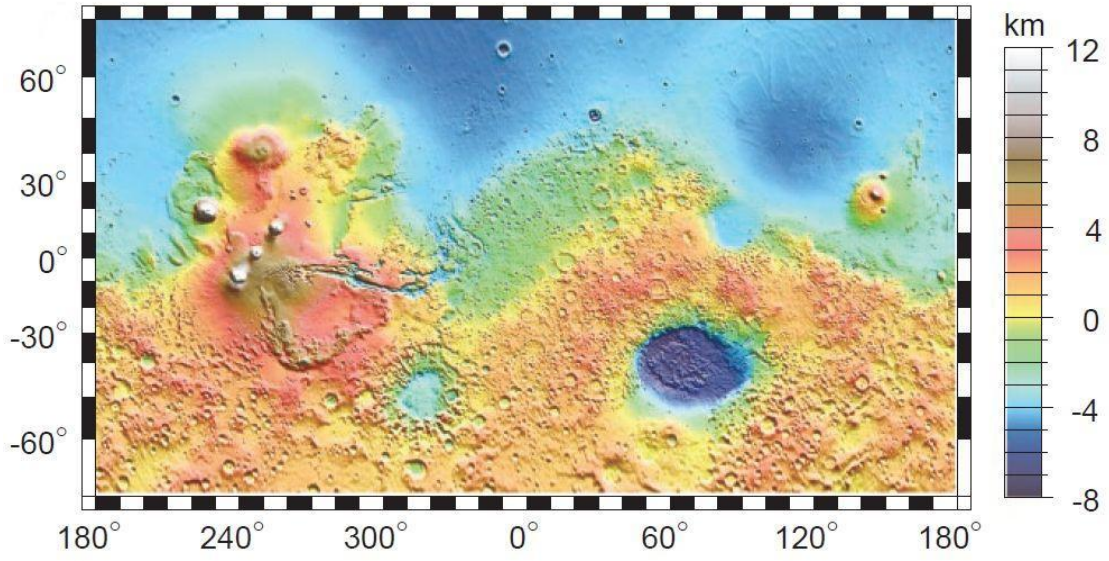

b.

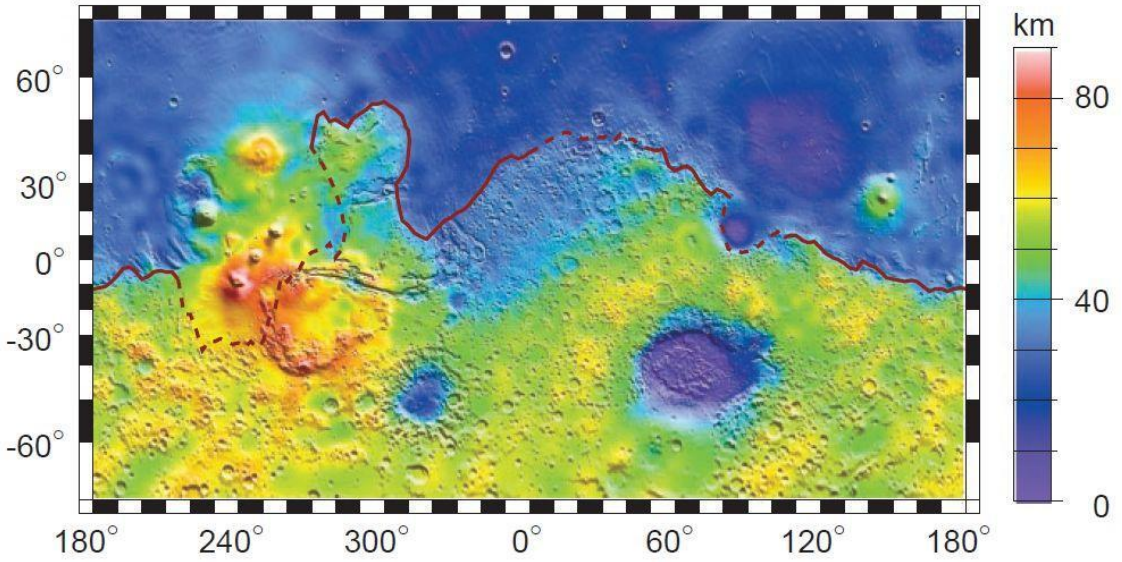

a. A MOLA elevation map showing the topographic dichotomy on Mars. The boundary runs along the Martian equator as it divides the planet into two distinct hemispheres of low and high elevation. Figure from Zuber et al., 2000.

b. A crustal thickness map revealing the thinner crust of the northern hemisphere and impact basins and thicker crust of the southern hemisphere and the volcanic construct Tharsis Rise. Figure from Zuber et al., 2000.

Figure 1.4

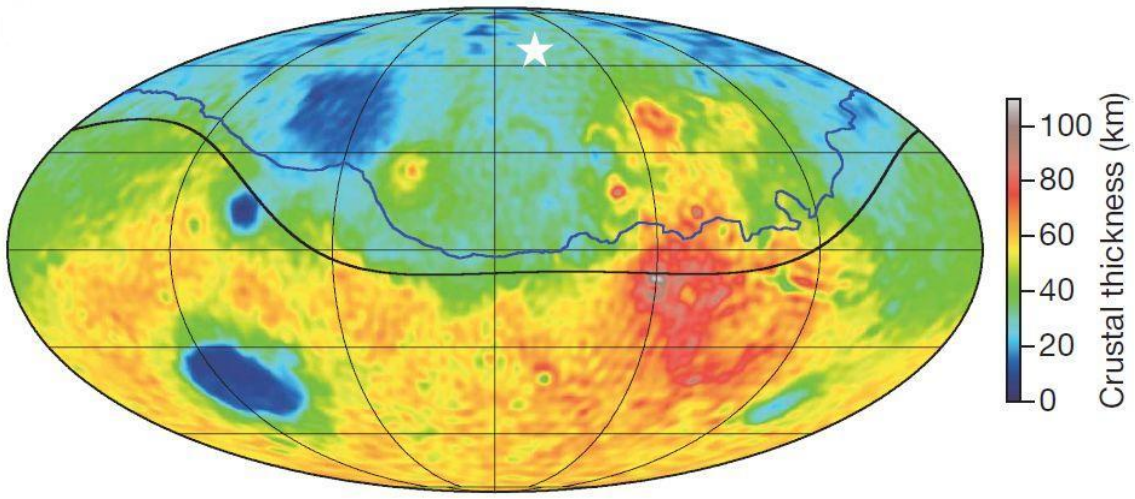

Crustal thickness map from Marinova et al. (2008), showing the location where excavation of the crust may have occurred (star). The boundary of the impact proposed by Andrews-Hanna et al. (2008) is indicated by the blue line.

Figure 1.5

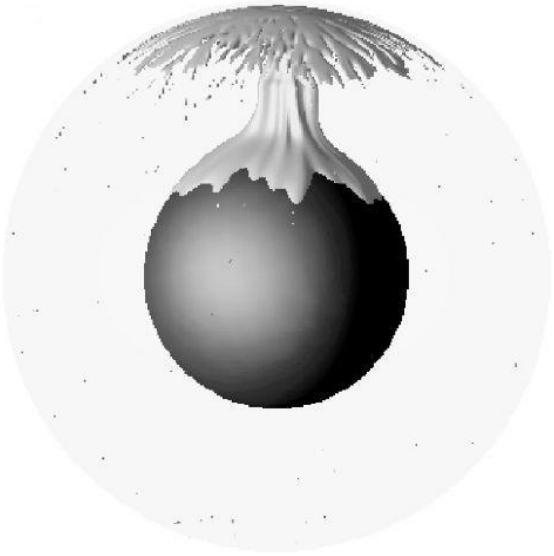

A schematic diagram of what a spherical harmonic degree-1 mantle plume looks like, from Roberts and Zhong (2006). (Used under fair use guidelines, 2012).

Figure 1.6

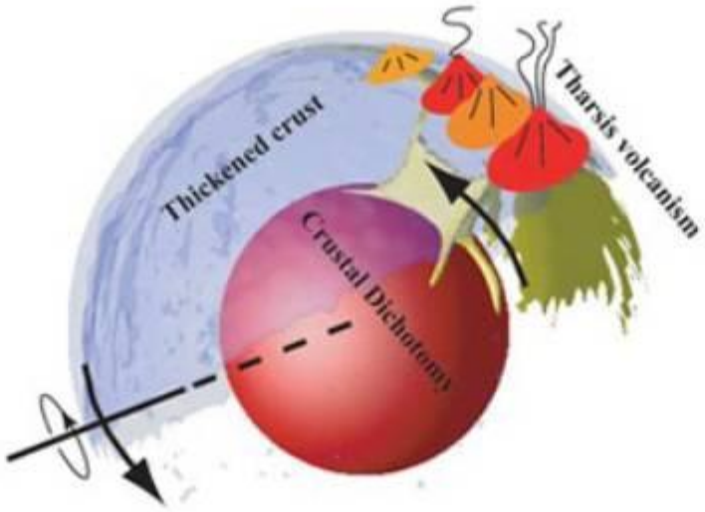

A figure from Zhong (2009) depicting his theory on a migrating mantle plume from the South Pole of Mars to the current location of Tharsis Rise near the dichotomy boundary at the equator. (Used under fair use guidelines, 2012).

Table 1. SNC Meteorites and Associated Composition Densities

Name	**Type**	**Density Range, kg/m^3**
Shergottite	Basalt	3320
Nakhlite	Clinopyroxenite	3480
Chassignite	Dunite	3580
Regional densities	Rocky crust	2350-3350
Wieczorek and Zuber (2004)	Bulk rocky crust	2700-3100
Best fit density, McGovern et al. (2002)	Rocky crust	2900

Values obtained from Neumann et al., 2004.

Chapter 2: Methods

2.1 Geophysical Modeling

To make inferences about the interior structure of Mars, we rely on the information gathered from available geophysical models and petrologic studies. Digital Elevation Models (DEMs) not only show the obvious geologic features visible on the surface; when integrated with gravity data, these models can reveal a lot about the interior structure of a planet, including mass distributions and possible interior dynamics including mantle structures (Zuber et al., 2000). Combining these models can help us understand how the crustal dichotomy was formed, if the Tharsis volcanic region was formed by a mantle plume, and infer about the structural and thermal history of Mars.

Throughout this chapter, I will discuss gravitational potential, gravity anomalies, and geoid anomalies. The gravitational potential is work done (or energy stored) on a mass by the force of a gravitational field (gravity) that is exerted on that mass. The gravitational potential at a point is determined by the mass difference and depth of density anomalies beneath (and surrounding) the point of observation. Because the largest mass anomaly is the long-wavelength departure of the planet from a sphere, it is customary to reference potential anomalies to the reference ellipsoid. The ellipsoid is the best fitting ellipse that represents the long-wavelength shape of a planet; its radius deviates the most from the poles and the equatorial region due to the rotation of the planet and if the planet was a uniform density body (which no planet is of course), the gravitational potential would be constant everywhere on the ellipsoid. The geoid is the true equipotential surface, and the geoid height is measured relative to the reference ellipsoid. On Mars, the geoid is sometimes referred to as the areoid although many researchers prefer to stick with the term geoid. These highs and lows manifest from the broad undulations believed to come from mantle convection, which deviate from that reference ellipsoid and is the true shape of the planet. While the ellipsoid has a greater departure from a sphere, the geoid's departure from the reference ellipsoid is only on the order of 50 to 100 m (Blakely, 1996). Thus, studying the geoid anomalies and gravity

anomalies over a region can give insight to the behavior of the underlying mass in that region. More details on these topics are discussed in sections 2.3 and 2.4.

2.2 Spherical Harmonics

Gravitational potential models on a planet are constructed using spherical harmonic functions. The observed satellite tracking data from the Radio Science experiment are used as a basis for the gravitational potential model. Sets of gravitational potential coefficients are created by fitting the observed track data on a sphere (Smith et al., 1999). If we knew the internal density structure of the planet, then the density distribution of each depth could be represented by separate sets of harmonic coefficients, that when summed together, would give the overall gravitational potential field of that total distribution (Blakely, 1996). Spherical harmonic functions are also easier to work with when studying potential theory. Hence, they are more useful than Cartesian methods in this study.

Spherical harmonic functions are comprised of periodic, sinusoidal functions in longitude and periodic Legendre functions in latitude. Functions that only vary with latitude are called zonal harmonics, and functions that only vary with longitude are called sectoral harmonics, and tesseral harmonics vary in both directions (Blakely, 1996) (Figure 2.1). The degree l and order m of a spherical harmonic function indicate the scale over which the function varies with latitude and longitude, respectively (Barlow, 2006); in other words, these two variables show how the function varies across the globe. The degree l can also give a sense of resolution: the smaller degree l is, the longer the wavelength of the function, and the larger the degree l is, the shorter the wavelength of the function. For example, the crustal dichotomy that divides Mars into two hemispheres can be approximated by the degree-1, order-0 spherical harmonic function (Figure 2.2). The degree minus order, in this case, 1-0 = 1, gives one line of latitude (in this case the equator) that separates the sphere into a northern hemisphere and southern hemisphere, while the order, in this case zero, means that there is no variation of the harmonic as a function of longitude. For example, if the order $m = 1$, then there would be one line of longitude, separating the sphere into a western and eastern hemisphere. A combination

of various degrees and orders are summed up to represent various scales of surface features, from local to regional to global scale.

The spatial resolution of the spherical harmonic coefficient is calculated by $2\pi R / (l - m)$ for the wavelength in the North-South direction or $2\pi R / l$ for the wavelength in the East-West direction, where R is the planetary radius, l and m are the spherical harmonic degree and order, respectively (Wahr, 1996). However, the spherical harmonic coefficients are independent of direction so generally the spatial resolution is approximated as $2\pi R / l$ and the value of m will give the sense of direction. Thus for Mars, with a mean planetary radius of R = 3390 km, a data set with a maximum spherical harmonic degree l of 100 would be a spatial resolution of 2π(3390 km) / 100 ≈ 213 km.

In Section 2.4, I discuss how the reference ellipsoid term $\frac{GM}{r^3}a^2J_2$, which approximates the ellipsoidal shape of the planet, is associated with a degree l = 2 (Y_2^0) component of the gravitational potential and that there is no degree l = 1 component in the gravitational potential. For all planets, usually the degree l = 1 component is zero by choosing to work in the center-of-mass coordinate system. This leads to a center-of-mass-center-of-figure (COM-COF) offset (e. g. Wieczorek, 2007). For planets such as Earth and Venus, removing this degree-1 component does not have a large effect on the interpretation of the gravitational potential because these planets do not have a large associated degree-1 topographic component. However, because the surface topography of Mars is characterized by an enormous degree-1 component manifested as the topographic/crustal dichotomy, it is important to note that removing the degree-1 component of the gravitational potential may also be removing an important contribution to the potential associated with the topography.

2.3 Controls on Gravity

Because the signature of gravity is non-unique, countless combinations of mass distributions could give the same gravity signature. Thus modeling the gravitational potential field requires certain additional assumptions. I start by assuming a layer of crust resting on top of a layer of mantle, assuming a constant density in each layer. In order to constrain the crustal and mantle densities, I constrain their compositions using a

specific set of special meteorites called the SNC meteorites, discussed in detail in Chapter 1. The SNC meteorites, thought to be achondritic meteorites originated from Mars (Goettel, 1981; Dreibus and Wanke, 1985; McSween, 1985; Sohl and Spohn, 1997; Bertka and Fei, 1998; McKenzie et al., 2002), agree with the proposed crystallization age of the Martian silicate crust and a chondritic bulk composition of the Martian mantle. A study by McGovern et al. (2002) suggests that the bulk crustal density of 2900 kg/m^3 gave the best fit for admittance over Mars, specifically the Tharsis Rise region (the Tharsis Montes and Olympus Mons volcanoes), while Smith et al. (1999a) suggest that the Martian mantle is more iron-rich and would be denser than Earth's, thus a density of 3500 kg/m^3 is assumed for an olivine-rich Martian mantle (Neumann et al., 2004). Collectively, these density studies constrain the bulk density of the basaltic crust of Mars to be 2900 kg/m^3 and the density of an olivine-rich Martian mantle to be 3500 kg/m^3. These are also the same values adopted by other studies of Mars including Zuber (2001) and Neumann et al. (2004).

In addition to crustal and mantle densities, other factors that control gravity include surface topography, crustal thickness, and Moho topography – the relief of the boundary that differentiates the crust from the mantle (Blakely, 1996). Possible hidden subsurface structures of interest within the crust and/or mantle could also contribute to the gravitational signature, but these are beyond the scope of this study and require additional observations. Thus, with the two constrained density values for a constant-density crust and mantle, we can utilize coupled topography and gravity methods to deduce a model of crustal thicknesses and the resulting gravity misfit map, the difference between modeled and observed gravity.

In order to decipher whether parts of the gravitational signature comes from surface topography or a deeper subsurface source, I study the geoid and the gravity anomalies present. The geoid, or areoid, as it is called on Mars, is an equipotential surface of the planet, discussed further in Section 2.4, which could be considered as Mars' "sea level" datum. This surface is shaped by the underlying mass, which can vary depending on the volume and density of the mass underneath. The geoid is a height (km or m) that is measured relative to a reference ellipsoid. The geoid exhibits a bulge (positive height) wherever there is an excess mass or high-density material below, such as

a mountain or an iron ore body. It exhibits a depression (negative height) wherever there is a mass deficiency or low density material below, such as a basin or a buried cavity. The areoid of Mars is shown in Figure 2.6 to demonstrate the shape of the planet's equipotential surface relative to a reference ellipsoid. The areoid shows mass excess (positive height) in the Tharsis volcanic region and the region north of the Hellas Basin, and mass deficit (negative height) or zero height mostly elsewhere on the planet.

The total observed gravity is actually a combination of the attraction of the reference ellipsoid and effects from elevation (Free Air anomaly), topographic mass above sea level (Bouguer anomaly) and other various effects such as tidal forces, isostacy, and density variations within the crust and mantle. Geophysical studies using the gravitational potential often start with observing these various gravity anomalies and calculating for the Free Air anomaly and the Bouguer anomaly.

2.4 Potential Theory

Many components on a planet come together to generate the total observed gravity field. In order to pinpoint the gravity anomalies to specific sources, a series of gravity corrections have to be applied. I follow Wahr (1996) and Blakely (1996) below to show how each of these components affect the observed gravity and the corrections that are applied. I start by examining each of the gravitational components that make up the total gravitational potential in the example equation below, (equation 4.25 from Wahr, 1996).

$$V_T(r,\theta,\varphi) = \left[\frac{GM}{r} + \frac{1}{3}\Omega^2 r^2\right] Y_0^0(\theta,\varphi) - \left[\frac{1}{3}\Omega^2 r^2 + \frac{GM}{r^3}R^2 J_2\right] P_2(\cos\theta) - \frac{GM}{r}\sum_{\substack{l=2 \\ (l,m)\neq(2,0)}}^{\infty}\sum_{m=-l}^{l} V_l^m Y_l^m(\theta,\varphi)\left(\frac{R}{r}\right)^l \tag{2.1}$$

The total gravitational potential of a planet V_T consists of a self-gravitational potential term $\frac{GM}{r}$ where G is the universal gravitational constant, M is the mass of the planet, and r is distance between the center of the planet and the point of observation. This component is in the first bracket term above. The second term, $\frac{1}{3}\Omega^2 r^2$, comes from the rotation of the planet, where Ω is the rotational period of the planet (for Mars, Ω = 24.62 hrs or 88632 sec). These two terms in the first bracket, collectively the coefficient of the Y_0^0 term, describe the potential of a self-gravitating and rotating planet and represent the spherical harmonic degree $l = 0$ structure that corresponds to the planet's center-of-mass (COM). Rotation also introduces a term that depends on latitude and this is given by the third term, $P_2(\cos\theta)\frac{1}{3}\Omega^2 r^2$, where $P_2(\cos\theta)$ is the Legendre polynomial for degree l = 2. For historical reasons, this term is written using P_2 rather than Y_2^0, but as you can see the difference is a constant, because $P_2 = P_2^0 = \sqrt{\frac{4\pi}{5}}\, Y_2^0$. The fourth term in equation 2.1 arises because the rotating planet is no longer spherical but is flattened. The constant J_2 can be related to the equatorial flattening factor, f, by $J_2 = \frac{2}{3}f - \frac{a\Omega^2}{3g_T}$ (Wahr, 1996), where f is the difference between the equatorial radius, a, and the polar radius, c divided by the equatorial radius, or $f = \frac{a-c}{a}$. The effect from this component on the total potential V_T is shown by the terms in the second bracket above $\left[\frac{1}{3}\Omega^2 r^2 + \frac{GM}{r^3}R^2 J_2\right]$ where $\frac{1}{3}\Omega^2 r^2$ is the component from the centrifugal force and J_2 is the ellipticity coefficient. These two terms in this second bracket define the reference ellipsoid, or the overall shape of a uniform planet and correspond to the spherical harmonic degree l = 2, order m = 0 component. They are two orders of magnitude larger than the other terms in the potential expansion. The remaining sum is the spherical harmonic expansion of the potential coefficients, V_l^m, summed over degree l and order m terms. Notice that the summation $\sum_{\substack{l=2 \\ (l,m)}}^{\infty} \sum_{\substack{m=-l \\ \neq(2,0)}}^{l} V_l^m Y_l^m(\theta,\varphi)\left(\frac{R}{r}\right)^l$ start at degree l = 2, but excludes the l = 2, m = 0 component. This expansion does not include l = 1 because it assumes that the origin of the coordinate system is the same as the center-of-mass, thus assuming zero offset between the center-of-mass (COM) and the center-of-figure (COF). This is a point we

will come back to later, because the expansion of global topography has a degree $l = 1$ contribution (Wieczorek, 2007) and thus there will be a resulting degree $l = 1$ isostatic geoid anomaly.

2.4.1 Potential on the Geoid

Gravity varies as a function of height above the surface. We can calculate the spherical harmonic gravitational coefficients from the spherical harmonic potential coefficients by $g_l^m = \frac{GM}{R^2}\,(1-l)\,V_l^m = g\,(1-l)V_l^m$. A satellite such as Mars Global Surveyor orbiting Mars at an average altitude of 378 km above the surface will experience a different force due to gravity g than if it were at the surface of Mars. This can be seen in the potential expansion by the $\left(\frac{R}{r}\right)^l$ term in the last term of equation 2.1. Thus the measured potential at the satellite is corrected to the surface by downward continuing the potential at the satellite altitude r_{sat} to the surface, R. This can be calculated by multiplying the potential coefficients by $\left(\frac{R}{r_{sat}}\right)^l$ here. This is also demonstrated by:

$$g_{FA}(R) = g(r_{sat}) - \frac{2g(r)}{R}\sum T_l^m\ Y_l^m\,(\theta,\varphi)\left(\frac{R}{r_{sat}}\right)^l \tag{2.2}$$

where $g_{FA}(R)$ is the gravity on the geoid, $g(r_{sat})$ is the gravity at the satellite altitude $h = r_{sat} - R$ above the surface, R is the mean planetary radius, $h(\theta,\varphi) = \sum T_l^m\ Y_l^m\,(\theta,\varphi)$, and T_l^m are the coefficients of the surface topography.

2.4.2 Free Air and Bouguer Gravity Anomalies

The "removal" of this height, such as bringing the height of the satellite from orbit down to the surface of the planet is effectively the same as the Free Air correction in regional gravity studies. When the Free Air correction has been applied (or subtracted) and the reference ellipsoid g_0 has also been subtracted from the observed gravity g_{OBS}, the resulting gravity anomaly (measured in milligals) is the Free Air anomaly Δg_{FA}:

$$\Delta g_{FA} = g_{OBS} - g_{FA} - g_0 \tag{2.3}$$

Figure 2.3 shows a map of Free Air anomalies on Mars. The Free Air anomaly still contain gravity signal contributed by the mass from surrounding topography. The gravity that comes from the topography is the Bouguer gravity g_{BA}, which is dependent on the density ρ_{crust} of the crustal material (positive mass above the ellipsoid) and the height *h* of the mass (such as the height of a mountain):

$$g_{BA} = \frac{4\pi\rho_{crust}R^2}{M(2l+1)} \sum T_l^m \; Y_l^m \; (\theta, \varphi) \tag{2.4}$$

where M is the mass of the planet. To apply the Bouguer Correction, the positive mass above the sea level (or reference ellipsoid) have to be assumed as an infinite slab of crust with a thickness *h*, and a uniform density ρ in order for it to be removed from the surface of the planet. This gives a simple Bouguer anomaly Δg_{BA}:

$$\Delta g_{BA} = g_{OBS} - g_{FA} - g_{BA} - g_0 \tag{2.5}$$

which is the observed gravity g_{OBS} subtracting the reference ellipsoid g_0, and removing both the gravity effect from elevation or Free Air g_{FA} and the effect from surrounding topography g_{BA}. Figure 2.4 shows a map of Bouguer anomalies on Mars. After these corrections are applied, the remaining anomaly should correspond to density variations within the crust and mantle, which will help us study possible hidden subsurface structures (Blakely, 1996).

2.5 The Principle of Isostacy

A common place to begin with gravity modeling is the assumption of isostacy. There are two types of isostacy: Airy isostacy and Pratt isostacy. Airy isostacy states that

each vertical column of material from the surface down to a certain depth of compensation would have equal mass. This means that a column of crustal material with excess mass (such as a mountain and crustal root) would have the same mass as a column of crust with mass deficit (such as a basin) and excess mantle material (mantle uplift or rebound beneath the basin), assuming that both the crustal density and mantle density are uniform and do not vary laterally (Blakely, 1996). Also, in Airy isostacy the shape of the Moho topography should be a scaled, mirror-image of the surface topography, with the depth to the root determined by the density contrast between the crust and mantle. Where there is a mass excess/topographic high on the surface, such as a mountain, there would be a large crustal root of lower-crustal-density material extending down to the higher-density mantle to support the structure above. Where there is a mass deficit/topographic low, such as a basin on the surface, there would be a mantle uplift of higher-density material rising up to compensate for the deficit (Figure 2.5b). Pratt isostacy states that each vertical column of crustal material would have equal mass, assuming lateral changes in density. Thus in Airy isostacy, the compensation depth varies and should be a mirror-image of the surface topography, whereas in Pratt isostacy, the compensation depth is at the same depth everywhere (Blakely, 1996).

Understanding whether a structure is isostatically compensated or not gives insight to possible hidden internal structures and helps piece together the thermal and crustal relaxation history of a region. It is important to note that the method of Wieczorek and Phillips used in the Mars Crustal Thickness (MCT) code does not explicitly assume isostacy. The equations described in Section 2.6 comprise the standard method used in planetary geophysics studies (Wieczorek and Phillips, 1998; Zuber et al., 2000; Neumann et al., 2004; Wieczorek, 2007). Mars is considered a stagnant lid planet with a thick lithosphere and the underlying assumption is that the lithosphere is too thick and stiff to allow isostatic compensation to take place. In my investigation of the subsurface of Mars, I will explicitly assume that the crust is isostatically compensated using Airy isostacy and compare this with the results obtained by using the Wieczorek and Phillips algorithm. This is where my first experiment begins: because the heart of the MCT code is based on Equation 18 in Wieczorek and Phillips (1998), I modified this to incorporate Airy-isostacy following Rapp (1989). I assumed Airy isostacy because of the

assumed crustal and mantle densities derived from the SNC meteorites representing each layer of material. Also, it is difficult to constrain lateral variations in density in the Martian crust or mantle, so I chose to work with a uniform-density model. Neumann et al. 2004 take the uniform density assumption a step further by considering a unique density for the polar caps and the Tharsis volcanic material. Detailed experiments and results will be presented in the next chapter.

2.6 The Crustal Thickness Model Equation

2.6.1 Derivation of Wieczorek and Phillips' Equation

The method I use to calculate crustal thickness has been implemented in a program written in FORTRAN called Mars Crustal Thickness (from here on referred to as MCT) within the SHTOOLS software archive written by Dr. Mark Wieczorek. SHTOOLS is freely available software for download at his website: http://www.ipgp.fr/~wieczor/SHTOOLS/SHTOOLS.html. MCT follows the algorithm of Wieczorek and Phillips (1998) and utilizes spherical harmonic computations to model the gravity of a planet. It can be applied to various planetary bodies and has been used on the Moon and Mars (Wieczorek, 2007).

The heart of the code is based on equation 18 from Wieczorek and Phillips (1998):

$$h_{ilm} = \omega_l \left[\frac{C_{ilm}^{BA} M(2l+1)}{4\pi\Delta\rho D^2} \left(\frac{R}{D}\right)^l - D \sum_{n=2}^{l+3} \frac{{}^n h_{ilm}}{D_n n!} \frac{\prod_{j=1}^{n}(l+4-j)}{(l+3)} \right] \tag{2.6}$$

where ω_l is a stabilizing downward continuation filter applied to the function:

$$\omega_l = \left\{ 1 + \lambda \left[\frac{M(2l+1)}{4\pi\Delta\rho D^2} \left(\frac{R}{D}\right)^l \right]^2 \right\}^{-1} \tag{2.7}$$

C_{ilm}^{BA} are the coefficients due to the Bouguer anomaly, M is the mass of Mars in kg, $\Delta\rho$ is the density contrast between the crust and mantle in kg/m^3, R is the mean planetary radius in m, D is the radius of the average depth of the Moho topography in m, l and m are the spherical harmonic degree and order to expand the function to, respectively, n is the power the spherical harmonic expands to, j is the starting value for the higher order product terms, and λ is a Lagrange multiplier applied to the filter. Equation 18 (or equation 2.6 from here on out) calculates the Moho topography or relief along the crust-mantle interface h_{ilm} that is needed to explain the gravitational signature observed on Mars. Assuming a uniform density for both the crust and mantle (i.e., no mantle convection) and a variable Moho topography, Wieczorek and Phillips (1998) first calculated for the Bouguer anomaly from the surface topography. Next, they solve for the Moho topography that would give that calculated Bouguer anomaly signature. Equation 2.6 and 2.7 are derived from Equations 10 and 17 (2.8 and 2.9 here, respectively) from Wieczorek and Phillips (1998):

$$C_{ilm}^{+} = \frac{4\pi\Delta\rho D^3}{M(2l+1)} \sum_{n=1}^{l+3} \frac{{}^{n}h_{ilm}}{D^n n!} \frac{\prod_{j=1}^{n}(l+4-j)}{(l+3)} \tag{2.8}$$

$$\Phi = \left[C_{ilm}^{BA} - C_{ilm}^{D} \left(\frac{D}{R}\right)^{l} \right]^2 + \lambda (h_{ilm})^2 \tag{2.9}$$

Equation 2.8 comes from a potential equation $U(r, \theta, \varphi)$ that is derived from Newton's law of gravitation and expanding the results of the integration using the binomial theorem (Wieczorek and Phillips, 1998) and equation 2.9 is a function to be minimized. The terms in the summation greater than n = 1 (equation 2.8) are usually ignored; however Rummel et al. (1988) show that at least the n = 2 term can be significant. Equations 2.6 and 2.7 are derived by first minimizing equation 2.9 with respect to the Moho topography h_{ilm} using the positive coefficients of the Moho topography C_{ilm}^{+} (equation 2.8). What this does is to reduce the gravitational potential misfit between the observed and modeled

gravity so that the geoid from the Moho topography matches the Bouguer anomaly. Given that this study on subsurface structure is an inverse problem, the method is to minimize the misfit so that the model fits the available data. Here, I reproduce the step-by-step derivation of equation 2.6 (heart of the code) from equations 2.8 and 2.9.

1) Start by substituting the entire equation 2.8 of C_{ilm}^{+} for the C_{ilm}^{D} term in equation 2.9, this inputs the coefficients of the Moho topography at the reference radius of D:

$$\Phi = \left[C_{ilm}^{BA} - C_{ilm}^{D} \left(\frac{D}{R}\right)^{l} \right]^2 + \lambda (h_{ilm})^2$$

$$\Phi = \left[C_{ilm}^{BA} - \frac{4\pi\Delta\rho D^3}{M(2l+1)} \sum_{n=1}^{l+3} \frac{{}^{n}h_{ilm}}{D^n n!} \frac{\prod_{j=1}^{n}(l+4-j)}{(l+3)} \left(\frac{D}{R}\right)^{l} \right]^2 + \lambda (h_{ilm})^2 \tag{2.10}$$

2) Minimizing Φ with respect to h_{ilm} (setting derivative to equal 0) and ignoring higher-order terms (when evaluating the relief along density contrast surfaces such as the crust-mantle boundary that are smaller than the regions studied, the first-order terms are sufficient, so it is acceptable to ignore higher-order terms) :

$$\frac{d\Phi}{dh_{ilm}} = 2\left[C_{ilm}^{BA} - \frac{4\pi\Delta\rho D^3}{M(2l+1)} \sum_{n=1}^{l+3} \frac{{}^{n}h_{ilm}}{D^n n!} \frac{\prod_{j=1}^{n}(l+4-j)}{(l+3)} \left(\frac{D}{R}\right)^{l} \right] \text{x} \left[-\left(\frac{4\pi\Delta\rho D^3}{M(2l+1)}\right) \left(\frac{D}{R}\right)^{l} \right] + 2\lambda (h_{ilm}) = 0 \tag{2.11}$$

3) Pulling the *n* = 1 term out of summation:

$$\frac{d\Phi}{dh_{ilm}} = \left[C_{ilm}^{BA} - \frac{4\pi\Delta\rho D^3}{M(2l+1)} \left(\frac{{}^{1}h_{ilm}}{D^1 1!} \frac{\prod_{j=1}^{1}(l+4-1)}{(l+3)} \left(\frac{D}{R}\right)^{l} \right.\right.$$

$$+\sum_{n=2}^{l+3}\frac{{}^{n}h_{ilm}}{D^{n}n!}\frac{\prod_{j=1}^{n}(l+4-j)}{(l+3)}\left(\frac{D}{R}\right)^{l}\Bigg)\Bigg]\ \text{x}\ \left[-\left(\frac{4\pi\Delta\rho D^{3}}{M(2l+1)}\right)\left(\frac{D}{R}\right)^{l}\right]\left[\frac{1}{D}\right]+\lambda(h_{ilm})=0$$

(2.12)

$$\frac{d\Phi}{dh_{ilm}}=\left[C_{ilm}^{BA}-\frac{4\pi\Delta\rho D^{3}}{M(2l+1)}\left\{\frac{{}^{1}h_{ilm}}{D}\left(\frac{D}{R}\right)^{l}+\sum_{n=2}^{l+3}\frac{{}^{n}h_{ilm}}{D^{n}n!}\frac{\prod_{j=1}^{n}(l+4-j)}{(l+3)}\left(\frac{D}{R}\right)^{l}\right\}\right]$$
$$\text{x}\ \left[-\left(\frac{4\pi\Delta\rho D^{3}}{M(2l+1)}\right)\left(\frac{D}{R}\right)^{l}\right]\left[\frac{1}{D}\right]+\lambda(h_{ilm})=0$$

(2.13)

4) Pulling the $\left(\frac{D}{R}\right)^{l}$ term out and multiplying by the $-\frac{M(2l+1)}{4\pi\Delta\rho D^{3}}\left(\frac{R}{D}\right)^{l}D$ term:

$$\frac{d\Phi}{dh_{ilm}}=\left[C_{ilm}^{BA}-\frac{4\pi\Delta\rho D^{3}}{M(2l+1)}\left(\frac{D}{R}\right)^{l}\left(\frac{{}^{1}h_{ilm}}{D}+\sum_{n=2}^{l+3}\frac{{}^{n}h_{ilm}}{D^{n}n!}\frac{\prod_{j=1}^{n}(l+4-j)}{(l+3)}\right)\right]$$
$$-\left(\frac{M(2l+1)}{4\pi\Delta\rho D^{3}}\right)\left(\frac{R}{D}\right)^{l}D\lambda(h_{ilm})=0$$

(2.14)

5) Now multiplying by $\left(\frac{M(2l+1)}{4\pi\Delta\rho D^{3}}\right)\left(\frac{R}{D}\right)^{l}D$ on both sides of the equation:

$$\frac{d\Phi}{dh_{ilm}}=\left[C_{ilm}^{BA}\left(\frac{M(2l+1)}{4\pi\Delta\rho D^{2}}\right)\left(\frac{R}{D}\right)^{l}-\left(h_{ilm}+D\sum_{n=2}^{l+3}\frac{{}^{n}h_{ilm}}{D^{n}n!}\frac{\prod_{j=1}^{n}(l+4-j)}{(l+3)}\right)\right]$$
$$-\left[\left(\frac{M(2l+1)}{4\pi\Delta\rho D^{3}}\right)\left(\frac{R}{D}\right)^{l}\right]^{2}D^{2}\,\lambda(h_{ilm})=0$$

(2.15)

6) Rearranging:

$$\frac{d\Phi}{dh_{ilm}}=\left[C_{ilm}^{BA}\left(\frac{M(2l+1)}{4\pi\Delta\rho D^{2}}\right)\left(\frac{R}{D}\right)^{l}-D\sum_{n=2}^{l+3}\frac{{}^{n}h_{ilm}}{D^{n}n!}\frac{\prod_{j=1}^{n}(l+4-j)}{(l+3)}\right]$$

$$= h_{ilm} + \left[\left(\frac{M(2l+1)}{4\pi\Delta\rho D^2}\right)\left(\frac{R}{D}\right)^l\right]^2 \lambda(h_{ilm})$$

(2.16)

$$\frac{d\Phi}{dh_{ilm}} = \left[C_{ilm}^{BA}\left(\frac{M(2l+1)}{4\pi\Delta\rho D^2}\right)\left(\frac{R}{D}\right)^l - D\sum_{n=2}^{l+3}\frac{{}^n h_{ilm}}{D^n n!}\frac{\prod_{j=1}^{n}(l+4-j)}{(l+3)}\right]$$

$$= h_{ilm}\left\{1+\lambda\left[\frac{M(2l+1)}{4\pi\Delta\rho D^2}\left(\frac{R}{D}\right)^l\right]^2\right\} = (h_{ilm})\omega_l{}^{-1}$$

(2.17)

since the filter $\omega_l{}^{-1}$ is:

$$\omega_l{}^{-1} = \left\{1+\lambda\left[\frac{M(2l+1)}{4\pi\Delta\rho D^2}\left(\frac{R}{D}\right)^l\right]^2\right\}$$

7) Solving for h_{ilm} :

$$h_{ilm} = \omega_l\left[C_{ilm}^{BA}\left(\frac{M(2l+1)}{4\pi\Delta\rho D^2}\right)\left(\frac{R}{D}\right)^l - D\sum_{n=2}^{l+3}\frac{{}^n h_{ilm}}{D^n n!}\frac{\prod_{j=1}^{n}(l+4-j)}{(l+3)}\right]$$

Thus giving Wieczorek and Phillips (1998) equation 18, or here equation 2.6 with 2.7.

2.6.2 Using Rapp's Isostacy

Now that I have derived the original equation used in the MCT code, I want to incorporate the isostatic factor into the program. The isostatic equation I use in the modified program called *MarsIsostacy* is Rapp's (1989) equation below:

1) Rapp's (1989) isostacy equation, equation 9, modified by using $\rho_{mean} = \frac{3M}{4\pi R^3}$:

$$C_{ilm}^{I} = \left(\frac{4\pi R^3}{2l+1}\right)\frac{\rho_{cr}}{M}\left\{\left[1-\left(\frac{R-D}{R}\right)^{l}\right]h_{lm\alpha} + \left(\frac{l+2}{2}\right)\left[1+\frac{\rho_{cr}}{\Delta\rho}\left(\frac{R-D}{R}\right)^{l-3}\right]h2_{lm\alpha} + \left(\frac{(l+2)(l+1)}{6}\right)\left[1-\frac{{\rho_{cr}}^2}{\Delta\rho^2}\left(\frac{R-D}{R}\right)^{l-6}\right]h3_{lm\alpha}\right\} + \ \ldots$$

(2.18)

where C_{ilm}^{I} are the spherical harmonic coefficients for isostacy, ρ_{cr} is the density of the crust, ρ_{mean} is the mean density of Mars (3930 kg/m^3), $\Delta\rho$ is the density contrast across the crust-mantle boundary, and $h_{lm\alpha} = h_{ilm} / R$ is the Moho topography, but in different notation in Rapp (1989). The subsequent terms after the first and second addition signs are the higher order terms, indicated by the multiplication of $h2_{lm\alpha}$ and $h3_{lm\alpha}$, representing the second higher order terms and third higher order terms, respectively. The reader is cautioned that in Wieczorek and Phillips' (1998) formulation, the h_{ilm}'s are the spherical harmonic coefficients of the Moho topography, while in Rapp's (1989) formulation, the $h_{lm\alpha}$'s are the spherical harmonic coefficients of the Moho topography. To derive Rapp's equation above, I start with the same expression for the potential coefficients given in equation 2.8. Instead of solving for the coefficients of the Moho topography as in Wieczorek and Phillips (1998), I use the following relationship between the Moho topography and the surface topography coefficients:

$$m_{ilm} = \frac{\rho_{cr}}{\rho_{mantle} - \rho_{cr}}\frac{R^2}{(R-D)^2}t_{ilm}$$

(2.19)

which results from balancing the pressure due to a spherical shell of crustal rock of crustal density ρ_{cr} with a crustal thickness of D. Then I expand using the binomial theorem used by Wieczorek and Phillips (1998). The last part of equation 2.18 trails off to represent even higher order terms that would be truncated as those higher order terms do not make much of a difference in the resulting crustal thickness models. While

Wieczorek and Phillips (1998) retain all the terms in the binomial expansion, Rapp (1989) only includes the first three terms, showing that the high-order terms are negligible. Often in geophysical problems, only the first term is used. Note that these higher order terms impact the isostatic geoid anomaly, but not the crustal thickness. This is the isostatic equation to be applied to the modified MCT code (*MarsIsostacy*) to generate isostatic crustal thickness models.

2.7 The Crustal Thickness Model Code

In studying the Martian gravity field and topography, Mark Wieczorek's Mars Crustal Thickness Program (MCT) is used. It is a FORTRAN95 program compiled with built-in modules and subroutines from the SHTOOLS library. After the initial declaration of variables, a number of parameters are set and the code prompts the user for various input parameters. Then, the gravity and topography files are read. For my work, the gravity model is jgm85h02.sh, a gravity model of Mars with maximum spherical harmonic (SH) degree lmax = 85, obtained from Mars Global Surveyor (MGS) Radio Science experiment tracking (Neumann et al., 2004; Nunes et al., 2009; Zuber et al, 2004). The topography model is Mars2000.shape (Smith et al., 2001), a topography model of Mars with maximum SH degree and order lmax and nmax = 90, obtained from the Mars Orbiting Laser Altimeter (MOLA) instrument onboard MGS. The gravity coefficients are then downward continued starting from the model radius of 3397 km down to the mean planetary radius (MPR) in the harmonic domain. Next, the Bouguer Anomaly, *ba*, is calculated: $ba = pot - bc$, where the Bouguer Anomaly equals to the gravitational potential, *pot*, minus the Bouguer Correction, *bc*.

The next section of the code computes the crustal thickness using iteration at each reference Moho radius. The change in thickness, thick_delta, reference Moho radius, D, and Moho coefficients are stated. Degree *l* is set to be 1 and the Moho coefficient is calculated to be the Bouguer Anomaly times Mars' mass times the reference radius to the *l* degree power, and divided by 4π times the density difference times D^2, this gives:

$$h_{ilm} = C_{ilm}^{BA}\left(\frac{M(2l+1)}{4\pi\Delta\rho D^2}\right)\left(\frac{R}{D}\right)^l \tag{2.20}$$

where $\Delta\rho$ (or rho_l - rho_u) is the density difference and in the code, rho_l is the mantle density and rho_u is the crustal density. This means that the Moho coefficient are the product of the Bouguer Anomaly and Mars' mass divided by the surface area and density contrast across the crust-mantle boundary.

The **MakeGridGLQ** subroutine is then called to create a 2-dimensional gridded map of the Moho radius, using the Moho grid file and calculated Moho coefficients. From here, another gravity subroutine, **Hilm** (not to be confused with the h_{ilm} term in the earlier equations) is called to iteratively calculate the relief along an interface that corresponds to a given Bouguer Anomaly, using the algorithm explained in section 2.6. This function specifically uses equation 18 from Wieczorek and Phillips (1998) (equation 2.6 here). It makes a guess at the relief and outputs better SH coefficients, then iteratively inputs the next guess, and so forth. Then **MakeGridGLQ** is called again to create the resulting 2-dimensional gridded Moho relief maps.

The last section of the code calculates the gravity misfit values between the observed and calculated gravity. Here, the Moho coefficients are upward continued from the Moho radius D up to the mean planetary radius R. The gravity misfit is then calculated as the gravitational potential minus the Bouguer Correction minus the coefficient array cilm → misfit = pot – (bc + cilm). Now, the coefficient array is calculated for the misfit array by multiplying the misfit array with GM/R^2.

The last part of the program prints out the Mean Crustal Thickness in km and output data. Each input parameter and selected values are explained and summarized in Table 2.1 below:

1) Crustal density and 2) mantle density values, which will determine the density contrast of the relief. This has been set to ρ_c = 2900 kg/m^3 and ρ_m = 3500 kg/m^3, for the crust and mantle, respectively as explained in earlier sections, giving a crust-mantle interface density contrast of $\Delta\rho$ = 600 kg/m^3.

3) An assumed minimum crustal thickness, in order to anchor the model so that the resulting thickness map will not exhibit negative thicknesses; this is set to 5 km so that the lowest elevations on Mars in Hellas Basin and Isidis Basin will have either a minimum thickness of zero or a positive thickness. This value is also consistent with values used by similar studies (Zuber et al., 2000 and Neumann et al., 2004).

4) The filter type applied to the calculation, which includes minimum amplitude, minimum curvature, or no filter. The filter is basically a downward continuation filter to constrain how much the short wavelength topography will be filtered (Wieczorek and Phillips, 1998). My experiments show that selecting either the minimum amplitude or the minimum curvature filter does not affect the resulting crustal thickness, thus for all results the minimum amplitude filter type is used.

5) The degree l at which the filter is one-half (0.5), only for when a filter is selected above. This is the degree value at which the power of the error spectrum of the gravitational potential field equals the power of the gravitational potential spectrum. In other words, this degree value sets the strength of the potential field and its error to be the same. This happens at about degree $l = 50$ for Mars. However, degree $l = 10$ is another end value used, which shows regional and global scale features without being overwhelmed by the dichotomy feature (a degree $l = 1$ feature). Any degrees lower than 10 will start getting overwhelmed by larger structures and any degrees higher than 50 will not necessarily show the smaller-wavelength features. Thus the experiments generally used degrees between the end members of 10 and 50.

6) The maximum degree to compute the Moho relief to; this is the degree that correlates the power spectrum of the Moho relief with the power spectrum of the surface topography. This is set to degree $l = 50$; degrees higher than this will not have any significant effects on the resulting crustal thickness.

7) Remove degree-1 topography coefficients from Bouguer Correction? This will remove the spherical harmonic coefficients corresponding to the topographic dichotomy structure when calculating the Bouguer anomaly. Usually, the choice is to select ‘no’ so that the resulting crustal thickness will show the dichotomy feature. Experiments described in Chapter 3 will show what setting this parameter to ‘yes’ (or removal of the degree-1 topography coefficients) will do to the crustal thickness.

8) Grid spacing for output crustal thickness map. This is set to 1°.

Table 2.1 Summary of Model Input Parameters in MCT code

Model Input Parameter	**Value**
1) Crustal density ρ_c	2900 kg/m^3
2) Mantle density ρ_m	3500 kg/m^3
3) Assumed minimum crustal thickness	5 km
4) Filter type	Minimum amplitude
5) Degree l at which filter is 0.5	10 and 50
6) Maximum degree l to compute Moho to	50
7) Removal of degree 1topo coefficients from Bouguer Correction?	no
8) Grid spacing for output crustal thickness map	1°

2.8 Data

The two main types of data used in the MCT program are a spherical harmonic expansion of the global topography field and a spherical harmonic expansion of the gravitational potential field. The data were collected by the Mars Global Surveyor spacecraft; the topographic files from the Mars Orbiting Laser Altimeter (MOLA) instrument and the gravity files from the Radio Science Subsystem instrument. They are available for download through the Planetary Data System (PDS) Geosciences Node website: http://pds-geosciences.wustl.edu/dataserv/default.htm. Both types of data are expanded in spherical harmonic coefficients in ASCII format (specific files and their spatial resolution are listed in Table 2.2). The MCT code uses an older version of the topography (Mars2000.shape) and gravity (jgm85h02.sh) data files (Neumann et al., 2004; Nunes et al., 2009; Smith et al., 2001; Zuber et al, 2004), so I obtained newer versions (MarsTopo719.shape and jgm95j01.sha) of the same type of files (Wieczorek, 2007) and compiled and ran the code with the newer files for comparison. Given that there is little difference between the two versions of the gravity files (note virtually no

difference in Figures 2.6 and 2.7) and except for the slightly different resolution of the topography files (see the lack of difference in Figures 2.8 and 2.9 for comparison), I proceed using the original file versions already in place in the code.

In addition to crustal thickness maps, I have modified the MCT code so that it computes and produces gravity misfit maps, which show the difference between the observed and modeled gravity, allowing me to analyze anomalies that may be present (this is shown as the last part of the code discussed earlier). I have also generated two reference maps, a topographic map using MOLA data (Figure 2.8, Mars2000.shape file and Figure 2.9, MarsTopo719.shape file), a geoid/areoid map using MGS data (Figure 2.6, jgm85h02.sh file and Figure 2.7, jgm95j01.sha file), and gravity maps showing both Free Air gravity and Bouguer gravity (Figures 2.3 and 2.4) anomalies, with and without the rotational flattening term, from the gravitational potential model using the same jgm85h02.sh potential file. All maps computed from the MCT code are generated by the Generic Mapping Tool (or GMT) mapping software created by Paul Wessel and Walter H. F. Smith. GMT is also freely available software for download at this website: http://gmt.soest.hawaii.edu/. All maps are presented in Hammer projection, with maps centered at 0°, 0° (Figures 1.2, 2.3) with the Tharsis Rise region in the western hemisphere, along the equator, and Hellas Basin in the southeast quadrant of the map, unless otherwise noted. Topographic, crustal thickness, and geoid maps are in kilometers (km) and gravity misfit maps are in milligals (mgal).

Table 2.2 Data files used in MCT code

File Name	Data Type	Resolution	Source
Mars2000.shape (original)	topographic spherical harmonic coefficients	SH degree 90 or ~237 km	MOLA, MGS, Greg Neumann
jgm85h02.sh (original)	gravity/potential spherical harmonic coefficients	SH degree 85 or ~250 km	Radio Science Subsystem, MGS
MarsTopo719.shape (newer)	topographic spherical harmonic coefficients	SH degree 719 or ~30 km	MOLA, MGS, Mark Wieczorek
jgm95j01.sha (newer)	gravity/potential spherical harmonic coefficients	SH degree 95 or ~224 km	Radio Science Subsystem, MGS

Figure 2.1

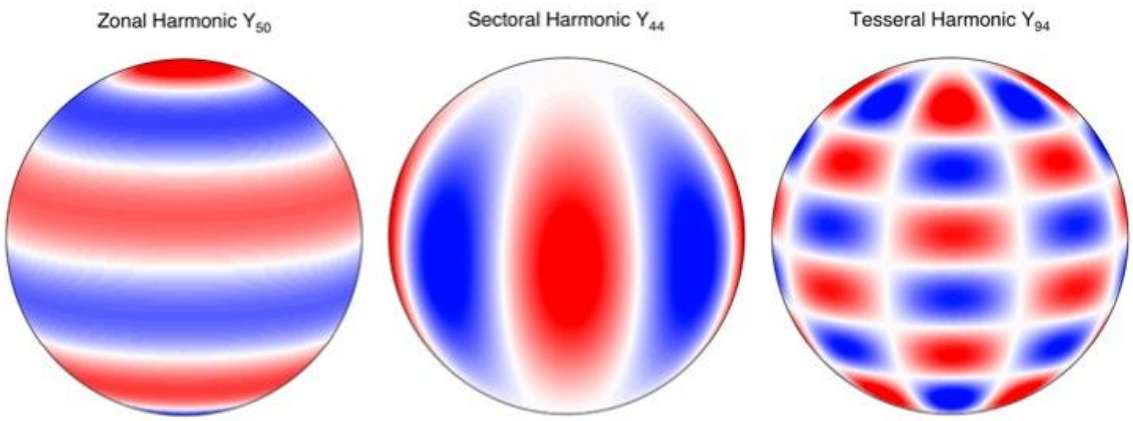

Schematic examples of spherical harmonic diagrams: zonal, sectoral, and tesseral harmonics. Red indicates positive while blue is negative. Here, the Zonal harmonic has degree $l = 5$ and order $m = 0$, the Sectoral harmonic has degree $l = 4$ and order $m = 4$, and the Tesseral harmonic has degree $l = 9$ and order $m = 4$.

Figure 2.2

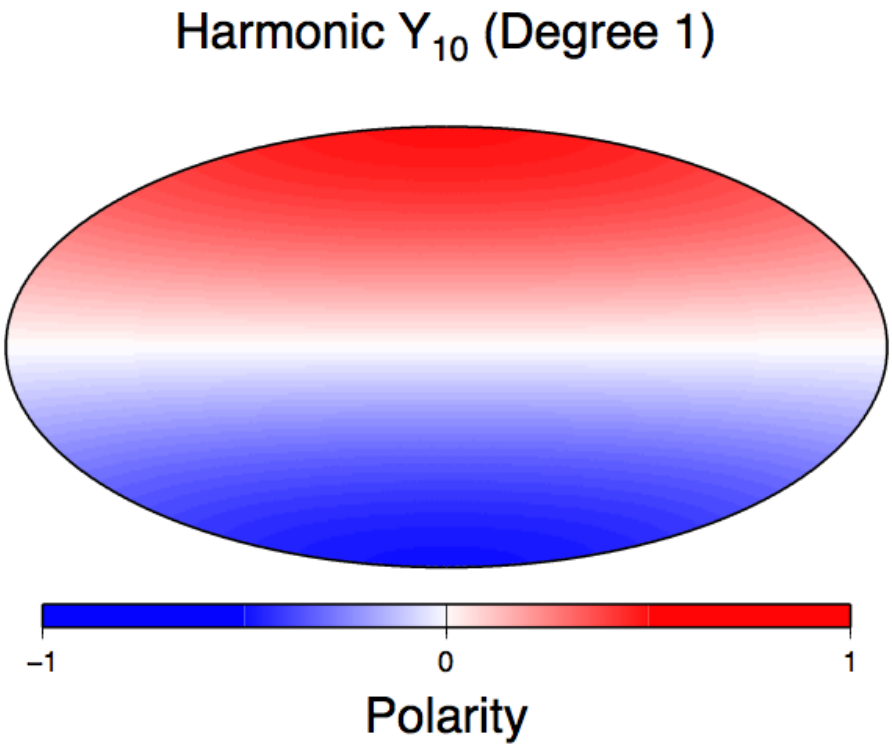

Example of a degree $l = 1$, order $m = 0$ harmonic feature, such as Mars' topographic dichotomy.

Figure 2.3

a. Free Air anomaly with Flattening Factor

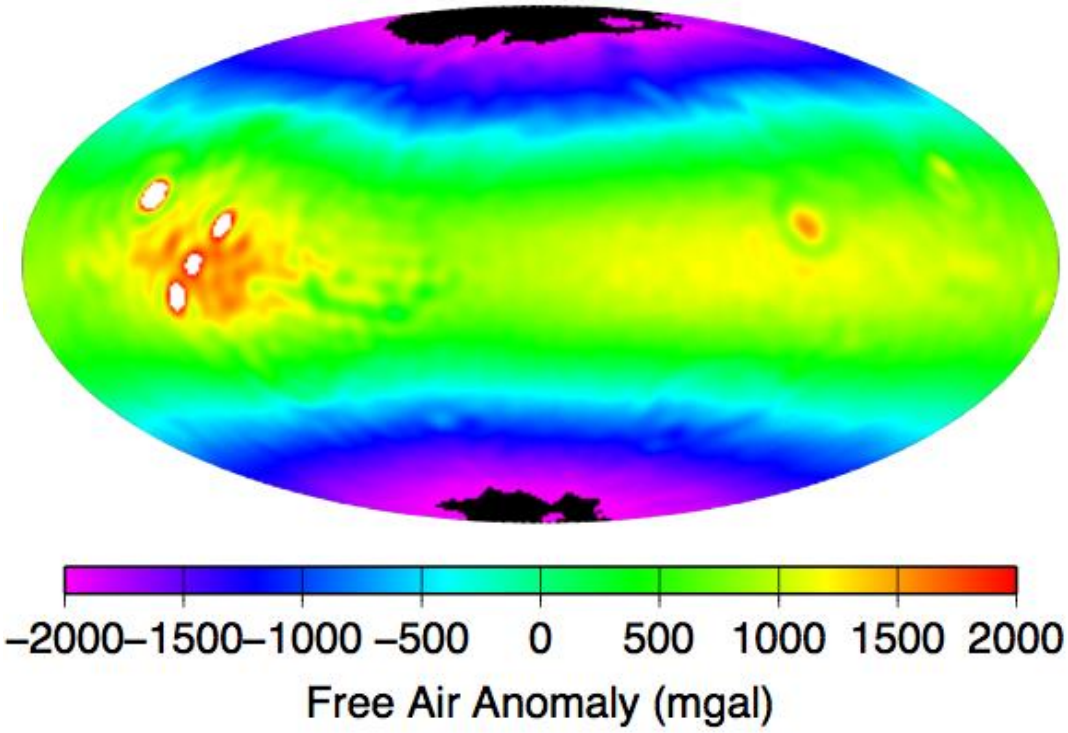

b. Free Air anomaly without Flattening Factor

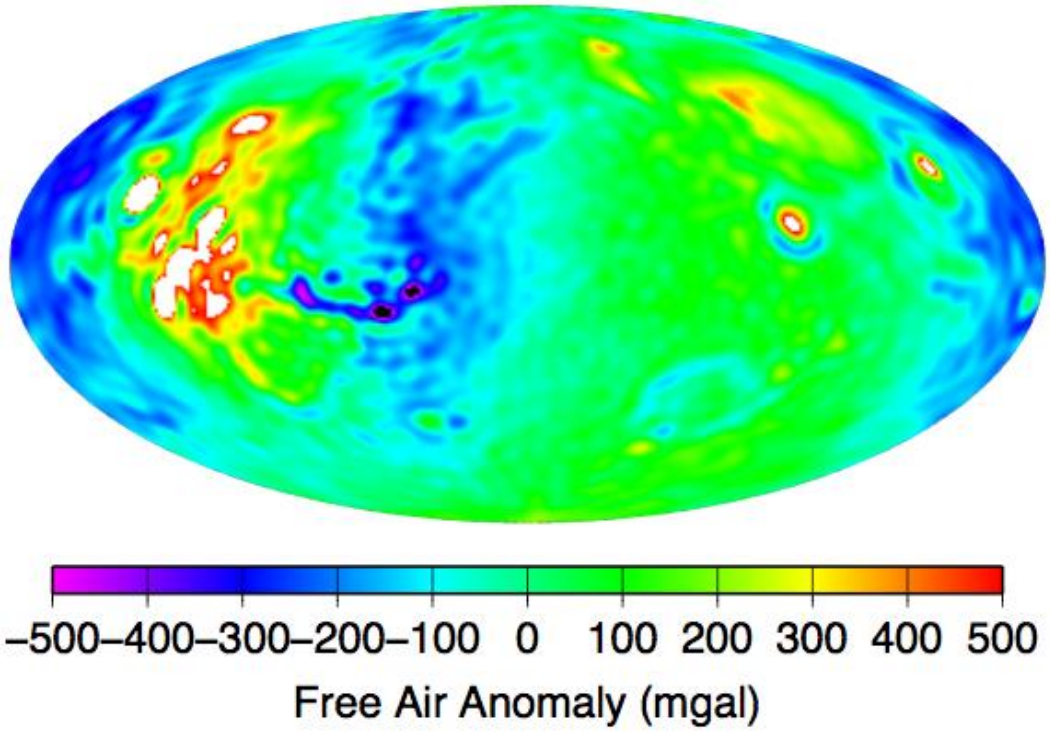

Figure 2.3 (con't.)

a) The Free Air gravity anomaly map generated by the *jgm85h02.sh* gravity potential file. The J_2 term is not removed here thus a degree-2, order-0 structure is prominent with the largest anomaly at the equatorial region, with a bulge at the equator and flattened at both poles, relating to the flattening factor from the planet's rotation. This and subsequent figures are generated with GMT mapping software in Hammer projection centered at 0°,0°, using the geoid data file *jgm85h02.sh*, obtained from the Radio Science Subsystem instrument onboard the Mars Global Surveyor spacecraft (unless otherwise noted). **b)** The Free Air gravity anomaly map with the J_2 term removed. Now the degree-2, order-0 flattening factor is no longer present. Notice the scale is smaller, indicating that a large portion of the Free Air gravity anomaly comes from that degree-2, order-0 flattening term.

Figure 2.4

a. Bouguer anomaly with Flattening Factor

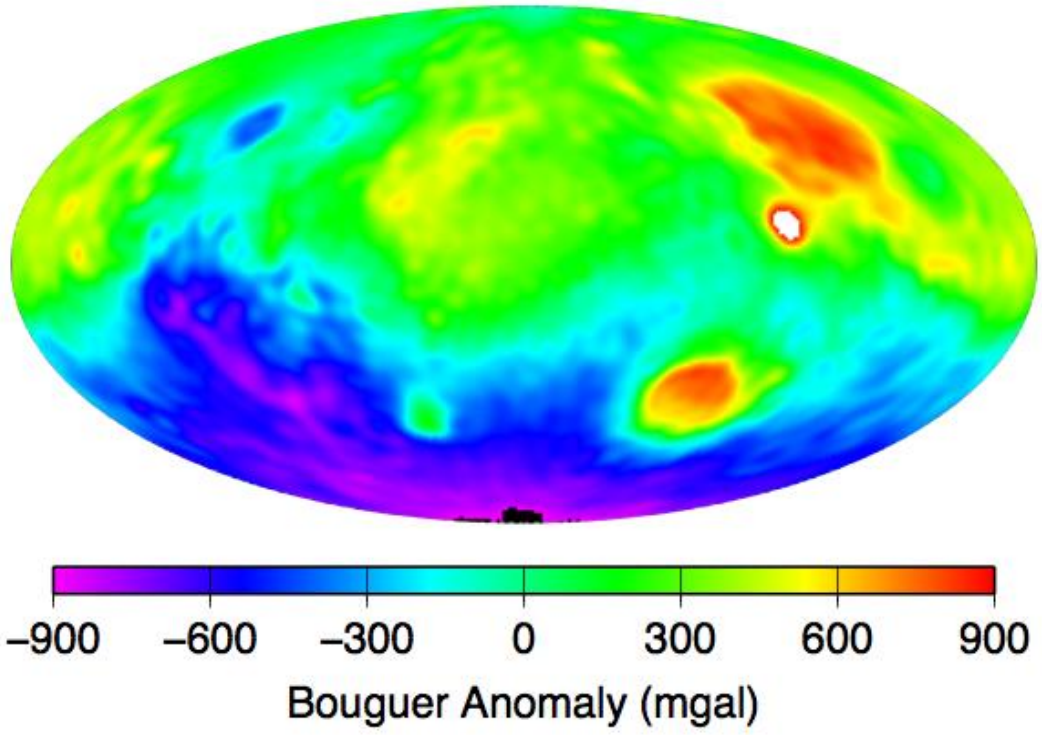

b. Bouguer anomaly without Flattening Factor

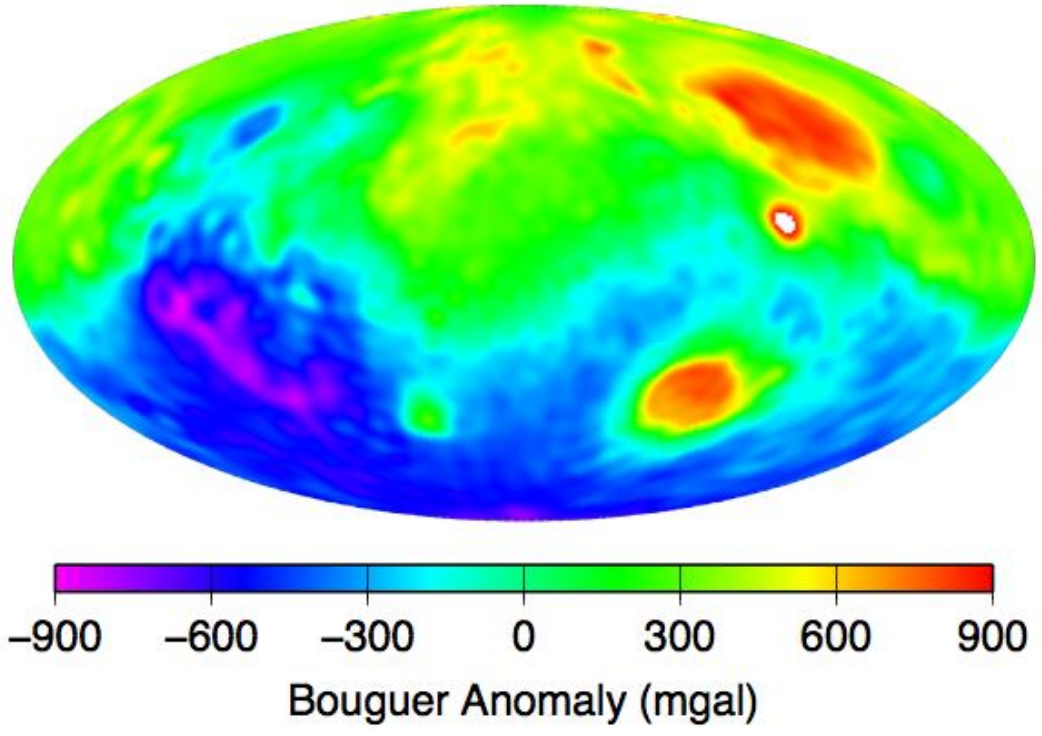

Figure 2.4 (con't.)

a) The Bouguer gravity anomaly map generated by the *jgm85h02.sh* gravity potential file. The J_2 term is not removed here and a prominent degree-1 structure is shown, corresponding to the degree-1 structure of the Martian topography. Note the largest anomaly occurs in the red regions (Utopia, Isidis, and Hellas Basins) and the purple regions from the South Pole leading a track-like pattern toward the Tharsis Rise volcanic region, northwest of the South Pole toward the equator. **b)** The Bouguer gravity anomaly map with the J_2 term removed. Removing the flattening factor has very minor changes to the overall Bouguer anomaly pattern, with lower anomaly values near the South Pole and higher anomaly values in the Northern Lowlands.

Figure 2.5

a. Non-isostatic

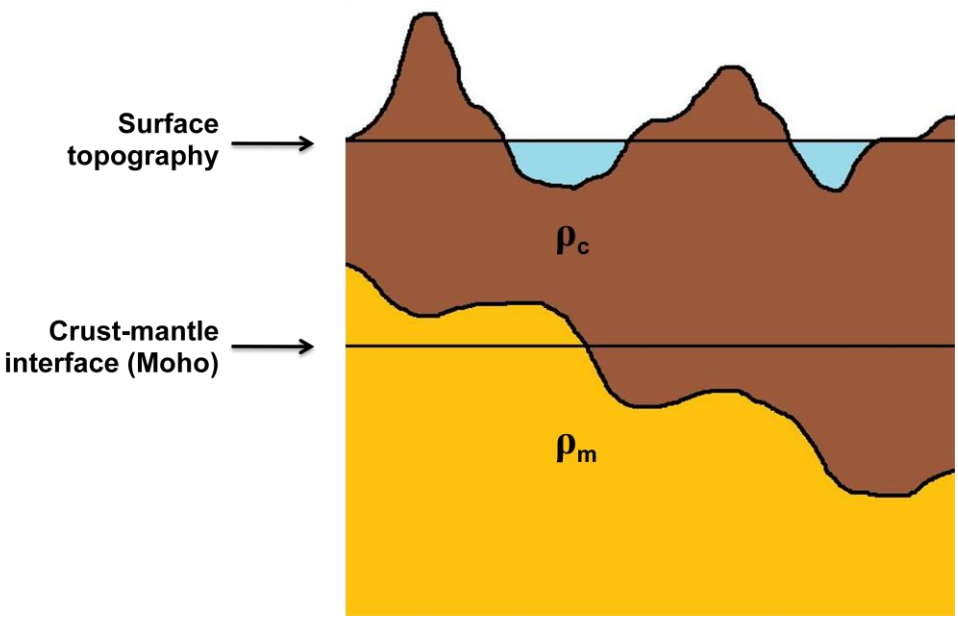

b. Airy-isostatic

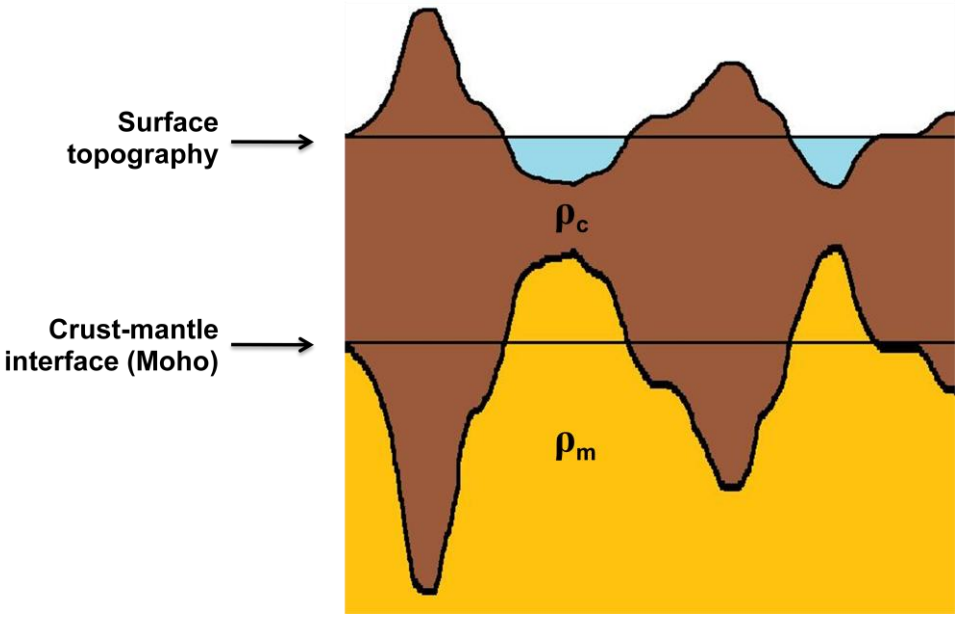

Figure 2.5 (con't.)

Representation of the crust (brown) and mantle (yellow) in **a)** a non-isostatic state, where the Moho topography is variable and **b)** an Airy-isostatic equilibrium, where the Moho topography is a mirror-image of the surface topography, scaled by the density contrast between the crust and mantle. ρ_c and ρ_m are the uniform crustal and mantle densities, respectively. The horizontal lines indicate the average surface topography (datum) or average Moho topography. Figures drawn by Karina Cheung, 2011.

Figure 2.6

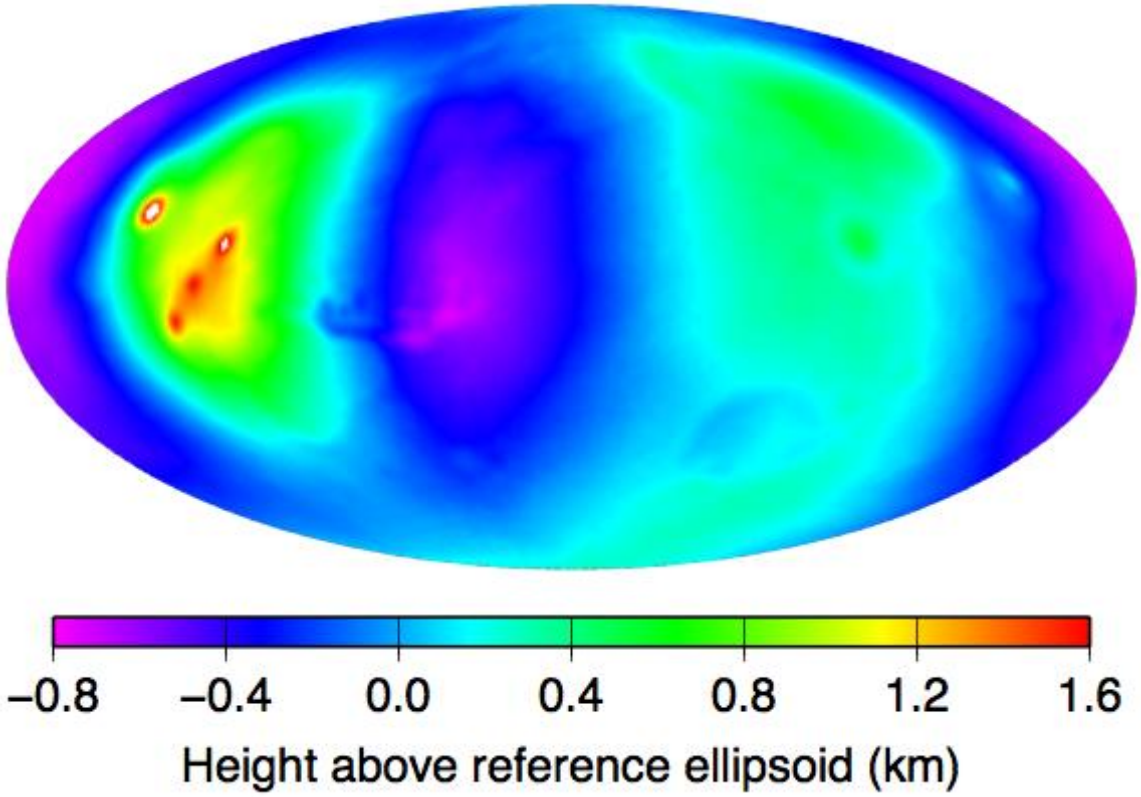

The areoid of Mars, relative to a reference ellipsoid, showing prominent mass excess in the Tharsis volcanic region and the region above Hellas Basin in the northeast and mass deficit elsewhere on the planet. This is generated using the geoid data file *jgm85h02.sh*, obtained from the Radio Science Subsystem instrument onboard the Mars Global Surveyor spacecraft. The data is recorded in spherical harmonic coefficients, converted to kilometers in GMT and has an approximate spatial resolution of 250 km. Original file includes the rotational flattening J_2 term, which has been removed to produce this map.

Figure 2.7

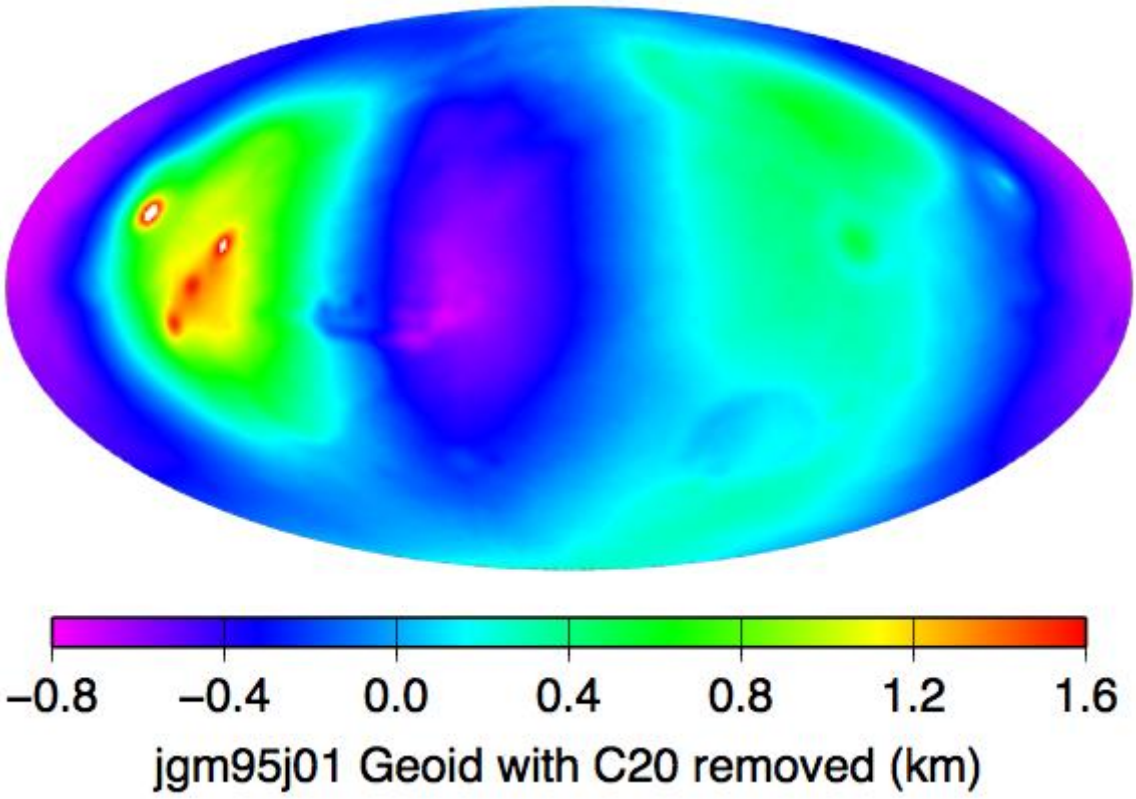

The areoid of Mars, using the geoid data file *jgm95j01.sha*, obtained from the Radio Science Subsystem instrument onboard the Mars Global Surveyor spacecraft. The data is recorded in spherical harmonic coefficients, converted to kilometers in GMT and has an approximate spatial resolution of 224 km. Original file includes the rotational flattening J_2 term, which has been removed to produce this map.

Figure 2.8

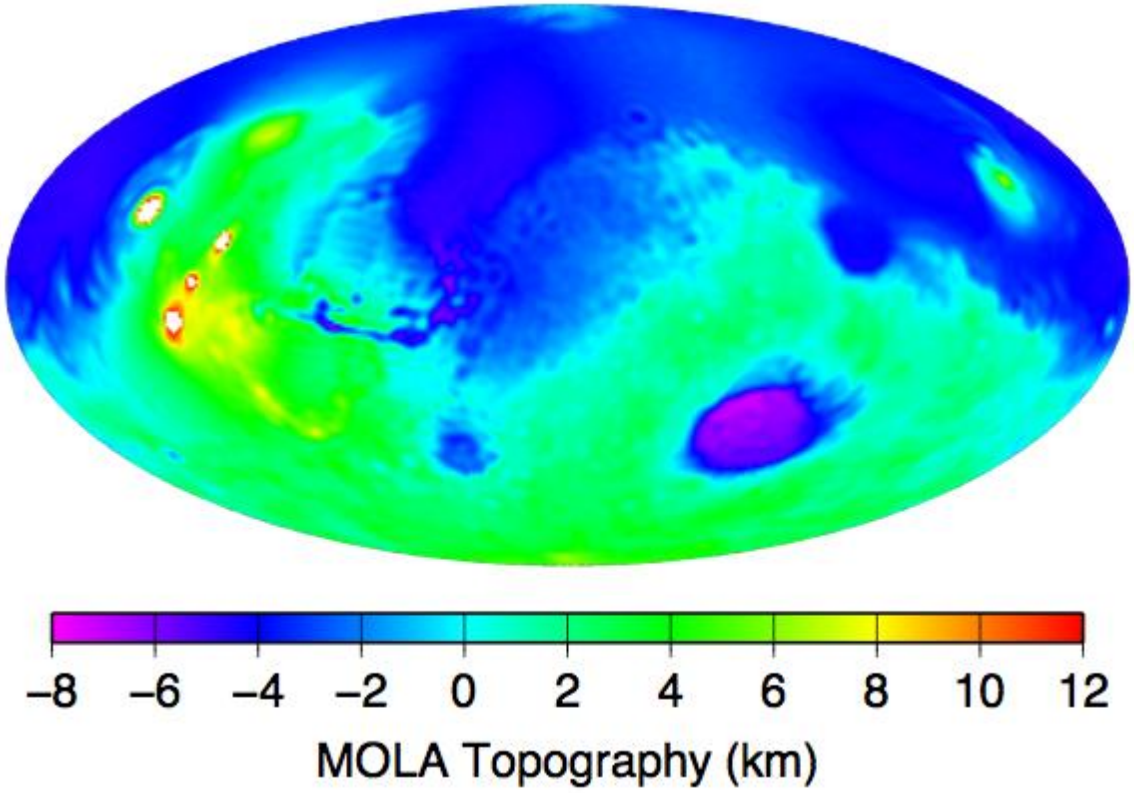

Topographic map of Mars using the data file *Mars2000.shape* obtained from the Mars Orbiter Laser Altimeter (MOLA) instrument onboard the Mars Global Surveyor spacecraft. The data is recorded in spherical harmonic coefficients and converted to kilometers in GMT and has an approximate spatial resolution of 237 km. Note the prominent crustal dichotomy running along the equator that divides the planet into two distinct hemispheres. Original file includes the rotational flattening J_2 term, which has been removed to produce this map.

Figure 2.9

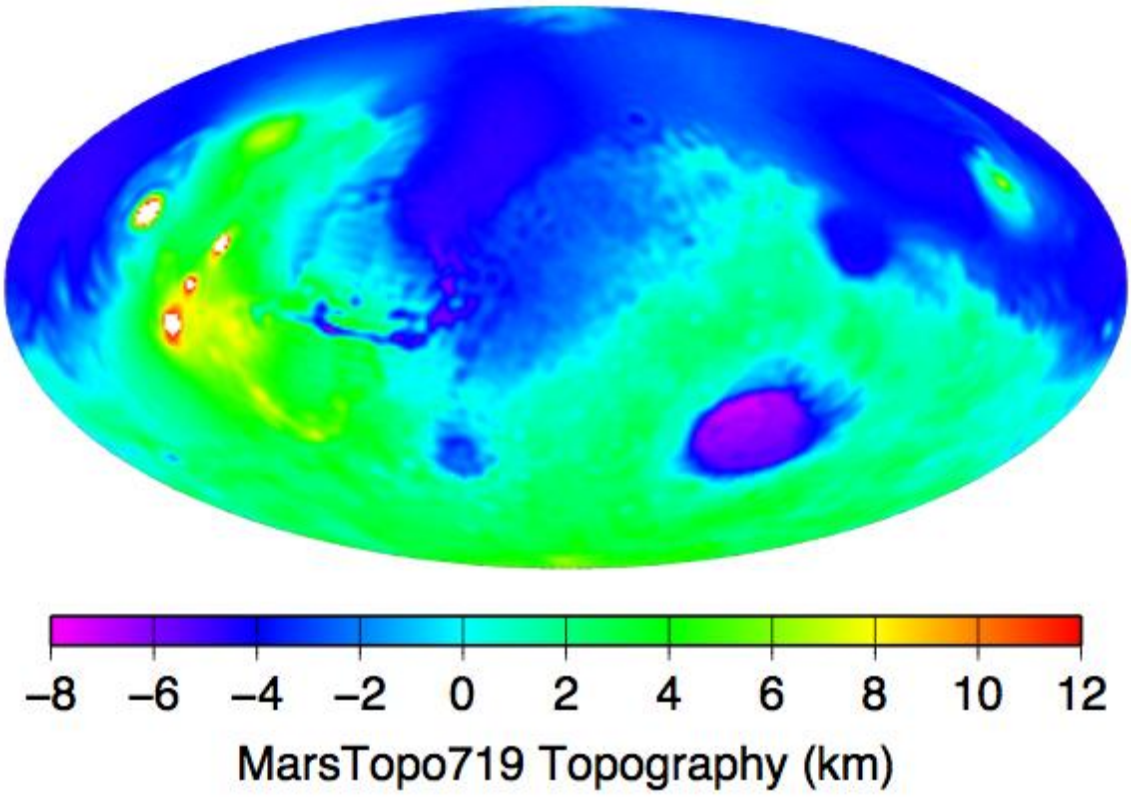

Topographic map of Mars using the data file *MarsTopo719.shape* obtained from the Mars Orbiter Laser Altimeter (MOLA) instrument onboard the Mars Global Surveyor spacecraft. The data is recorded in spherical harmonic coefficients and converted to kilometers in GMT and has an approximate spatial resolution of 30 km. Original file includes the rotational flattening J_2 term, which has been removed to produce this map.

Chapter 3: Results

3.1 Preliminary Studies

3.1.1 Is Mars Isostatic?

For a planet to have a global-scale feature such as the topographic/crustal dichotomy, first thing that comes to mind is whether the planet is isostatic or not, what would the crust look like if it was isostatic, and if it is a result of a potential planet-scale impact, which I will discuss in section 3.6. When a planet-scale object impacts the planet, not unlike the hypothesized impact of the Earth that explained the origin of the Moon (Canup and Asphaug, 2001), several possibilities arise. If the impactor is large enough, most of the planet's mass could be obliterated and/or some mass may be expelled into space and coalesce to form a natural satellite. One scenario would be an impactor that hits the planet, creating a large-scale impact basin, such as the Borealis Basin or Utopia Planitia region, forming the Northern Lowlands on Mars, creating the hemispheric difference in elevation. At this scale, the massive impact object would hit the planet so hard that the entire crust gets depressed into the mantle, and/or melts and mixes with the mantle. If the crust can stay intact, some of the crustal material could rebound elastically and isostatically whereas some other parts of the crust would not. Some crustal material could also be homogenized with mantle material that it would be difficult to distinguish the geologic units chronologically to infer about the geologic history, as that record would be erased and the landscape would be resurfaced.

In the first part of this section, I experiment with the crustal thickness models and test them to see if Mars' crust can be considered isostatic or not. If so, where are the regions that are isostatic and non-isostatic and why? Lastly, what do the isostatic regions and non-isostatic regions imply about internal properties such as mantle dynamics, crustal behavior, and the thermal history of the planet.

In section 2.4, I talked about the two types of isostacy and that Wieczorek and Phillips (1998)'s method in the Mars Crustal Thickness program does not assume isostacy. Therefore we have modified the program and renamed it MarsIsostacy program

using the Airy isostatic equation from Rapp (1989) so that results generated are isostatic. The algorithm in the Mars Crustal Thickness code contains a part that iterates until the gravity misfit becomes less than 1 mgal and maintains a minimum crustal thickness. In this modified, isostatic version that part of the iteration loop is taken out as that iteration is not needed. The program calculates for the Moho topography to equal the surface topography, but scaled by the crust-mantle density contrast, which is what Airy isostacy is, explained in section 2.4. The program calculates the Moho topography using equation 2.19:

$$m_{ilm} = \frac{\rho_{cr}}{\rho_{mantle} - \rho_{cr}} \frac{R^2}{(R-D)^2} t_{ilm}$$

where t_{ilm} is the spherical harmonic coefficients of the surface topography for degree *l* and order *m*, m_{ilm} is the spherical harmonic coefficients of the Moho topography for degree *l* and order *m*, *R* is the reference radius, and *D* is the depth. The above equation comes from the balancing of the pressure due to a spherical shell of crustal rock, as discussed in section 2.6.2. The following model results are generated using this MarsIsostacy program.

3.1.2 The Rotational Flattening Component

When I first modeled the crustal thickness using the MarsIsostacy program, the resulting model looked very odd in that the thickness map did not show the crustal dichotomy at all. Instead, it had a band of much thicker crust surrounding the equatorial region and thinning toward both poles (Figure 3.1a). It turns out that one of the biggest components that contributes to the global crustal shape of the planet is the planetary rotational flattening factor, which is what I was seeing in Figure 3.1a. The flattening factor *f* is the difference between the equatorial radius and the polar radius, divided by the equatorial radius. With most near-spherical planetary bodies, the equatorial radius is usually larger than the polar radius due to the rotation of the body. Along with centrifugal force, the rotating mass of the body is distributed outward, creating a bulge in the equatorial region and thus flattening at the poles. This translates to a prominent

spherical harmonic degree-2, order-0 gravitational component that dominates over all other crustal and gravity fields. In order to examine the true isostatic nature of the crust, this degree-2, order-0 rotational flattening component has to be removed from the code. When this component is removed, the resulting crustal thickness model shows what is similar to the non-isostatic thickness model (Figure 3.1b). Note how the rotational flattening component contributes to not just the equatorial bulge shape of the planet, but also to a much thicker crust at the Tharsis Rise volcanic region. Now that this prominent factor is removed and the crustal thickness model looks like previously published models, I proceed to test out other parameters in the program.

Before I reproduce Neumann et al.'s (2004) model, it is important to note that the topography profile in this study includes this degree-2, order-0 flattening component whereas the models in Neumann et al. (2004) do not. Their study references the topography to an ellipsoid. Several assumptions can be made when working with global gravity data. One can either leave the degree-2 flattening component in and solve for the crustal thickness or they can remove this degree-2 flattening component and leave the residual degree-2 structures in. Neumann et al. (2004) references topography to an ellipsoid which is not affected by the flattening component, whereas the topography in this study is referenced to the geoid that does get affected by the various spherical harmonic degrees, such as the degree-2 flattening component. Thus this work includes this component and this component has to be removed before any crustal thickness analyses can be made. Another issue is that there is a degree-1 component in the topography (the topographic dichotomy), which will generate a degree-1 geoid; however, there is no degree-1 component in the gravity in the crustal thickness model used here, so extra caution is needed when analyzing the resulting crustal thickness models.

3.1.3 Reproducing Neumann et al.'s Model

The first step in my work is to verify that I can reproduce the crustal thickness map from Neumann et al. (2004) shown in Figure 3.2a. Given that Neumann et al. also use the method developed by Wieczorek and Phillips (1998), this test confirms that I am able to correctly use Wieczorek's crustal thickness program. For comparison, my version

of the crustal thickness map of Mars is shown in Figure 3.2b. As mentioned in Chapter 2, the biggest difference between my crustal thickness modeling and Neumann at al.'s is that their study considers a separate lower density value for the polar ice caps and a higher density value for the volcanic regions, in addition to the average crustal and mantle densities. My model incorporates only the crustal and mantle densities, with no other densities used to produce my crustal thickness maps. I use 2900 kg/m^3 for average crustal density, 3500 kg/m^3 for average mantle density, and 5 km for minimum crustal thickness.

Overall, my model has a very similar pattern when compared to Neumann et al. (2004). All other models in this study are generated using a rainbow-like color scale, but for this model, the scale color palette has been adjusted slightly to match that of Neumann et al.'s model to show how the same thickness patterns are exhibited in both models. See Table 3.1 for a comparison of crustal thickness values between my model and that of Neumann et al. The average crustal thickness of the Northern Lowlands is generally about 40 km thinner than the average crustal thickness of the Southern Highlands. The thickest crustal area (Figure 3.2), indicated by red in both models, is located at the Tharsis volcanic region between 60°N and 60°S and 220° and 300°E. Both maps show the point of thickest crust, indicated by small white region with an excess of 80 km, to be located at about 10°S and 240°E, right under the volcano Arsia Mons, the most southwestern volcano in the chain of three Tharsis Montes volcanoes. From this point at the Arsia Mons volcano, there seems to be an apparent tail-like path extending from this volcano toward the southeast at about 45°S and 270°E. I will come back to this specific feature in detail in section 3.5 about a possible mantle plume track. Other thick regions are also shown in both models, such as the northern broad shield volcano Alba Patera, located at 40°N and 250°E.

The thinnest crust, indicated by dark blue/violet in both maps, are located in craters and impact basins including Argyre Basin (50°S and 320°E), Hellas Basin (40°S and 70°E), Borealis Basin (45°N and 80°E to 140°E), with the thinnest point at Isidis Basin (10°N and 90°E), just north of the equator, on the dichotomy boundary. Both models show a steep change in crustal thickness from the Southern Highlands (yellow), transitioning (green) to the Northern Lowlands (light blue), and marking the topographic

and crustal dichotomy of the planet. This transitional boundary of the crust tends to stay within 30° north and south of the equator. What is striking is that this boundary seems to deviate more from the equator, going more north at the Tharsis volcanic region, with the boundary extending up to 50°N, north of and encompassing Alba Patera and surrounding regions. Another interesting feature is a ring-like pattern surrounding the Borealis Basin, between 20°N to 80°N and 60°E to 180°E. This looks like an annulus of remnant material of a crater rim from which the Borealis impact basin was formed. I will also come back to this feature in detail in section 3.6. Here, I've shown that my crustal thickness model fits Neumann et al.'s model well, despite that they used additional densities for the polar ice caps and volcanic regions in their study. Thus, the addition of those densities does not make much of an impact to the overall crustal thickness model and those additional densities will not be used in this study here. In section 3.7, I compare my isostacy model with that of Neumann et al.'s (2004).

Table 3.1 Comparison of Crustal Thicknesses Between Neumann et al.'s Model and Model in this Study

Crustal Thickness (km)	Neumann et al. (2004)	This Study
Minimum Crustal Thickness	5.8	5.0
Maximum Crustal Thickness	102	88.5
Average Crustal Thickness	45	44.9

*thicknesses obtained using the same uniform crustal density of 2900 kg/m^3 and mantle density of 3500 kg/m^3

3.1.4 Assumed Crustal Thickness

Besides using a set uniform density for the crust and mantle in both Neumann et al.'s model and my model, I also use an assumed minimum crustal thickness to "anchor" the model, so that no resulting modeled thickness is negative, or less than zero. Gravity methods alone cannot be used to constrain the crustal thickness, because gravity is non-unique. Hence, an assumed minimum crustal thickness has to be set along with the two

densities to model the resulting thickness. I use a minimum crustal thickness of 5 km in the model, which gives a mean crustal thickness of 44.9 km, consistent with the mean crustal thickness of 45 km from Neumann at al.'s (2004) study. This assumed minimum crustal thickness of 5 km places the minimum crustal thickness of near 5 km at Isidis Basin (10°N and 90°E) and the northern part of the crater floor of Hellas Basin (40°S and 70°E) (Figure 3.2b). Figure 3.3 illustrates that changing the assumed minimum crustal thickness simply shifts the overall crustal thickness in the resulting models without changing the large-scale pattern. The larger the chosen assumed minimum crustal thickness, the larger the overall modeled crustal thickness. With my successful reproduction of Neumann et al.'s model, I proceed to test out various combinations of parameters in Wieczorek's crustal thickness code in order to study possible hidden structures on Mars.

3.2 Density Contrast

As discussed above, the density of the crustal and mantle materials plays the most important role in determining the thickness of the crust and/or the depth to the crust-mantle interface, which gives insights and implications to the structure and thermal history of the planet. Thus, the first experiments are to vary the density values of these materials to study how the crustal thickness changes. First, I vary the crustal density values while holding the mantle density constant at 3500 kg/m^3. Second, I essentially repeat the experiment, but vary the mantle density values while holding the crustal density constant at 2900 kg/m^3. Both of these constant density values are used based on a number of assumptions and various gravity studies as discussed in section 2.3. Lastly, I combine these density relationships in a summary plot to show how various density contrasts across the crust and mantle affect the overall average crustal thickness.

3.2.1 Varying Crustal Density

In the first set of experiments, I vary the crustal density while holding the mantle density constant. As noted earlier in Chapters 1 and 2, the standard Martian mantle

density assumed in a variety of gravity studies is 3500 kg/m^3. This will be the value set for the constant mantle density in this section. The crustal density range I've chosen goes from 2500 kg/m^3 to 3100 kg/m^3 in steps of 100 kg/m^3. Table 3.2 lists the range of crustal density values while the plots in Figure 3.4 show the various crustal thickness models generated using some of these crustal density values. Figure 3.4 shows three models with increasing crustal density. As crustal density increases, or the crust-mantle boundary density contrast decreases, the thickness increases. This is especially more prominent in the Tharsis volcanic region and the Southern Highlands, indicated by yellow and red regions of thicker crust. The thinner crustal regions such as the Northern Lowlands and the impact basins, indicated by blue, increases in thickness by about 10 km with each increase in density step of 200 kg/m^3. The crust of the Northern Lowlands seem to shift to higher thickness values more uniformly than the crust of the Southern Highlands, where the thickest concentration of material is right under the Tharsis region, Alba Patera, and a spot at the South Pole, indicated by white (Figure 3.4c).

The algorithm of Wieczorek and Phillips (1998) iterates so that the gravity misfit between the observed gravity and modeled gravity becomes small (about less than 1 mgal) and the minimum crustal thickness value set by the user is preserved. In this work, the minimum crustal thickness used is 5 km. Thus, the Moho topography changes so that the gravity misfit is minimized. All these models of varying crustal density fit the gravity data equally well.

Table 3.2 Range of Crustal Density Values and Resulting Crustal Thicknesses

Crustal Density, ρ_{crust} (kg/m^3)	**Density Contrast, $\rho_{mantle} - \rho_{crust}$ (kg/m^3)**	**Average Resulting Crustal Thickness (km)***	
		$l = 10$	$l = 50$
2500	1000	23.71	27.87
2600	900	25.73	30.61
2700	800	28.29	34.09
2800	700	31.62	38.65
2900	600	36.15	44.88
3000	500	42.66	53.86
3100	400	52.80	67.93

*while holding mantle density constant at 3500 kg/m^3

3.2.2 Varying Mantle Density

The second set of experiments varies the mantle density while holding the crustal density constant. Again, noted in Chapters 1 and 2, the standard Martian crustal density value used in gravity studies is 2900 kg/m^3. This will be the value set for the constant crustal density in this section. The mantle density range I've chosen goes from 3300 kg/m^3 to 3900 kg/m^3 in steps of 100 kg/m^3. Table 3.3 lists the range of mantle density values while the plots in Figure 3.5 show the various crustal thickness models generated using some of these mantle density values. Similar to Figure 3.4, Figure 3.5 shows three models with increasing mantle density, in steps of 200 kg/m^3. As mantle density increases, or the crust-mantle boundary density contrast increases, the thickness decreases. The overall average crustal thickness seems to decrease by about 5 to 10 km with every decrease in density of 200 kg/m^3. Again, the more prominent feature that changes thickness the most is the Tharsis volcanic region indicated by the red, elongated

feature and the Southern Highlands, indicated by green thinning to light blue. Again, all of these models of varying mantle density also fit the gravity data equally well.

Table 3.3 Range of Mantle Density Values and Resulting Crustal Thicknesses

Mantle Density, ρ_{mantle} (kg/m^3)	**Density Contrast, $\rho_{mantle} - \rho_{crust}$ (kg/m^3)**	**Average Resulting Crustal Thickness (km)***	
		$l = 10$	$l = 50$
3300	400	49.32	69.24
3400	500	41.32	54.38
3500	600	36.15	44.88
3600	700	32.57	38.28
3700	800	30.02	34.71
3800	900	28.05	32.07
3900	1000	26.49	30.11

*while holding crustal density constant at 2900 kg/m^3

3.2.3 Total Density Contrast

Both Tables 3.2 and 3.3 include a column of the density contrast between the given crustal and mantle density values. We can see that it is not the absolute value of the crustal density or the mantle density that determines the average crustal thickness; it is the density contrast across that boundary that essentially affects the overall crustal thickness (listed in the last column). Figure 3.6 shows a summary of this relationship between density contrast and crustal thickness. Both spherical harmonic degree 10 and 50 are used in this plot to show how the spherical harmonic degree also contributes to the thickness. Overall the spherical harmonic degree shows that the higher the degree, the more the crustal thickness shifts to larger values (more details in section 3.3).

We can see that as the crustal density values increase (shown by the red and blue series), while keeping the mantle density constant at 3500 kg/m^3, the overall minimum crustal thickness increases. This is really equivalent to decreasing the density contrast, resulting in an increase in crustal thickness. The concept is the same with varying the mantle density. While keeping the crustal density constant at 2900 kg/m^3, as the mantle density values increase (purple and green series), the density contrast increases, resulting in a decrease in minimum average crustal thickness. These are essentially identical concept exhibited by a mirror image of the crustal series versus the mantle series shown in Figure 3.6. I have included the density contrast values in all the models in Figures 3.4 and 3.5. Give that gravity is non-unique, there is no constraint on the maximum crustal thickness. The depth of the Moho could be moved deeper or shallower and still fit the gravity data. However, it cannot be moved to a shallow depth too much so that the crustal thickness becomes negative, which is unrealistic; thus what this summary plot really shows is the constraint on the minimum average crustal thickness.

When all six models are put together in decreasing density contrasts, the overall thickness increases. Figure 3.7 is another set of models showing the density contrast. However, the scales of these models have been adjusted. These models were generated to show that the same features are present at different thickness scales associated with their respective density contrasts, and that changing the density contrasts earlier in Figures 3.4 and 3.5 does not necessarily enhance or obscure certain crustal thickness features that are always present.

Thus, these density contrast experiment shows that the more Mars is differentiated into two distinct layers of materials, which distinguish a crustal layer from a mantle layer with a large density contrast, the thinner the crust. The less the crustal or lithospheric layer is differentiated or that it is more uniform in density with less density contrast across the layers, the thicker the crust. We will revisit this point in section 3.5 when we discuss about a possible mantle plume track, crustal thickening, and the hypothesized stagnant lid convection under a one-plate planet (Sramek and Zhong, 2010).

3.3 Spherical Harmonic Degree and Crustal Thickness

Briefly shown in Figure 3.6, the changing of the spherical harmonic degree also contributes to changes in the overall crustal thickness. As explained in Chapter 2, spherical harmonic functions are periodic functions that vary with latitudes and longitudes and can give an approximate value for the spatial resolution of a map. Recall that the higher the spherical harmonic degree value is, the smaller wavelength-scale a feature can be resolved, or higher the resolution. For example, Figure 3.8 shows two crustal thickness models generated with the same set of user input parameters except for the parameter of spherical harmonic degree at which the filter is one-half (see section 2.2, Table 2.1). Both the crustal thickness models in Figures 3.8a) degree-10 and 3.8b) degree-50 are modeled with a crustal density of 2900 kg/m^3, a mantle density of 3500 kg/m^3, and an anchoring minimum crustal thickness of 5 km. Clearly the degree-10 model is characterized by the striking dichotomy that divides the planet into two hemispheres, with a few large-scale features present, including the Tharsis volcanic region, Hellas Basin, and the Borealis Basin in the Northern Lowlands. The landscape features seem to blend together and appear smooth throughout the planet. The Northern Lowlands have a thickness of about 20 km and the Southern Highlands have about 50 km in this model.

The degree-50 model shows the smaller wavelength-scale features and the dichotomy appears less sharp than it does in lower degree models. But the overall landscape is rougher, now that the smaller scale structures appear. Structures such as individual volcanoes, small impact basins, crater rims are apparent at this degree. The crustal thickness also shifts to higher values, with the Northern Lowlands having a thickness of about 30 km and the Southern Highlands having about 60 km. The higher degree model does not eliminate the large structures such as the dichotomy, but it does help reveal and bring out the small-scale structures that were overwhelmed by the larger signal of the large-scale structures. Therefore, changing the spherical harmonic degree does not only change the resolution of the structures present in the model, but also the thickness of the crust.

3.4 Higher-Order Terms

Aside from the spherical harmonic degree parameter, all the crustal thickness models are generated from the equation derived in Chapter 2, strictly following equation 2.6, the heart of the code. Equation 2.6 contains higher-order terms that correspond to the higher frequency, small wavelength-scale structures. In order to assess the importance of these small-scale structures, I modify equation 2.6 to remove the higher-order terms, so that I can observe whether higher-order terms contribute significantly to the results. Equation 2.6 with higher-order terms:

$$h_{ilm} = \omega_l \left[\frac{C_{ilm}^{BA} M(2l+1)}{4\pi\Delta\rho D^2} \left(\frac{R}{D}\right)^l - D \sum_{n=2}^{l+3} \frac{{}^n h_{ilm}}{D_n n!} \frac{\prod_{j=1}^{n}(l+4-j)}{(l+3)} \right] \tag{2.6}$$

and without higher-order terms:

$$h_{ilm} = \omega_l \left[\frac{C_{ilm}^{BA} M(2l+1)}{4\pi\Delta\rho D^2} \left(\frac{R}{D}\right)^l \right] \tag{3.1}$$

For degree 10, which corresponds to a much larger wavelength-scale, the model without higher-order terms compared to the original model including the higher-order terms are visually indistinguishable (Figure 3.9a, c). No difference seems to exist in these two models at this degree value. For degree 50, the model without the higher-order terms is slightly different than the original model with the higher-order terms (Figure 3.9b, d), with a small spot of thicker crust (indicated by white) in the Tharsis region. Due to the smaller scale nature of the higher-order term features, a difference plot was necessary in order to bring out these small-scale patterns (Figures 3.9e, f). The difference plot is created by subtracting the crustal thickness model with higher-order terms from the crustal thickness model without the higher-order terms.

Figure 3.9e reveals that there are differences between the two degree 10 models. However, note that the scale of these thickness variations is between -0.9 and 0.9 km in thickness. What is interesting is the pattern exhibited by this difference plot. There is an apparent, prominent degree-2 structure here, dominating the planet around the equatorial

region, (indicated by green and light blue, about -0.3 to 0 km thickness) with slightly thicker crust at both poles. Besides this large-scale structure, the North Pole exhibits thicker crust of 0.6 km and the Tharsis volcanic construct is even more prominent, thicker than the surrounding plains north and south of it with a thickness above 0.9 km. The rest of the planet's thickness contributed by the higher-order terms seems to hover between -0.3 and 0.2 km. The larger patterns such as the impact basins and Tharsis region were present before in the models with higher-order terms, but the most striking factor here is that the crustal dichotomy is not present, replaced by the degree-2 feature, making this difference plot indispensible and urging for further studies.

Similar to the degree 10 difference plot, a difference plot was also generated for degree 50 to clarify the pattern of small-scale structures (Figure 3.9f). The pattern of these structures does not seem to deviate too much from what is already present, again, what is important is that the crustal dichotomy is not present. The higher-order term features here include the individual Tharsis Rise volcanoes, Olympus Mons, the southwestern rim of Hellas Basin, and some thicker crustal anomalies at both poles and along the equator on the eastern half of the planet, all exhibiting crustal thicknesses of 0.5 km or higher. Not unlike the difference plot for degree 10, Figure 3.9e, this plot shows a general thickening of the crust at Tharsis Rise and the poles while the rest of the planet is at a uniform thickness of about 0 km. Only this plot reveals the detail of smaller-scale structures (indicated by red and yellow spots at about 0.5 to 0.9 km) compared with the obscured, elongated section (green in Figure 3.9e) along the equator. The importance of studying the crustal thickness contribution from the higher-order terms may help us understand how this amount of crustal material is distributed and whether it was generated by small-scale processes such as local lithospheric flexures or large-scale processes such as mantle plumes and their implications for the internal and thermal evolution of the planet. The lack of the degree-1 crustal dichotomy structure at these scales indicate that the global phenomenon is truly a large-scale structure and is not visible at small scales, that it is not contributed by higher-order, small-scale processes.

3.5 Mantle Plume Track

3.5.1 The Hypothesized Track

In previous sections, the models all show a thick tail-like feature that extends from the Tharsis region to the southeast toward the South Pole. This feature may be a possible mantle plume track, a hypothesis suggested in the studies by Sramek and Zhong (2010) and Sramek and Zhong (2012). In various models of crustal thickness I have presented thus far, most of them exhibit this feature when certain criteria is changed, such as varying the density contrast and the spherical harmonic degree. Figures 3.3b, 3.4c, 3.5a, and all the models in Figure 3.7 show a track of excess thickness.

It is not surprising that a possible mantle plume could have existed underneath the Tharsis volcanic region, where the accumulation of volcanic and crustal material built up to become this large construct. What is interesting is that this feature seems to be elongated, stretched out into a much longer feature and not concentrated at one spot. The tail-like pattern suggests that this mantle plume could have been migrating from one point to another, thus creating a mantle plume track. Not unlike the migrating hotspots that created the chain of Hawaiian Islands on Earth, this hypothesized mantle plume could have erupted from under certain locations of the crust where that part of the crust is thinner. Where there are areas of crust that is much thicker, the mantle plume may find it difficult to erupt through larger amounts of material. Instead, the upwelling magma may concentrate under those parts, contributing to the accumulation of material, further thickening the crust in those areas. Thus where the magma is able to erupt through, we see the surface expression of volcanoes.

The three Tharsis Montes volcanoes: Arsia Mons, Pavonis Mons, and Ascraeus Mons (Figure 1.2) are very convincing shield volcanoes that may support this migrating plume theory. These volcanoes line up in an almost perfect straight line with about equal spacing between each volcano that reminds us of the episodically-spaced volcanoes created by hotspots on Earth. However, on Earth, we have plate tectonics that allow the hotspots to "move" and erupt from one place to the next. It is really the crust that is moving above over a more stationary hotspot. For Mars, there are no plate tectonics for such events to occur. So how could there be a mantle plume that migrates? Zhong (2009) and Sramek and Zhong (2010) propose that Mars as a one-plate planet could have

rotated its entire one plate lithosphere due to polar wander (Figure 1.6). Thus if a mantle plume is situated at one spot (Figure 1.5), at the South Pole for example, it can erupt through the crust at different locations if the crust is rotating above this plume spot. Such is what is observed here in the thickness models. Although the line of Tharsis Rise volcanoes do not necessarily line up with the proposed plume track (indicated by black curved arrow in Figure 3. 10), the plume or the one plate lithosphere may have changed direction at the turning point of the location of Arsia Mons, the southwestern most of the three volcanoes.

A recent study by Hynek el al. (2011) reports geological evidence that supports this mantle plume track theory. Their work demonstrates that a specific certain type of plains in the Southern Highlands may be flood basalt plains that were formed from volcanic extrusions. They suggest that the orientation of these surface plains aligns with the proposed mantle plume track from the South Pole to the Thaumasia region, just south of the Tharsis Montes volcanoes (Figure 1.2). Further, Hynek el al. (2011) indicate that this type of plains is not found anywhere else in the southern hemisphere. In addition the areas where these plains are located have a much lower crater density and lacks any remnant magnetization, suggesting that volcanism has occurred in the region to resurface the area, covering or eliminating ancient crater impacts and melting any minerals that could have left residual magnetization in the crustal rocks.

3.5.2 Supporting Evidence of the Track

I have generated and produced various crustal thickness models in this study. All the crustal thickness models show a feature that further supports this mantle plume track theory. Figure 3.10 shows the possible direction of migration of the mantle plume track, shown by the black arrow, starting at the thick region of the South Pole, moving northwest toward Thaumasia, where the thickest region resides (indicated by red), and then shifting its motion, moving further north but changing direction near the location of Arsia Mons toward the northeast instead, and stopping at the volcano Alba Patera. This volcano may or may not be the product of this plume track, but it is in the vicinity of that region. The crustal thickness seems to disconnect (have thinner crust) at points along this

track, making them resemble a chain of separated islands on Earth, which further supports the plume track theory.

In addition to crustal thickness models, gravity misfit maps are generated and they also exhibit an unusual pattern in the same geographic location (Figures 3.11) with a higher concentration of varying gravity misfits. Recall that gravity misfits are the difference between calculated and modeled gravity, which is dependent on density of the underlying material. This elongated pattern (indicated by the black outline in Figure 3.11) of clustered, varying gravity misfits may suggest the varying local density anomalies in the region. Density anomalies could result from magma material melting the crust above, and/or underplating from molten material with the plume. Thus these anomalies may further support the mantle plume track theory.

3.6 Borealis Basin Impact

3.6.1The Impact Theory

In section 1.3 I discussed that the Northern Lowlands may have been formed due to a giant impact crashing onto the northern hemisphere and excavating enough material to create a huge hemispheric basin called the Borealis Basin. It is also proposed that this is how the crustal and topographic dichotomy was formed (Wilhelms and Squyres, 1984). Besides supporting the theory on the mantle plume track, the crustal thickness model and gravity misfit results from this study also reveal features that may support this impact theory and help constrain the impact location site within Borealis Basin.

In most of the crustal thickness models presented in this Chapter, the thinner region (blue) in the northeast part of the map, directly north of the Isidis Basin is the region called Utopia Planitia (Figure 1.2). Further northeast of this thin region located at about 70°N and 200°E, directly north of Arcadia Planitia is the proposed location of the hypothesized impact site (Andrews-Hanna et al., 2008; Marinova et al., 2008; Nimmo et al., 2008). I compare my crustal thickness model with that of Marinova et al.'s (2008) by setting the orientation to be the same as their crustal thickness model, Figure 3.12. My model shows very similar crustal thickness patterns compared to Marinova et al.'s model.

In Figure 3.12, the thicker regions of the Tharsis Rise in the east (in this orientation) and the regions north of Hellas Basin in the west seem like two constraining regions of much thicker materials reaching north and partially encompassing a circular-shaped region, part of the Borealis Basin. If this thicker material extended up to the North Pole, it may as well form a circular ring of materials that could make up a giant crater rim. This is essentially what it may be. I compare the gravity misfit maps in the same orientation (Figure 3.13) with my crustal thickness model (Figure 3.12 bottom). At first, it does not seem apparent in Figure 3.13a that there is a ring-like structure. However, after I generated the same misfit maps with the higher order terms taken out (Figures 3.13 b and c), it becomes more apparent that the gravity misfit or density anomalies show up as a partial ring of materials (indicated by black oval in Figure 3.13c) with more variations in the misfits on the southern "rim" of the circular feature, suggesting there may be materials of different densities that make up this part of the ring. Different density materials could come from denser, mantle material that gets excavated and displaced onto the surface, mixed with lower density crustal material. The northern "rim" of this anomalous ring may be the lack of density anomalies. If this was truly an impact crater rim, then the material here in the northern rim could have been resurfaced, either by impact melting or other volcanism or mechanism that obliterated the presence of materials with density differences. Those processes could have homogenized the composition of the crust in that region.

3.6.2 Is it an Impact Crater or Not?

Further more, gravity misfit maps can help decipher whether this feature is an impact crater or not. The dark blue region that is Utopia Planitia in my crustal thickness model in Figure 3.12 exhibits the characteristics of an impact crater. But is it a younger crater superimposed onto the "Borealis Basin" crater that I have discussed above or is it an entirely different type of crustal feature? Note the gravity misfit signature of Hellas Basin and Isidis Basin in Figure 3.13 b and c. Those basins sporting crater rim materials are characterized by low, negative misfit values on the rim (blue and purple) whereas their basin floors or region within their rim are characterized by high, positive misfit

values (red and white). It is accepted that these two basins are impact craters, so when comparing the impact site circled in black (Figure 3.13c) to these basins, we find that the possible "rim" of materials have low, negative misfit values and the inner basin floor materials have near 0 mgal misfit values along with various scattered anomalies of high, positive misfit values. Overall this ring-like feature share very similar characteristics with classic impact craters; the only difference is that the material inside the rim does not have a uniform positive misfit of other crater basin floors (the red and white of the crater floors of Hellas and Isidis basins).

Figure 3.14 is an orthographic projection of the same gravity misfit map of Figure 3.13b. This is just to show that the misfits still created a ring-like structure in spherical perspective and that it is not an optical illusion or data artifacts from the Hammer projection (Figure 3.13). There are some factors that could potentially explain why this circle of materials does not behave the same as a classic impact crater. Let's treat this feature as a crater; the basin floor is not uniform in the same misfit value throughout, but speckled with mainly positive misfits (about 15-30 mgal), the material present here may vary in composition and widely distributed within the crater. Underlying these speckled, higher positive misfit features, the basin floor seems more uniform (green) at about zero misfit. What we might be seeing is the signature of a remnant crater rim that has been subsequently covered and resurfaced by new material. This new material could be due to wide-spread flood basaltic volcanism that infilled the basin floor and smoothed out the density anomalies that were there before. We can see the crustal thickness expression of this in the crustal thickness map in Figure 3.12 (bottom), where the light blue area in that region is thicker than the dark blue Utopia Planitia west of it. The fact that this region is thicker than Utopia Planitia indicates that the crater at Utopia Planitia occurred after the emplacement of the flood basaltic plains. This is just one hypothesis I have for that region based on my observations of the thickness and misfit maps. If this circled region is indeed the location of a giant impact basin for the most of the northern hemisphere, then the sheer size of the basin would suggest and imply certain crustal rebound conditions pre- and post-impact, which leads us to discuss about isostacy.

3.7 Isostatic Compensation

3.7.1 Degree-1 and Degree-2 Crustal Structures

Figure 3.1b shows that the isostatic crustal thickness model (generated at degree-50) resembles the regular, non-isostatic model generated with the Mars Crustal Thickness code (also generated at degree-50, Figure 3.8b); it is important to note that the pattern is similar, but the thickness scale is different. Since the rotational flattening factor had a large power over small-scale crustal and gravity fields, I examine the degree-1 and degree-2 crustal structures separately to see which one contributes more to the overall global isostacy. In doing this, I generate a non-isostatic crustal thickness model from the Mars Crustal Thickness code and generate an isostatic crustal thickness model from the MarsIsostacy code, using the same mean crustal thickness in both, so that I can compare the two. In the Mars Crustal Thickness code, the mean crustal thickness is generated from the iteration I discussed earlier, whereas the mean crustal thickness in MarsIsostacy is the minimum thickness I input when running the program. For both programs to have the same mean crustal thickness, I first run the Mars Crustal Thickness code to obtain its calculated mean crustal thickness, then I input this value into the MarsIsostacy code as its minimum thickness. Both models now have the same mean crustal thickness value. An example of this is shown in Figure 3.15 with a mean crustal thickness value of 20.55 km for degree-1 and Figure 3.16 with a mean crustal thickness value of 27.15 km for degree-2.

Degree-1 structure corresponds to running the programs and setting the maximum degree to compute the Moho to, lmax = 1, and degree-2 corresponds to lmax = 2. After running both programs and generating both non-isostatic and isostatic crustal thickness models at such long wavelength-scales, it was not immediately apparent what regions are isostatic, thus a difference plot was needed. I subtract the non-isostatic crustal thickness model grid file from that of the isostatic model to obtain the difference plot, which brings out the finer differences between the two (similar to Figure 3.17c, generated with degree-50). If the difference plot shows features that are near 0 km, then that means those regions have no difference between non-isostatic and isostatic, therefore those regions are deemed isostatic. For lmax = 1, Figure 3.15c shows the difference between the non-

isostatic model and the isostatic model only differs by plus or minus 0.3 km with thicker crust in the northern hemisphere and thinner crust in the southern hemisphere. This is quite close to being 0 km, thus at this degree-1 wavelength-scale, Mars is more or less isostatic, with only minor global-scale variations that could be the result of the difference between the center-of-mass and center-of-figure or a large-scale internal process such as a degree-1 mantle plume located in one hemsiphere. I note here that Neumann et al. (2004) discussed how their model exhibited an approximately 3 km offset between the center-of-mass and center-of-figure that is contributed by this degree-1, order-0 component (see Table 4.1 for the degree-1, order-0 coefficient for Mars). Their value is about 2 times the -1735.55 m coefficient, thus making it about -3471 m (or -3.5 km). We can see here that the offset in this model is less than that value.

For lmax = 2, Figure 3.16c shows the difference between the non-isostatic model and the isostatic model to range from -10 km to 5 km. These thickness values are more significant and deviates a lot more from 0 km, suggesting that at the degree-2 wavelength-scale, Mars is not globally isostatic, but only in the regions that is close to 0 km (green regions). Other than the more significant thickness values, the pattern exhibited by this difference plot resembles a bull's eye or an impact crater-shaped feature. When lined up with a MOLA topographic map (Figure 2.8) showing surface features, this bull's eye is located at the equator where Valles Marineris transitions from the Southern Highlands to the Northern Lowlands, centered on where there is an absence of the prominent dichotomy boundary (near Chryse Planitia, 30°N, 40°W, Figure 1.2). This is the location where the dichotomy boundary has a more transitional nature than the sharper, more abrupt boundary elsewhere on the planet (see Figure 2.8). It looks like a crater in the difference plot pattern (also see Figure 3.17c) because the center of the feature has very thin crust (purple and black) surrounded by a rim of thicker crust (orange and red). If this is really an impact crater, then the observation of the northern rim having even thicker crust (indicated by white) may suggest that the impact hit the planet at a slightly oblique angle coming from the south.

3.7.2 Implications, Thermal History, & Density Constraints

I discussed about the possible Borealis Basin impact in the Utopia Planitia region in the Northern Lowlands in section 3.6, which may be one hypothesis that can explain the crustal dichotomy between the northern and southern hemisphere. In addition to that impact theory, if this bull's eye pattern seen here in the degree-2 difference plot is also an impact crater (Figure 3.17c), then this may be related to the formation of the Tharsis Rise volcanic region and maybe the Elysium Mons volcano on the antipodal side of Tharsis Rise (25°N, 145°E, Figure 1.2).

Based on this bull's eye pattern and corresponding MOLA surface topography, I propose a hypothesis that it is this global-scale impact that impacted the planet and triggered multiple eruptions that helped create the Tharsis Rise volcanic region (western rim of the red, thicker-crust ring). The thicker crust in the northern rim of this ring of material (indicated by the white crescent) may be supporting evidence of global-scale eruptions or mantle overturn that resulted in massive lava flows on the surface. This event may be the reason why most of the northern hemisphere is resurfaced, creating the smooth, Northern Lowlands we see today. Also, while this impactor is hitting the planet at this location, the antipodal point of this impact (left and right edge of Figure 3.17c, purple and black) is also being compressed while the northern and southern regions are being stretched and extended. This compression on either side of the equatorial region may be the precursor to elastic lithospheric rebound that may later become isostatic (those regions are not isostatic shown in this plot). Since crustal and mantle materials are being mixed at the impact location and redistributed to the northern and southern regions, then molten materials with different densities could trigger the formation of a mantle plume near the South Pole, given that the density and viscosity changes go deep enough to the core-mantle boundary for a mantle plume to form. Instead of forming a degree-1 mantle plume, the North Pole area may experience more massive mantle overturn and crust-mantle homogenization that eliminates the formation of mantle plumes.

My hypothesis seems to fit well with the surface expression of the topography shown on the MOLA maps and is further supported by the pattern exhibited in the geoid map in Figure 2.6. Although the study conducted by Phillips et al. (2001) suggests that the formation of the Tharsis Rise region and the antipode is due to elastic stresses, my hypothesis here is an alternative suggestion to these formations. Coming back to the

question whether Mars is isostatic or not: these difference plots clearly show a significant difference in predicted crustal thickness at the degree-2 wavelength-scale. The biggest difference is the Tharsis Rise volcanic region, which is not surprising given the large topographic load situated on top of the crust in that region. The difference between the two crustal thickness models extends to the eastern rim of thicker-crustal material; the co-location of Hellas Basin and Isidis Basin along that eastern rim may be much younger features that have elastic support. Those impact basins were formed subsequent to this hypothesized event, thus erasing parts of the thicker crust on this eastern rim of materials.

The planetary community more or less agrees that Mars has become mostly isostatic except for volcanic regions and impact basins. However, my findings from the degree-2 difference plot above suggests that Mars is still far from being mostly isostatic and that it is still in the process of reshaping itself through crustal rebound and material redistribution. If this is the case, then the planet may still retain a significant amount of heat in the interior, implying that the thermal processes on Mars have yet to cease, and that the planet may still be active. The idea of modeling with only two densities to represent the crust and the mantle is very simplified. Although this method is accepted and adopted by most of the planetary community, more density values should be acquired (preferably from sample-return missions as opposed to inference from meteorites) and used to constrain these crustal thickness models, which will help piece together a better and more thorough geodynamic history of the planet.

Figure 3.1

a. With the degree-2, order-0 Rotational Flattening Component

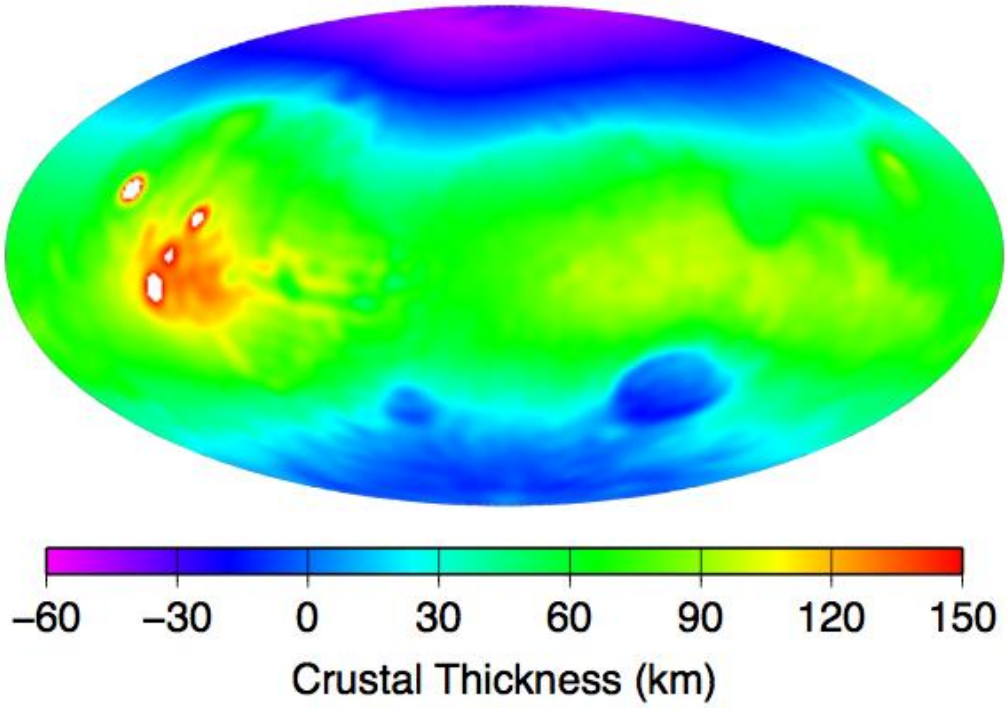

b. Without the degree-2, order-0 Rotational Flattening Component

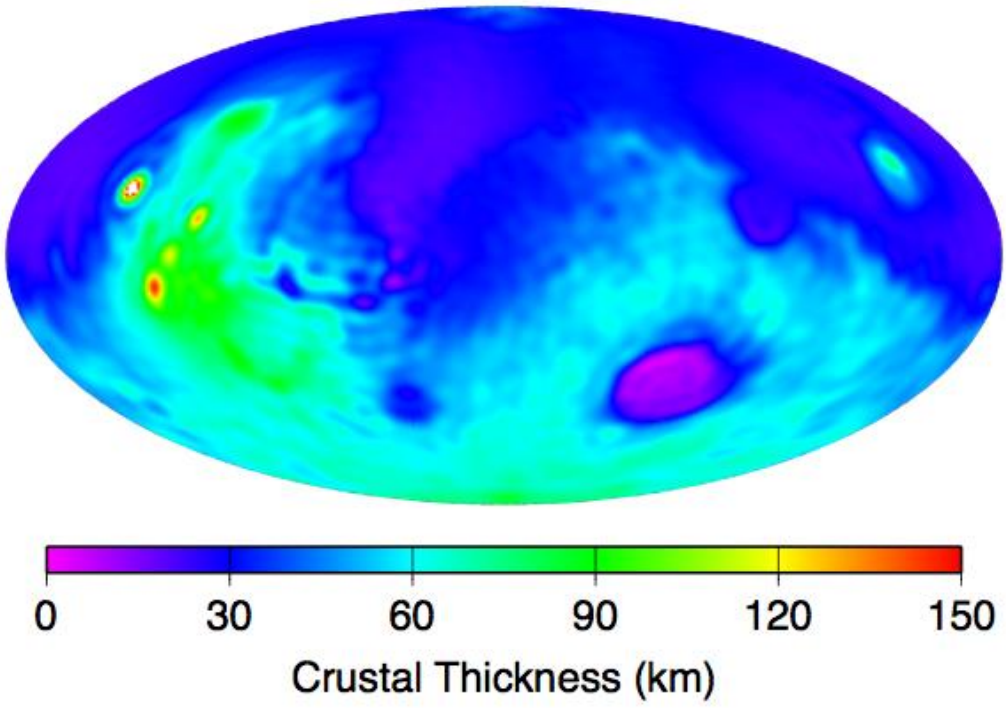

Figure 3.1 (con't.)

Airy-isostatic crustal thickness models showing how the rotational flattening component contributes a large degree-2, order-0 structure to the overall crustal thickness, dominating other existing structures (**a.**). The familiar crustal dichotomy shows up after this rotational flattening component is removed from the program (**b.**). Note that the rotational flattening component contributes to the shift in global crustal thickness. These models were generated using an average crustal density of 2900 kg/m^3, an average mantle density of 3500 kg/m^3, and an assumed minimum crustal thickness of 5 km.

Figure 3.2

a.

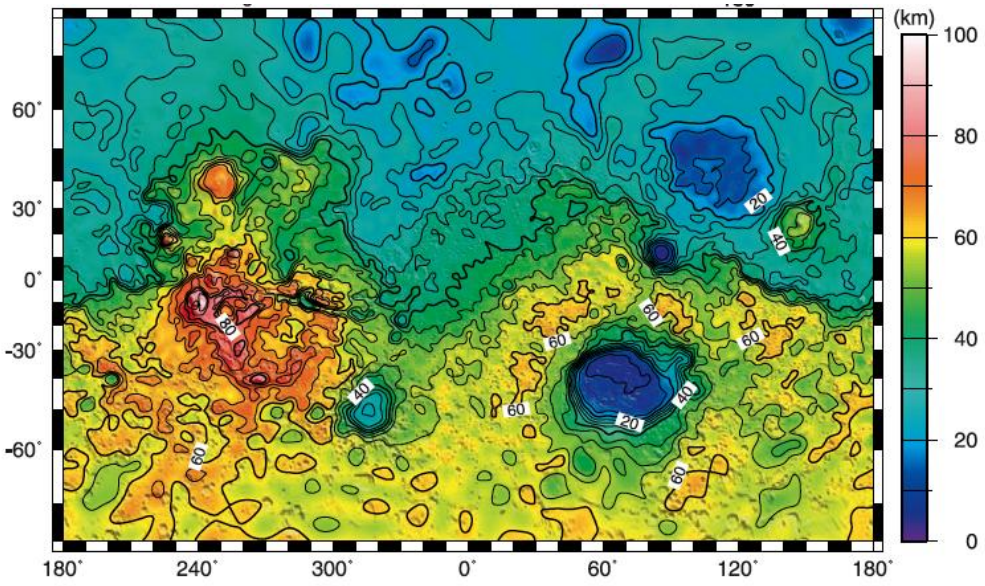
(km)
100
80
60
40
20
0
60˚
30˚
0˚
-30˚
-60˚
180˚
240˚
300˚
0˚
60˚
120˚
180˚

b.

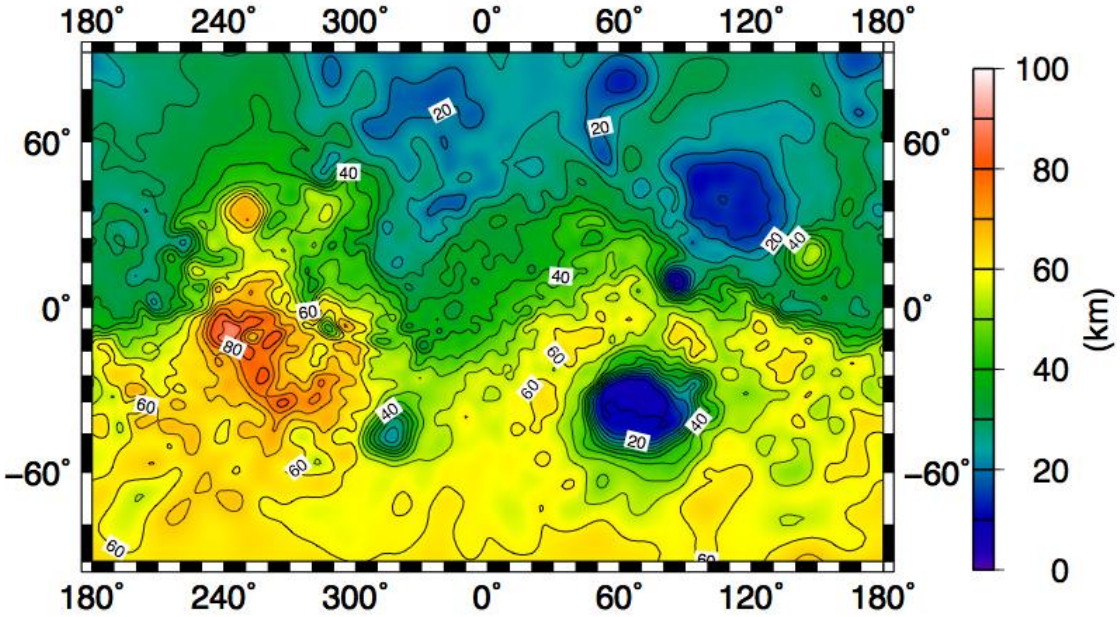
180˚
240˚
300˚
0˚
60˚
120˚
180˚
60˚
0˚
−60˚
100
80
60
40
20
0
(km)

Figure 3.2 (con't.)

Comparison of the crustal thickness models: **a.)** Neumann et al. (2004)'s version and **b.)** my version in this study. Neumann et al.'s version also includes a shaded relief topography superimposed on their map whereas my model does not. These models were generated using an average crustal density of 2900 kg/m^3, an average mantle density of 3500 kg/m^3, and an assumed minimum crustal thickness of 5 km.

Figure 3.3

a. Assumed minimum crustal thickness of 5 km

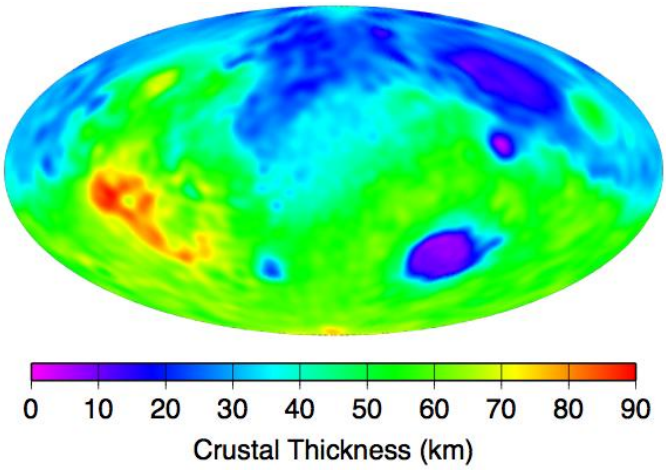

b. Assumed minimum crustal thickness of 15 km

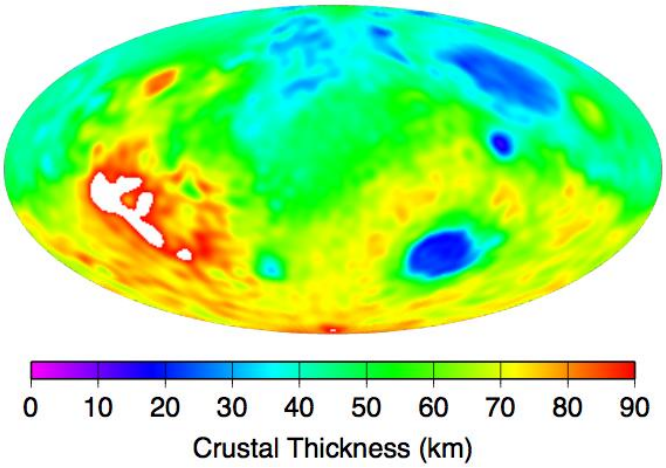

c. Assumed minimum crustal thickness of 30 km

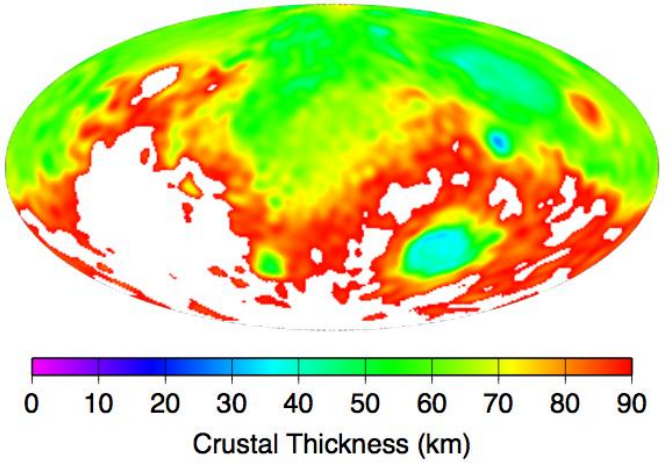

Figure 3.3 (con't.)

Crustal thickness maps showing how varying the assumed minimum crustal thickness shifts the overall global crustal thickness. The higher the assumed crustal thickness chosen, the larger the overall crustal thickness. These models were generated using an average crustal density of 2900 kg/m^3, an average mantle density of 3500 kg/m^3, and the assumed minimum crustal thicknesses stated.

Figure 3.4

a. Crustal Density: 2600 kg/m^3, a density contrast of 900 kg/m^3

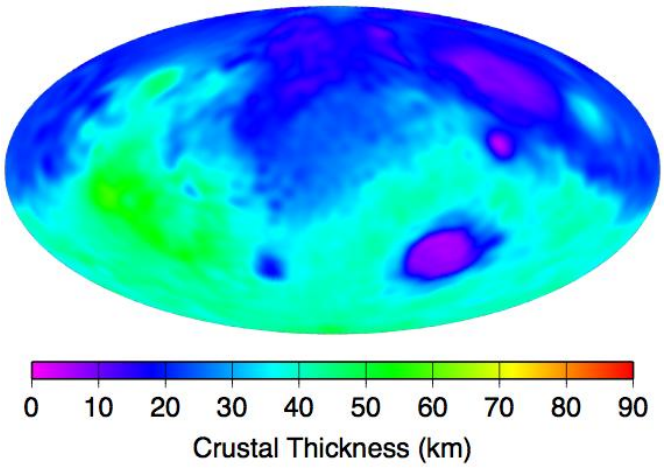

b. Crustal Density: 2800 kg/m^3, a density contrast of 700 kg/m^3

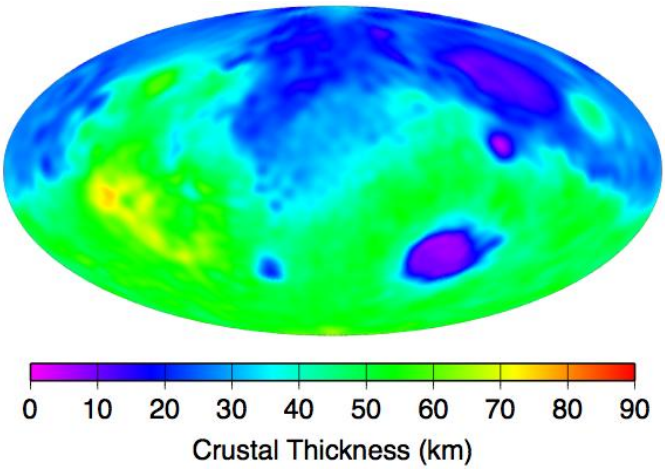

c. Crustal Density: 3000 kg/m^3, a density contrast of 500 kg/m^3

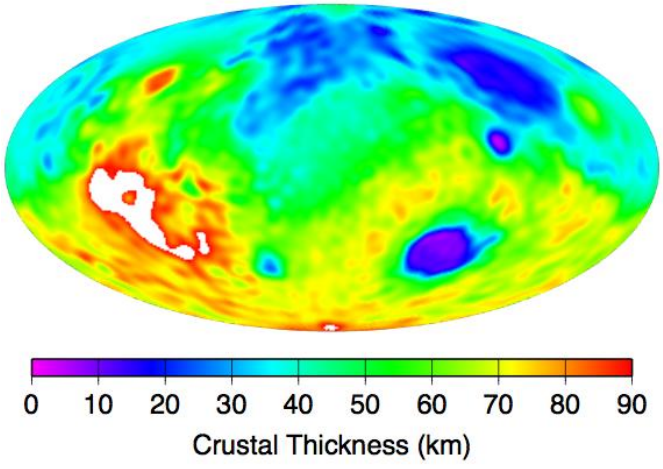

Figure 3.4 (con't.)

Crustal thickness maps showing how varying the crustal density while holding mantle density constant at 3500 kg/m^3 affects the overall thickness. As crustal density increases, or the crust-mantle boundary density contrast decreases, the thickness increases. This is especially more prominent in the Tharsis volcanic region and the Southern Highlands, indicated by yellow and red regions of thicker crust. These models were generated using an assumed minimum crustal thickness of 5 km at spherical harmonic degree 50.

Figure 3.5

a. Mantle Density: 3500 kg/m^3, a density contrast of 600 kg/m^3

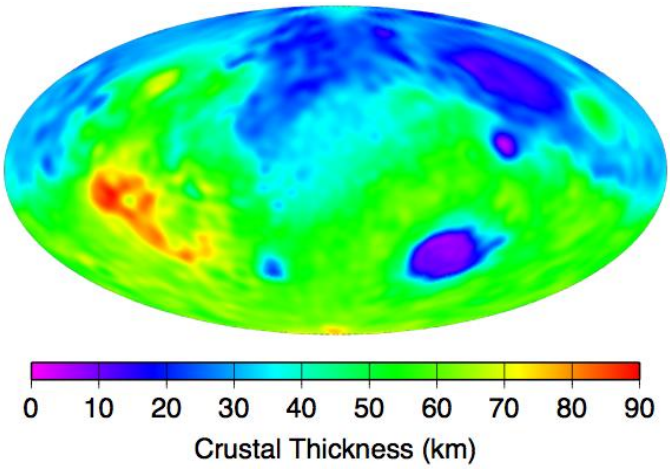

b. Mantle Density: 3700 kg/m^3, a density contrast of 800 kg/m^3

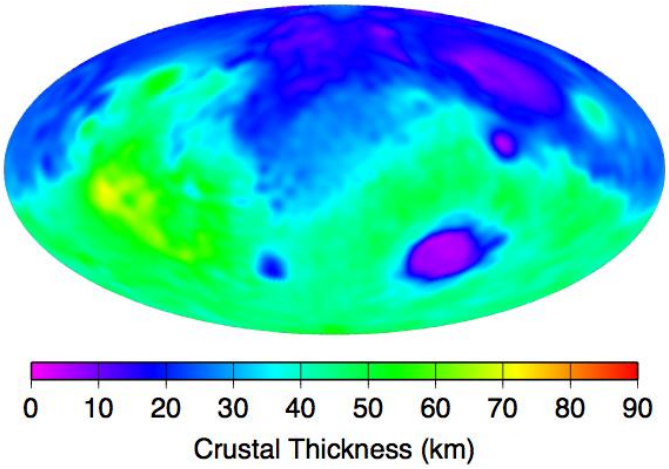

c. Mantle Density: 3900 kg/m^3, a density contrast of 1000 kg/m^3

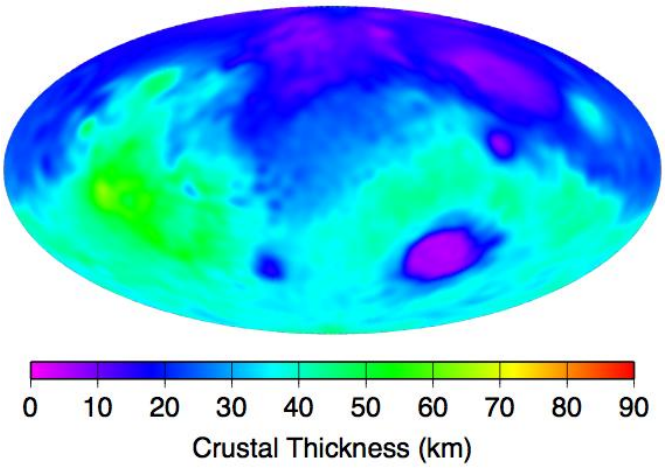

Figure 3.5 (con't.)

Crustal thickness maps showing how varying the mantle density while holding crustal density constant at 2900 kg/m^3 affects the overall thickness. As mantle density increases, or the crust-mantle boundary density contrast increases, the thickness decreases. This is again more prominent in the Tharsis volcanic region indicated by the red, elongated region and the Southern Highlands, indicated by green thinning to light blue. These models were generated using an assumed minimum crustal thickness of 5 km at spherical harmonic degree 50.

Figure 3.6

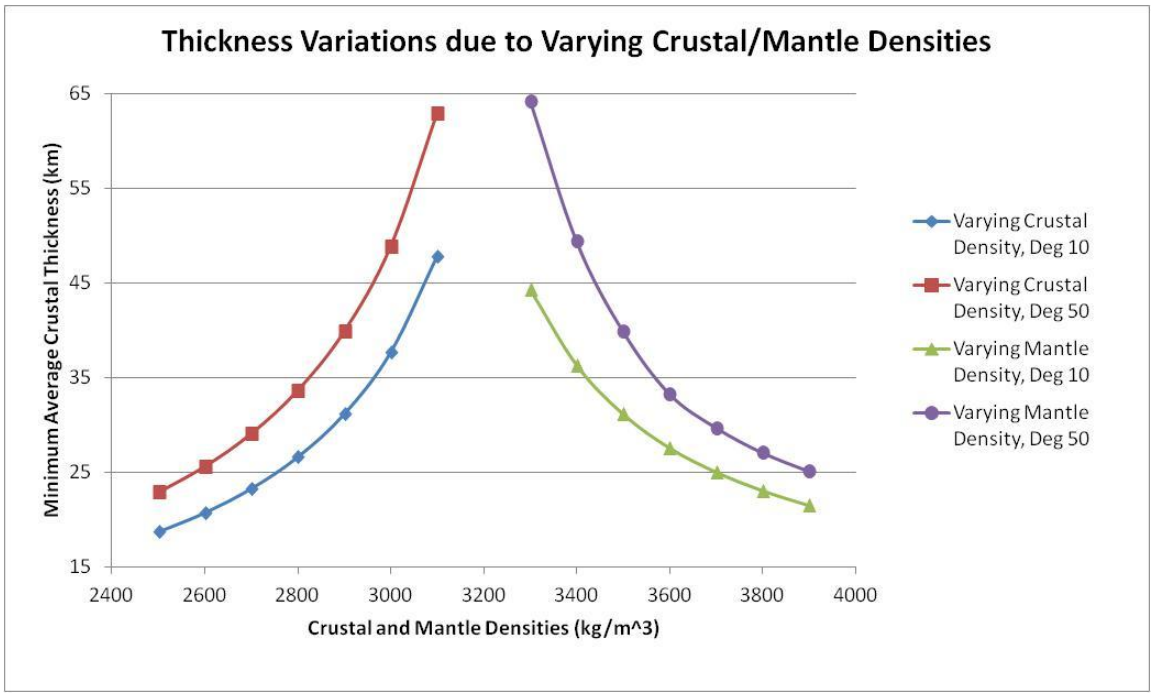

Plot showing the relationship between density contrast across the crust-mantle boundary and its effect on the resulting average crustal thickness. The blue and red series show varying crustal density while holding mantle density constant, in spherical harmonic degrees 10 and 50, respectively. The green and purple series show varying mantle density while holding crustal density constant, in spherical harmonic degrees 10 and 50, respectively. It is visible that the red series showing increasing crustal density (decreasing density contrast) is a mirror image of the purple series showing increasing mantle density (increasing density contrast). The difference between the spherical harmonic degree 10 series and degree 50 series is that the higher the spherical harmonic degree, the higher the crustal thickness values are shifted. These models were generated using a variety of crustal and mantle density combinations and an assumed minimum crustal thickness of 5 km.

Figure 3.7

a. Density contrast of 1000 kg/m^3

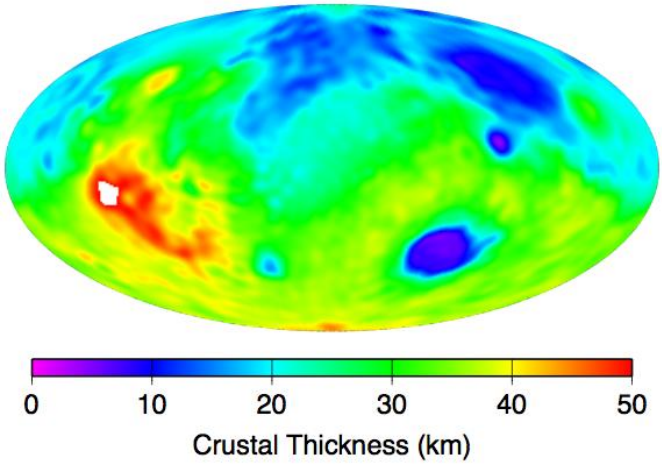

b. Density contrast of 700 kg/m^3

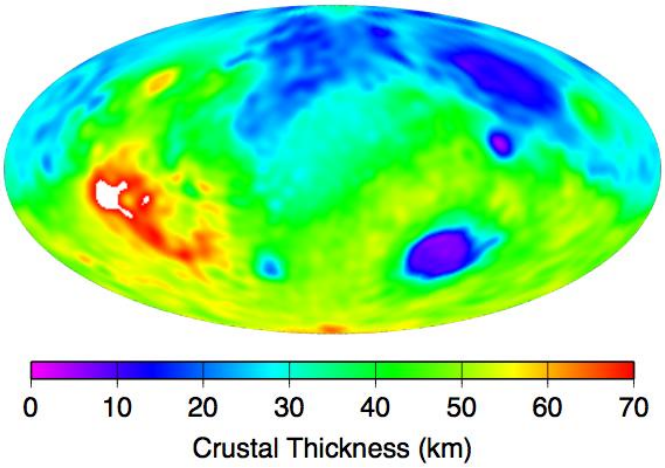

c. Density contrast of 500 kg/m^3

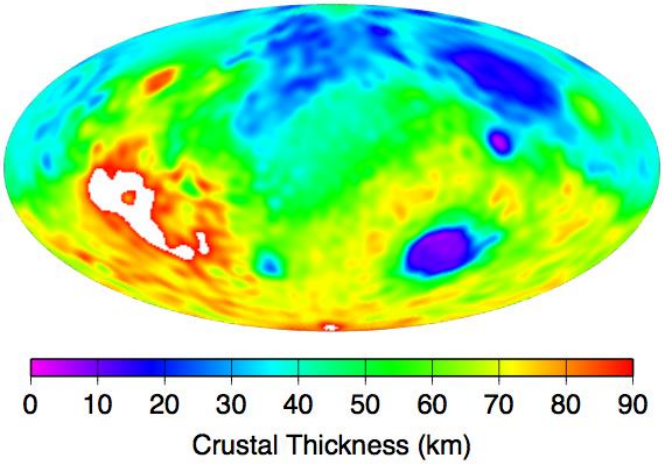

Figure 3.7 (con't.)

Crustal thickness maps showing how the density contrast changes overall crustal thickness. Note the scales of these models have been adjusted and are not at the same scale. This is to show that the same features are present at different thickness scales associated with their respective density contrasts, and that changing the density contrasts does not necessarily enhance or obscure certain crustal thickness features that are always present. These models were generated using an assumed minimum crustal thickness of 5 km at spherical harmonic degree 50.

Figure 3.8

a. Degree 10

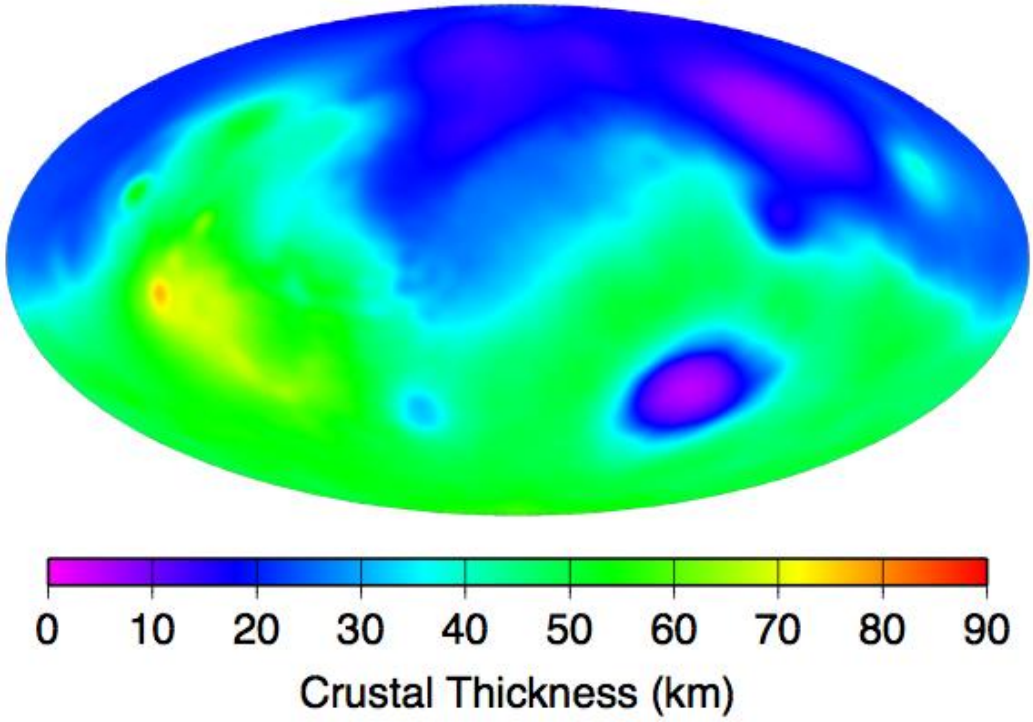

b. Degree 50

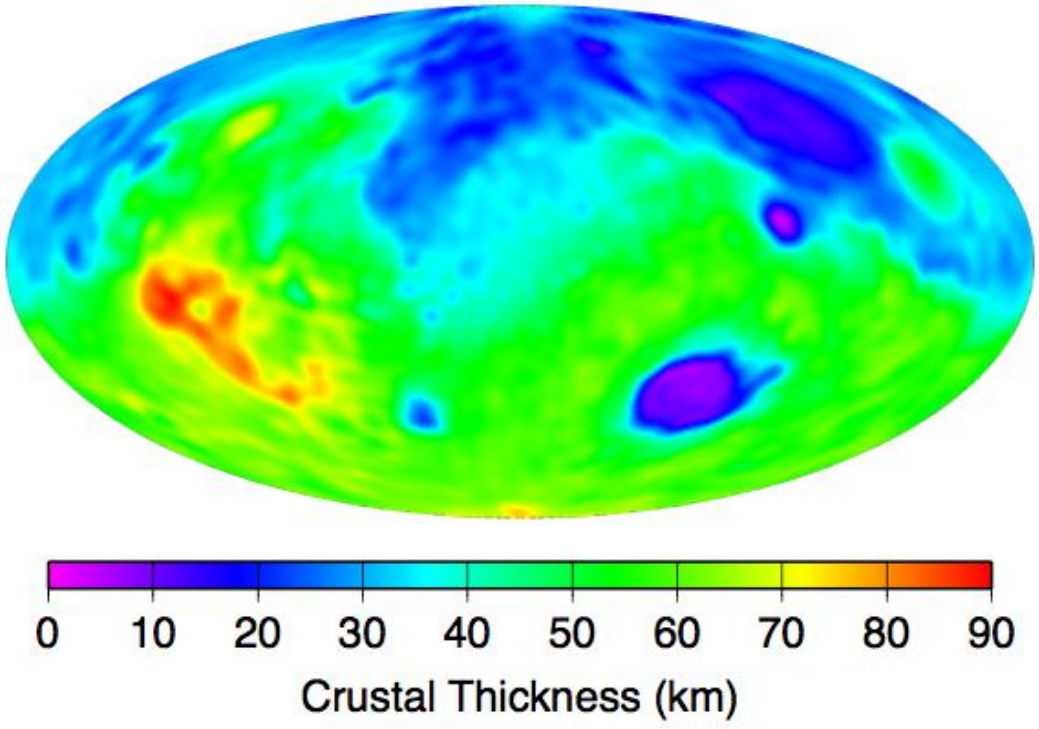

Figure 3.8 (con't.)

The spherical harmonic degree function does not only characterize the spatial resolution of a map, but it also contributes to the thickness changes at different degrees for a crustal thickness model. Here degree-10 shows the most prominent large-scale features on Mars whereas degree-50 exhibits the finer-scale detailed crustal features. Also, the overall crust of the model has shifted to larger thickness. These models were generated using an average crustal density of 2900 kg/m^3, an average mantle density of 3500 kg/m^3, and an assumed minimum crustal thickness of 5 km.

Figure 3.9

a. Degree 10, with higher terms

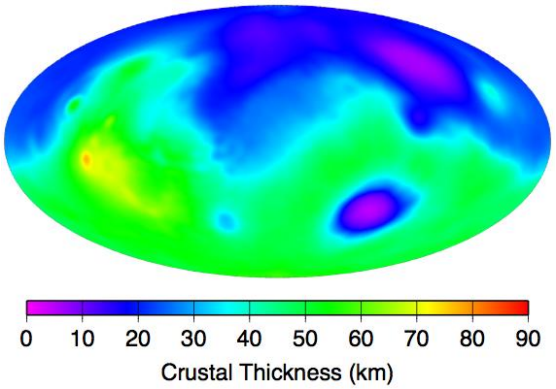

b. Degree 50, with higher terms

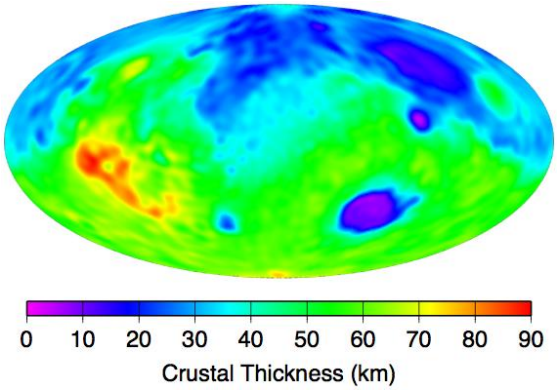

c. Degree 10, without higher terms

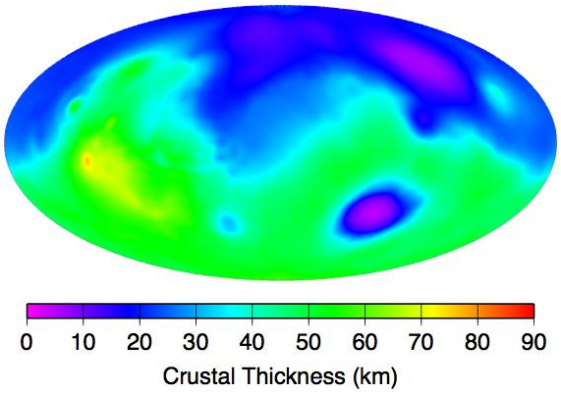

d. Degree 50, without higher terms

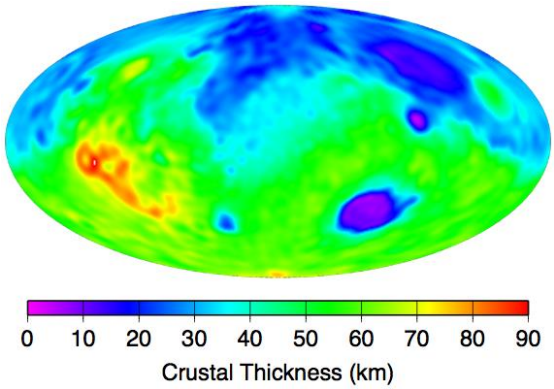

e. Degree 10, difference plot

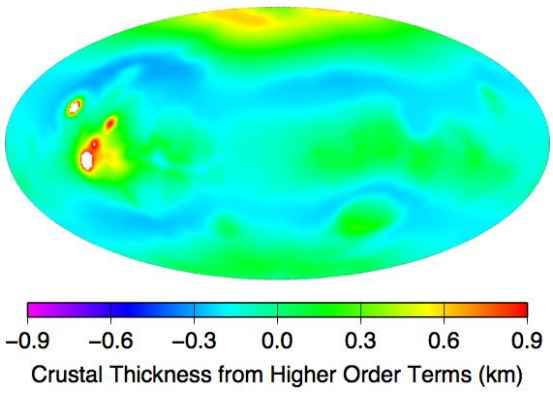

f. Degree 50, difference plot

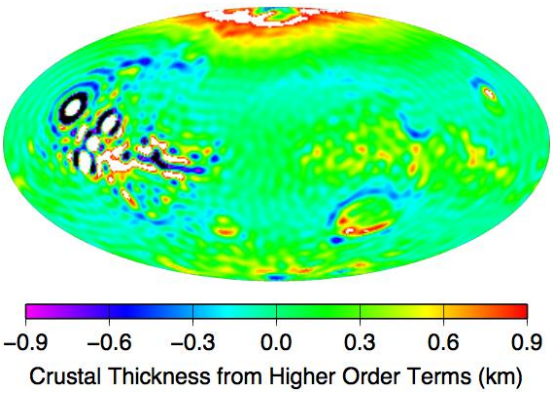

Figure 3.9 (con't.)

Small-scale structures contributed by higher-order terms may not be visible on a large-scale. When a difference map is created to plot the difference between the model with higher-order terms and the model without the higher-order terms, it becomes more apparent where those small-scale structures are located. Note the very small scales of these higher-order term features in e.) where a long-wavelength structure is apparent and f.) where the difference in thickness is largely due to small-wavelength scale structures such as the Tharsis region and some crater rims of the impact basins. These models were generated using an average crustal density of 2900 kg/m^3, an average mantle density of 3500 kg/m^3, and an assumed minimum crustal thickness of 5 km.

Figure 3.10

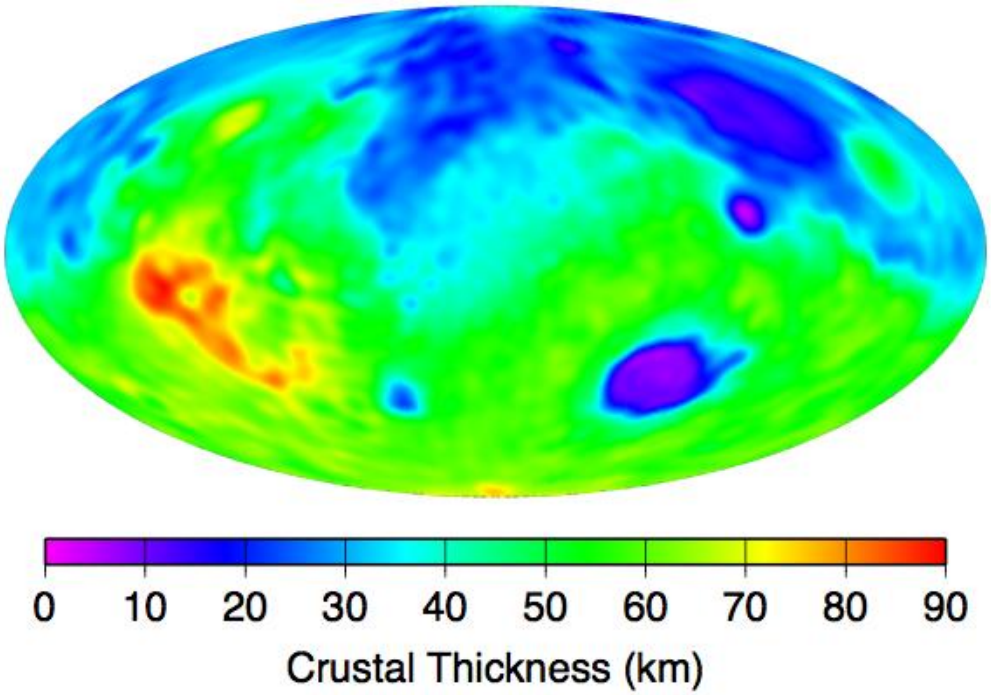
0 10 20 30 40 50 60 70 80 90
Crustal Thickness (km)

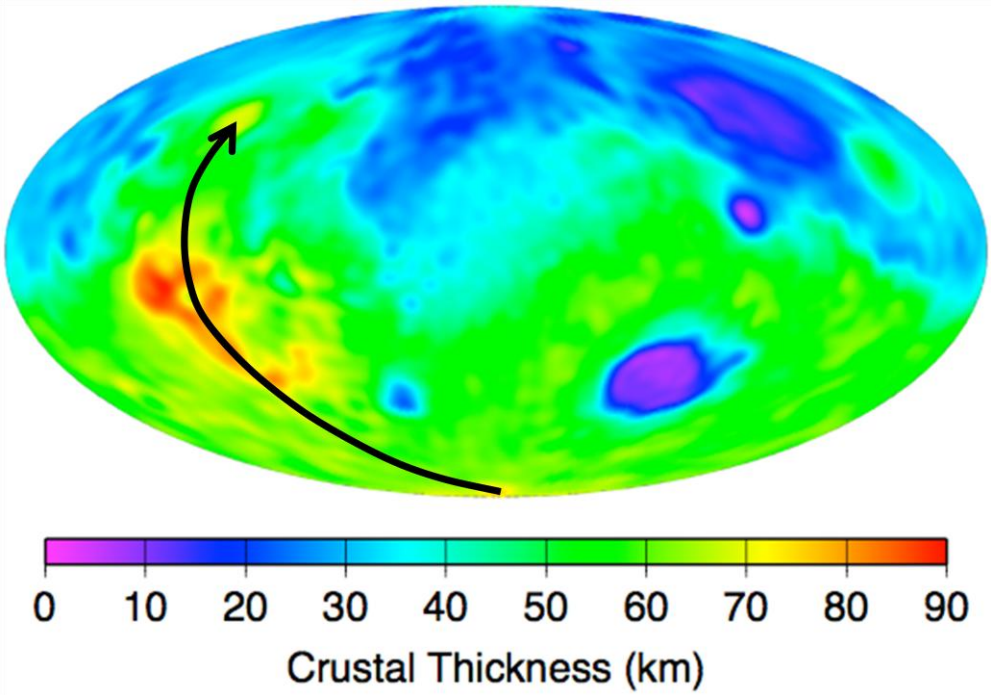
0 10 20 30 40 50 60 70 80 90
Crustal Thickness (km)

Figure 3.10 (con't.)

Crustal thickness map with arrow showing where the proposed mantle plume track is situated, migrating from the South Pole to its current location under the Tharsis region near the crustal dichotomy. This model was generated using an average crustal density of 2900 kg/m^3, an average mantle density of 3500 kg/m^3, and an assumed minimum crustal thickness of 5 km at spherical harmonic degree 50.

Figure 3.11

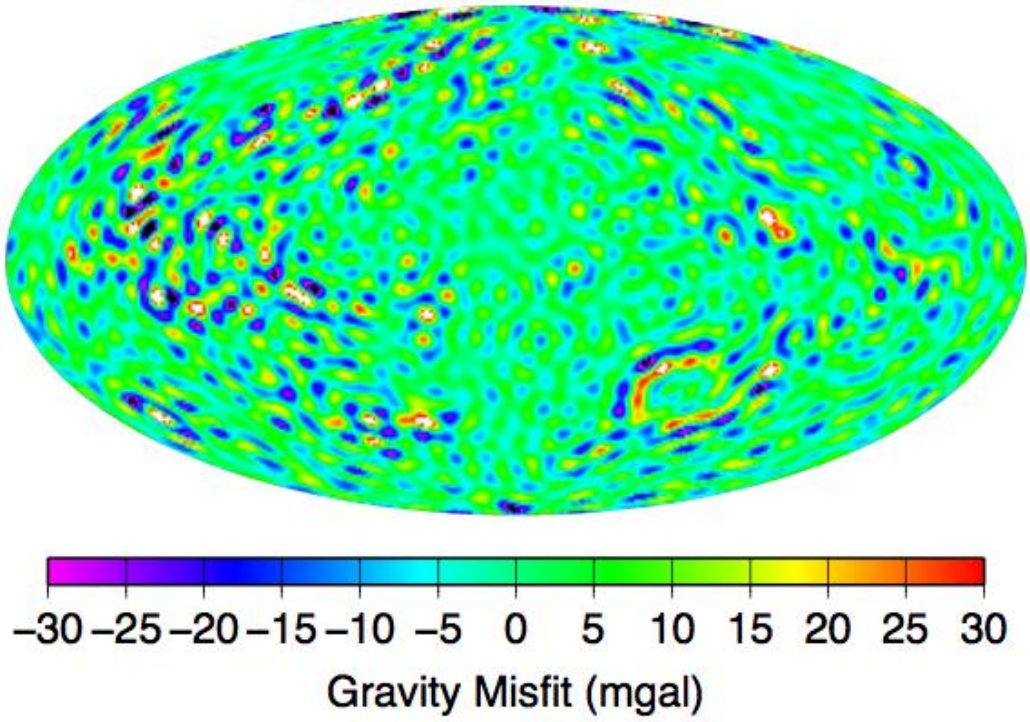
–30 –25 –20 –15 –10 –5 0 5 10 15 20 25 30
Gravity Misfit (mgal)

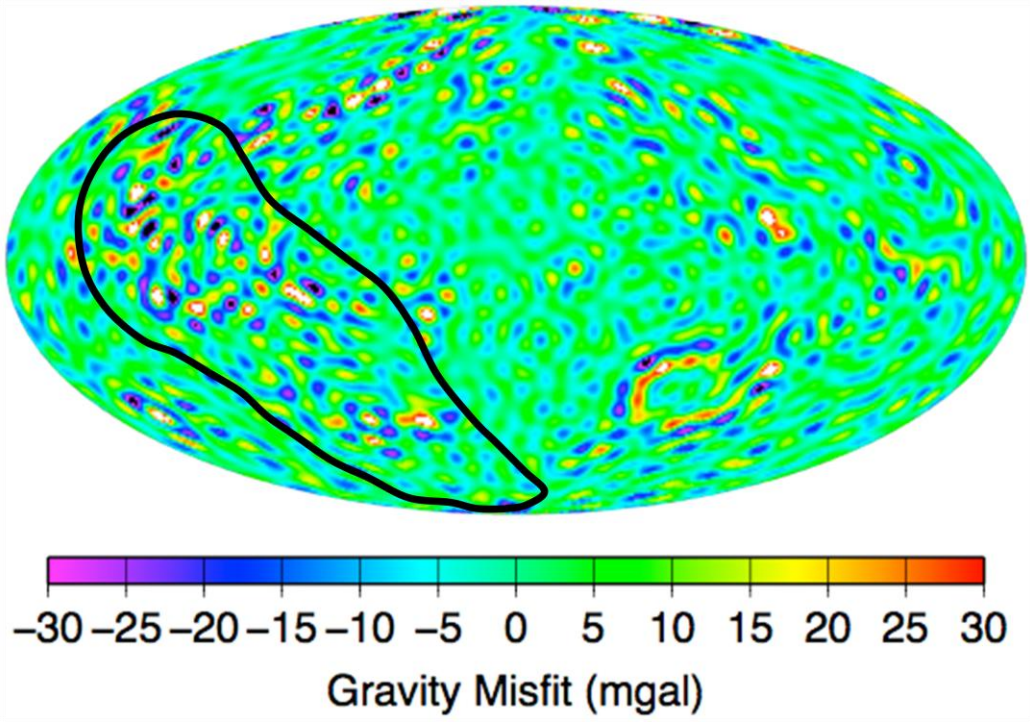
–30 –25 –20 –15 –10 –5 0 5 10 15 20 25 30
Gravity Misfit (mgal)

Figure 3.11 (con't.)

Gravity misfit map showing the more clustered variations in misfits (outlined in black) around the Tharsis region and southeast of that area toward the South Pole, indicating varying density anomalies in the vicinity of the proposed mantle plume track. This model was generated using an average crustal density of 2900 kg/m^3, an average mantle density of 3500 kg/m^3, and an assumed minimum crustal thickness of 5 km at spherical harmonic degree 50.

Figure 3.12

Marinova et al., 2008

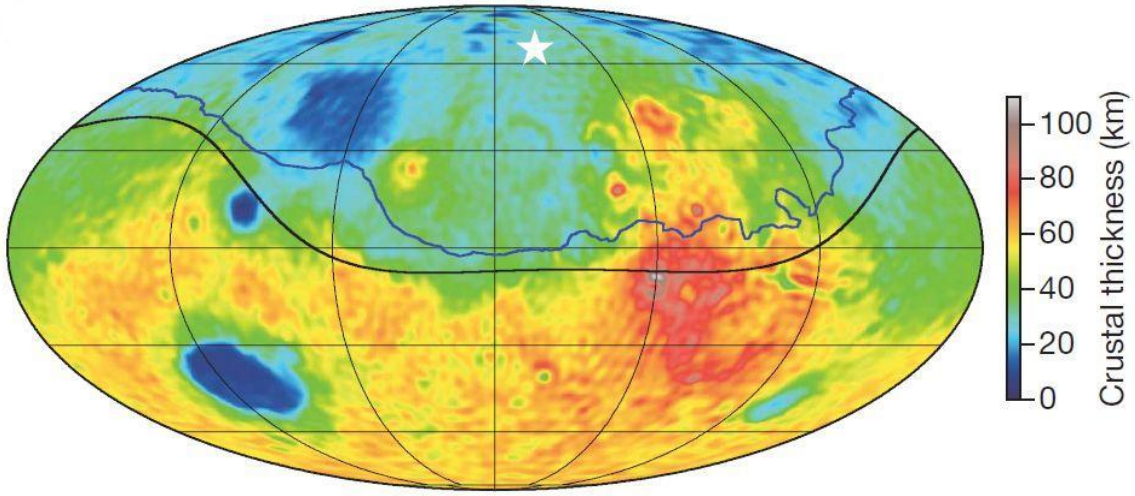

This study:

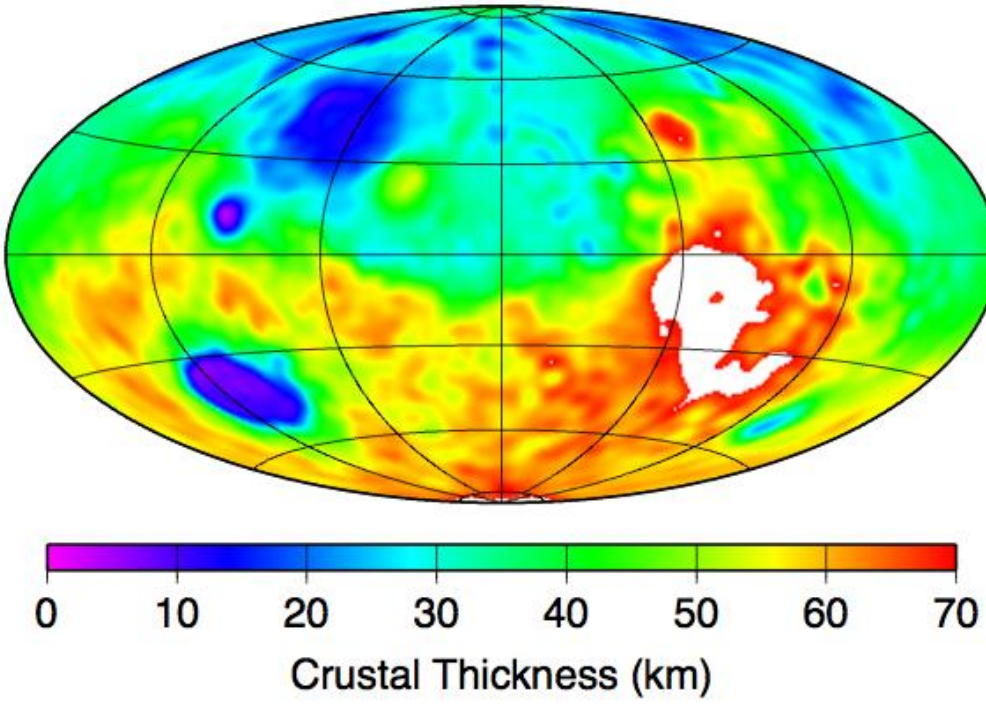

Figure 3.12 (con't.)

Top image: Crustal thickness map by Marinova et al., 2008, showing the dichotomy outline and the point of impact, indicated by the star. Bottom image: model in this study generated using an average crustal density of 2900 kg/m^3, an average mantle density of 3500 kg/m^3, and an assumed minimum crustal thickness of 5 km; it is oriented geographically the same as Marinova et al.'s thickness map for comparison, centered at 206°E. The scale for the crustal thickness from this study has been truncated to 70 km here to show the similarities between the model from this study and that of Marinova et al.'s. Thicknesses greater than 70 km are shown in white, located at the Tharsis Rise region.

Figure 3.13

a. Misfit generated with higher order terms

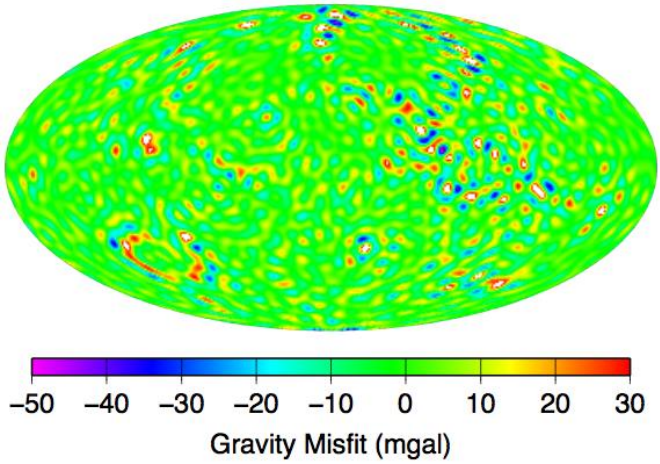

b. Misfit generated without higher order terms

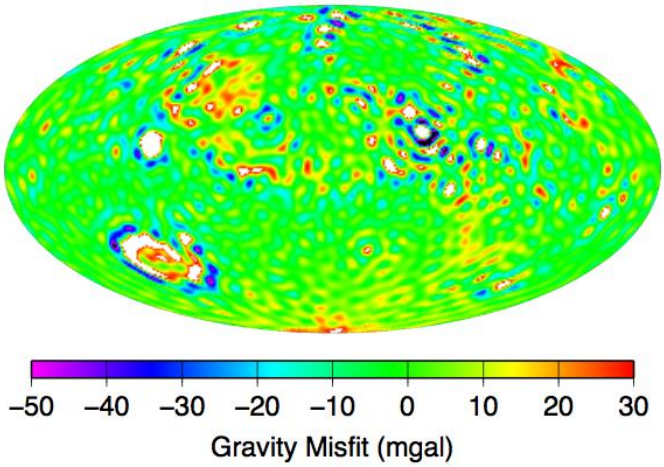

c. Misfit generated without higher order terms, with impact feature circled

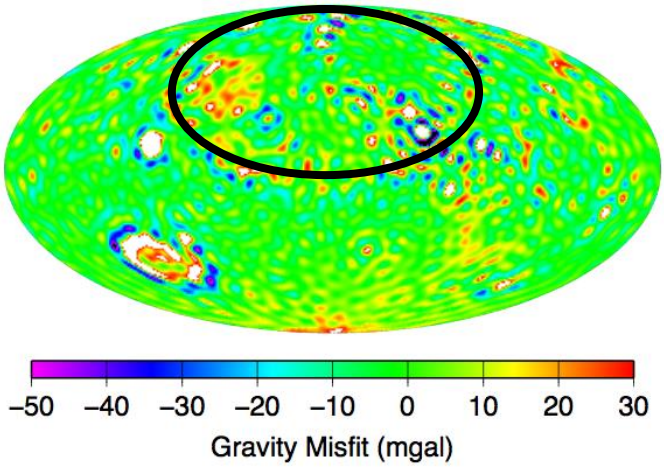

Figure 3.13 (con't.)

Gravity misfit maps compared to the thickness models. It is also in the same orientation as the maps by Marinova et al., 2008 (see Figure 3.12 above), centered at 206°E. Figure 3.13a is the misfit generated with the higher order terms. Figure 3.13 b and c is the same misfit generated without the higher order terms. As shown in 3.13c, the black circle shows a ring-like structure that may be related to the proposed region of impact if a giant object had impacted the Northern Lowlands and helped create the crustal dichotomy. This also shows that the higher order terms had to be removed to show this hidden feature. These models were generated using an average crustal density of 2900 kg/m^3, an average mantle density of 3500 kg/m^3, and an assumed minimum crustal thickness of 5 km at spherical harmonic degree 50.

Figure 3.14

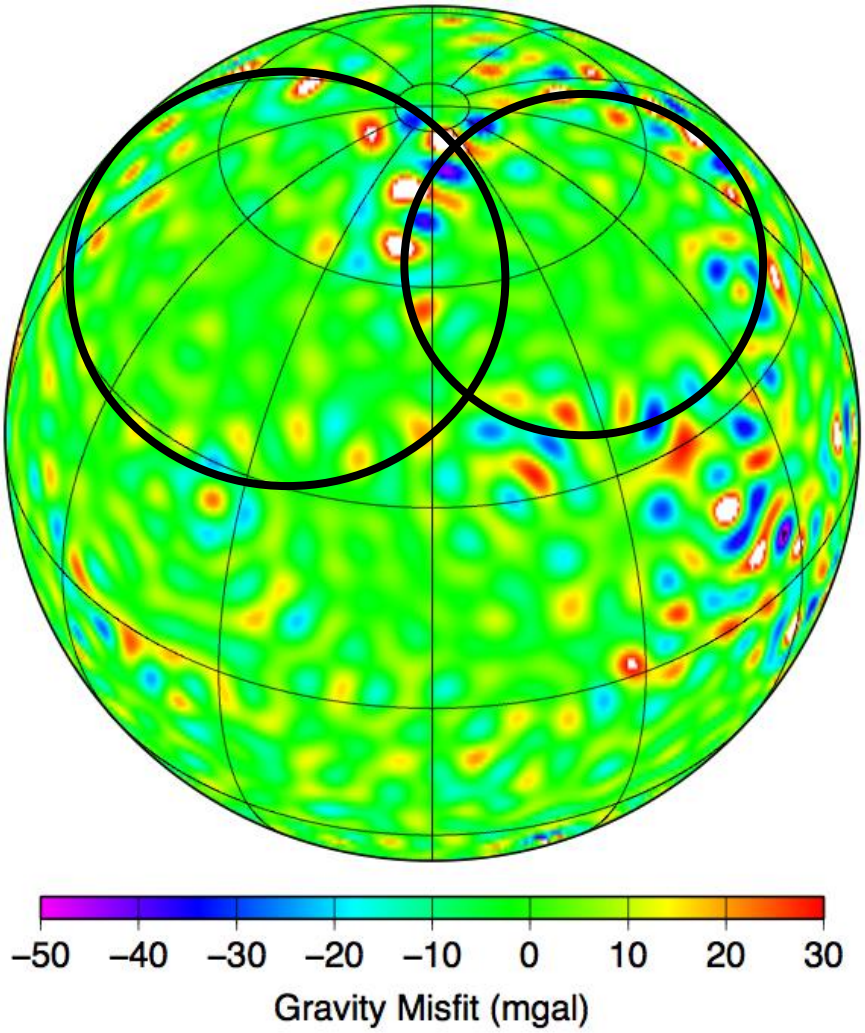

An orthographic projection of the same gravity misfit map of Figure 3.13a, here centered at 30°N and 200°E. This is just to show that the misfits still created a ring-like structure in spherical perspective and that it is not an optical illusion or data artifacts from the Hammer projection (Figure 3.13). This model was generated using an average crustal density of 2900 kg/m^3, an average mantle density of 3500 kg/m^3, and an assumed minimum crustal thickness of 5 km at spherical harmonic degree 50.

Figure 3.15

a. Non-isostatic thickness generated at lmax = 1

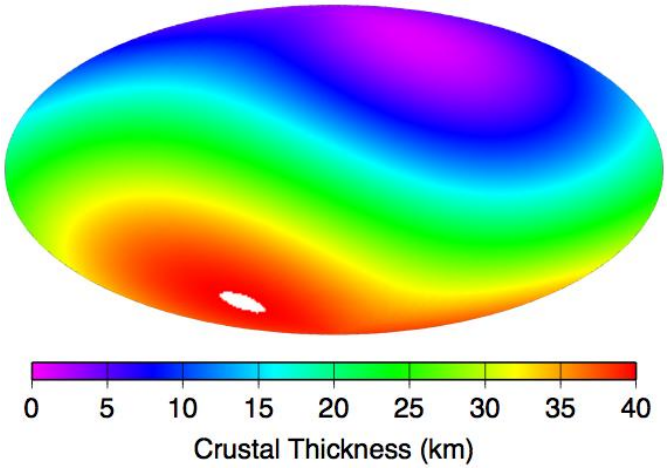

b. Isostatic thickness generated at lmax = 1

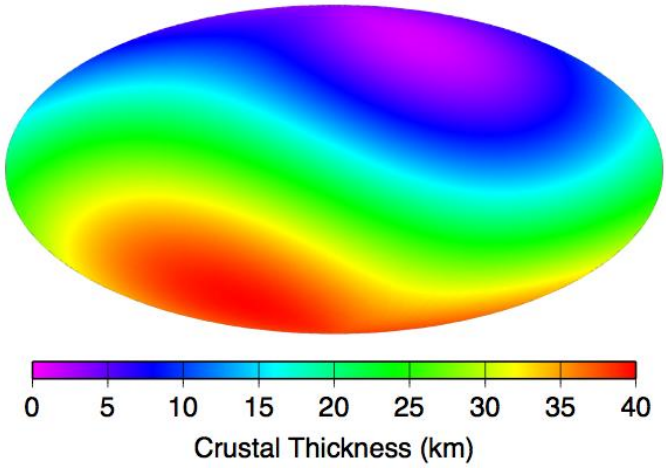

c. Difference between non-isostatic and isostatic thickness

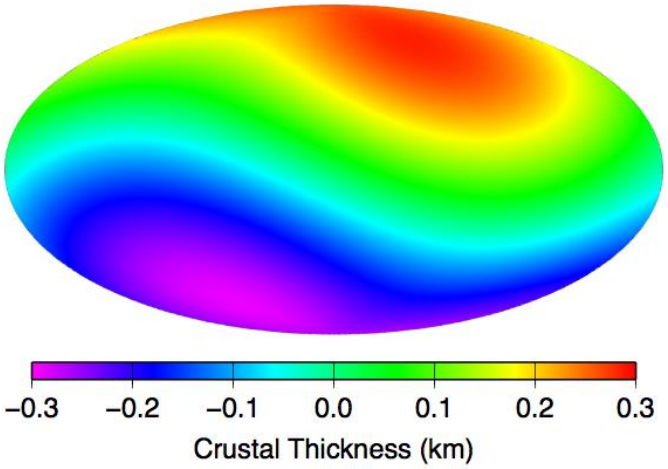

Figure 3.15 (con't.)

Crustal thickness models generated at lmax = 1. The top image **a.)** is the non-isostatic crustal thickness model generated from the Mars Crustal Thickness code, while the middle image **b.)** is the Airy-isostatic crustal thickness model generated from the MarsIsostacy code. Both models have a mean crustal thickness of 20.55 km, as shown in the equatorial region. The bottom image **c.)** is the difference between the two to show what regions are near 0 km, which indicates isostatic crust. Note the scale here is within -0.3 km and 0.3 km, showing very little deviance from 0 km, thus the degree-1 structure is more or less globally isostatic. (Please refer to section 3.7.1 for more detail). These models were generated using an average crustal density of 2900 kg/m^3 and an average mantle density of 3500 kg/m^3.

Figure 3.16

a. Non-isostatic thickness generated at lmax = 2

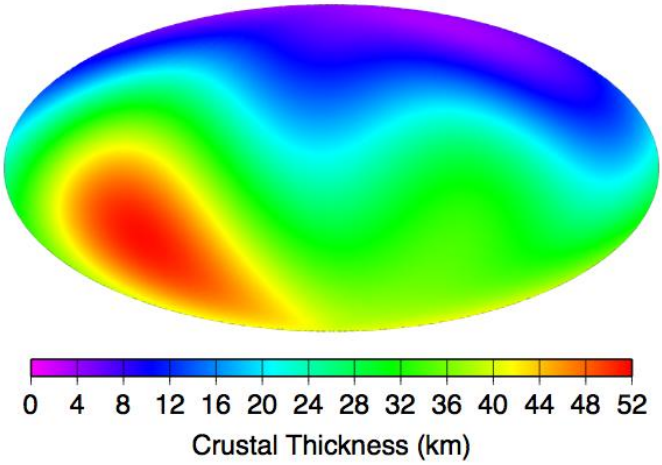

b. Isostatic thickness generated at lmax = 2

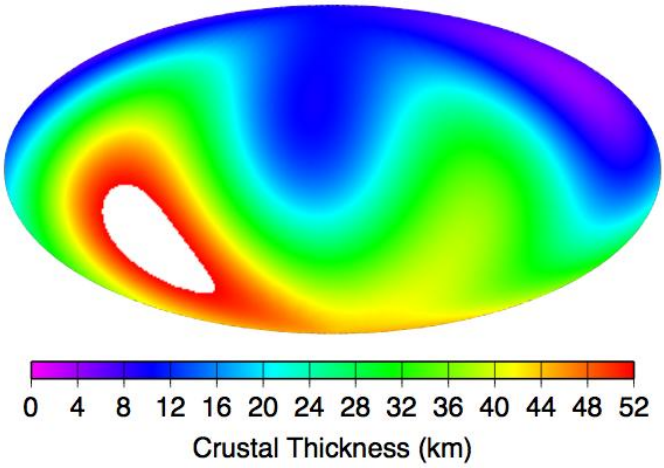

c. Difference between non-isostatic and isostatic thickness

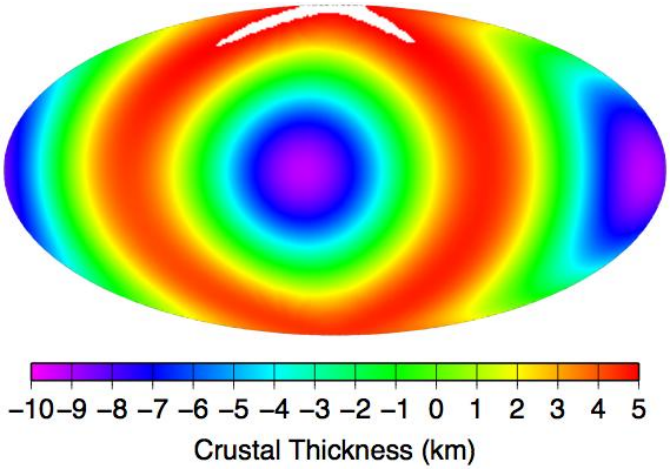

Figure 3.16 (con't.)

Crustal thickness models generated at lmax = 2. The top image **a.)** is the non-isostatic crustal thickness model generated from the Mars Crustal Thickness code, while the middle image **b.)** is the Airy-isostatic crustal thickness model generated from the MarsIsostacy code. Both models have a mean crustal thickness of 27.15 km, as shown in the equatorial region. The bottom image **c.)** is the difference between the two to show what regions are near 0 km, which indicates isostatic crust. The scale here ranges from -10 km to 5 km, showing significant thickness deviance from 0 km, thus the degree-2 structure contributes a significant non-isostatic component to the crustal field. (Please refer to section 3.7.1 for more detail). These models were generated using an average crustal density of 2900 kg/m^3 and an average mantle density of 3500 kg/m^3.

Figure 3.17

a. Non-isostatic thickness generated at lmax = 50

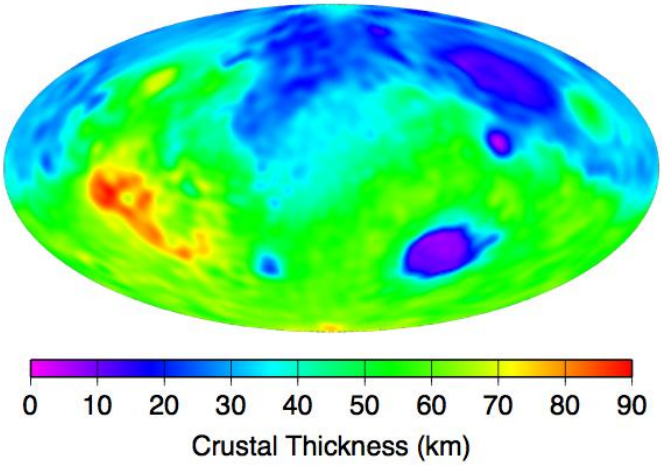

b. Isostatic thickness generated at lmax = 50

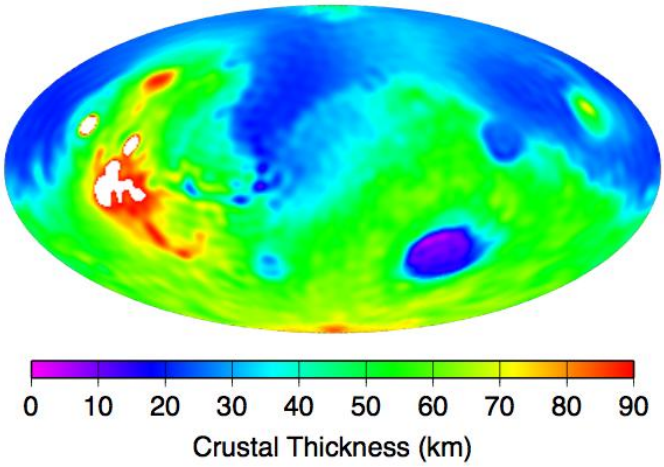

c. Difference between non-isostatic and isostatic thickness

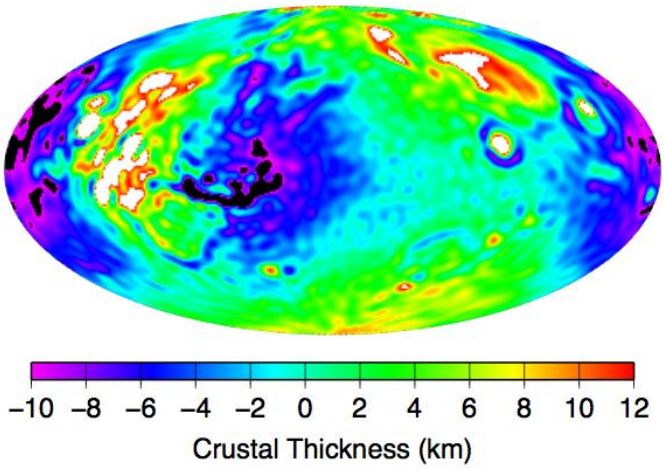

Figure 3.17 (con't.)

Crustal thickness models generated at lmax = 50. The top image **a.)** is the non-isostatic crustal thickness model generated from the Mars Crustal Thickness code, while the middle image **b.)** is the Airy-isostatic crustal thickness model generated from the MarsIsostacy code. Both models have a mean crustal thickness of 44.88 km, as shown in the equatorial region. See how the thickness difference between non-isostatic and isostatic features a large degree-2, order-2 structure and how that resembles the difference plot made with lmax = 2, indicating that the underlying difference between whether the planet is isostatic or not is mainly contributed by this degree-2 structure. This structure very much resembles a giant impact located over Valles Marineris, just east of the Tharsis Rise region. These models were generated using an average crustal density of 2900 kg/m^3 and an average mantle density of 3500 kg/m^3.

Chapter 4: Conclusions

4.1 The Non-Uniqueness of Gravity

Given that density structures derived from gravity studies are non-unique, numerous crustal thickness maps can generate the same gravity signature without imposing additional constraint. In this study, I assumed the crust to be uniform in composition while relying on geological assumptions about how much crustal material has to be generated (minimum crustal thickness) or the types of tectonic processes or deformation that goes into the process to constrain the average crustal thickness. Regardless of these considerations, the spatial pattern does not change, meaning that this method of using topography and gravity data to study crustal and mantle dynamics is not well-constrained. The experiments in this study can only reveal so much as to how changing the assumed crustal thickness, crustal and mantle densities, and spherical harmonic degree can affect the overall resulting average crustal thickness. Because the spatial patterns of the revealed structures do not necessarily change when these parameters are altered, many of these crustal thickness models can give the same patterns, thus not pinpointing to which set of criteria really helped make up those structures. Using gravity and topography data to infer about the interior of a planet is useful to a certain point, when seismic data is not available.

4.2 The Problem with Degree-1 and Degree-2

4.2.1 Degree-1

As discussed throughout this study, Mars is characterized by a very significant spherical harmonic degree-1, order-0 topographic dichotomy structure. Table 4.1 compares the spherical harmonic coefficients for the first few degrees and orders for Earth, the Moon, Venus, and Mars. The table shows that the coefficient for degree-1, order-0 for Mars is -1735.5 m, which is significantly larger than the same degree-1, order-0 coefficient of the other terrestrial bodies listed. This means that Mars is truly

divided into two distinctive hemispheres of different crustal thicknesses. It is interesting to compare this to the Moon's degree-1, order-1 coefficient. In the case of the Moon, the body is also divided into two hemispheres, but unlike Mars, it is divided into a thinner and thicker crust orienting East-West hemispheres as opposed to Mars' North-South hemispheres. So what exactly is the crustal dichotomy? Why is the planet divided into one hemisphere of thicker crust while the other hemisphere has thinner crust? I have proposed a couple hypothesis in Chapter 3 regarding a mantle plume track that may have contributed to thickening of the Southern hemisphere. I have also followed other studies in suggesting a possible large-scale impact in the Northern Lowlands that may have thinned the crust in the Northern hemisphere. But because the corresponding degree-1, order-0 gravitational potential is zero, given the choice of the center-of-mass coordinate system, it is hard to deduce what the crustal dichotomy really is, if basing it only on crustal thickness modeling because it has limited constraint.

4.2.2 Degree-2

Shown in Table 4.1 and the discussion in this work, the degree-2, order-0 coefficient of Mars (-5966.19 m) contains a very large rotational component, but there is also a non-rotational component in this coefficient as well. Thus the entire coefficient cannot just be removed to correct for the rotational component, because in doing so the residual component that is non-rotational will also be removed and that will give an inaccurate resulting crustal thickness, which could lead to misinterpretation. Various similar studies working with these coefficients all have no great consensus as to what to do about this degree-2, order-0 component. Wieczorek (2007) removed all of degree-2, order-0 term from topography in his work, while Neumann et al. (2004) plot their topography relative to the geoid, which has a major degree-2, order-0 component. The problem here is: which surface should be the reference -- a hydrostatic ellipsoid surface or a non-hydrostatic geoid surface including the J_2 rotational flattening term? The shape and gravity of Mars is deduced from satellite data, not inferred from hydrostatic equilibrium. If one assumes the planet to be in hydrostatic equilibrium, a correction can be made, but in order to do that correctly, the radial density structure of the planet has to

be known (Chambat et al., 2010). Because Mars is considered to be a one-plate, stagnant-lid planet, the principle of hydrostatic equilibrium may not be applicable. If hydrostatic equilibrium was applied on Mars, there is still a major problem in the fact that there is a lack of knowledge about the size of the core and the mantle density structure. Thus, this degree-2, order-0 component remains the biggest problem in modeling and understanding the interior structure of Mars.

Table 4.1 Spherical Harmonic Coefficients of the Terrestrial Bodies (except Mercury) for the first two spherical harmonic degrees. These are from various topographic shape files obtained from Mark Wieczorek's website: http://www.ipgp.fr/~wieczor/SH/SH.html.

Degree	Order	Spherical Harmonic Coefficients (meters)			
		Earth[1]	Moon[2]	Venus[3]	Mars[4]
0	0	6368637.46	1737025.82	6051877.34	3389500.12
1	0	648.73	147.49	-6.12	-1735.55
1	1	609.47	-985.04	-116.30	-101.16
2	0	-5805.81	-705.98	-163.80	-5966.19
2	1	332.98	-778.07	94.24	222.25
2	2	-418.17	85.38	-134.54	-1060.12

From shape files: [1]srtmp2160.shape, [2]ULCN359_lpo.shape, [3]VenusTopo719.shape, and [4]MarsTopo719.shape.

4.3 Future Work

There are many extensive seismological studies conducted on Earth that give us additional constraints on the interior of our planet. Because there is no seismic instrument on Mars, we have absolutely no seismic data of that planet, thus everything we know of Mars' interior all comes from geophysical modeling, density values from

meteorites assumed to have come from Mars, and geophysical inferences of the crust based on topographic loading from surface topography. There is no doubt that a complete picture of the interior of the planet cannot be possible without the use of seismic data. Although SHARAD (Shallow Subsurface Radar), a ground penetrating radar instrument on MRO (Mars Reconnaissance Orbiter) had been used on the polar ice caps and various regions on Mars, those data were limited to mostly the polar ice regions with signals reaching to only a few hundred meters (Seu et al., 2007) and up to 1 km under the crust (Carter et al., 2009). For larger-scale studies of the crust-mantle boundary and a more precise estimate of the radius of the core, such an instrument is not useful.

Currently, NASA has a spacecraft mission under review that will be able to perform tasks and experiments to probe the interior of Mars. The Geophysical Monitoring Station (GEMS) is the mission under review that will have three main instruments to perform in-situ measurements of Mars' interior (Banerdt et al., 2010). These instruments include a seismometer to investigate the interior layers of Mars including the core and mantle, a heat flow instrument that will measure the heat flux out of the planet, and a rotation and interior structure experiment that will measure the precession of the planet, which will help with geodesy studies (Dehant et al., 2011). This mission will solve the greatest, fundamental mysteries that the experiments in this study cannot explain. The geophysical modeling of Mars in this study using topography and gravity data only scratches the surface, but a lot is still unknown. If this proposed mission gets approved, a tremendous amount of data will be available for future studies, paving the way for exciting new findings and discoveries that will finally reveal the interior of Mars.

References

Acuna, M. H. et al. (1999). Global Distribution of Crustal Magnetization Discovered by the Mars Global Surveyor MAG/ER Experiment. *Science*, Vol. 284, 790-793.

Andrews-Hanna, J. C., M. T. Zuber, and W. B. Banerdt (2008). The Borealis basin and the origin of the martian crustal dichotomy. *Nature*, Vol. 453, doi: 10.1038/nature07011, 1212-1215.

Banerdt, B. et al. (2010). Geophysical Monitoring Station (GEMS): A Discovery-Class Mission to Explore the Interior of Mars. *American Geophysical Union, Fall Meeting 2010*, abstract #DI43A-1938.

Barlow, N. G. (2008). *Mars: An Introduction to its Interior, Surface and Atmosphere*, 264 pp., Cambridge University Press, New York.

Bertka, C. M. and Y. Fei (1998). Density profile of an SNC model Martian interior and the moment-of-inertia factor of Mars. *Earth and Planetary Science Letters*, Vol. 157, 79-88.

Blakely, R. J. (1996). *Potential Theory in Gravity & Magnetic Applications*, 441 pp., Cambridge University Press, New York.

Canup, R. M. and E. Asphaug (2001). Origin of the Moon in a giant impact crater near the end of the Earth's formation. *Nature*, Vol. 412, 708-712.

Carr, M. (2006). *The Surface of Mars*, 306 pp., Cambridge University Press, New York.

Carter, L. M. et al. (2009). Shallow Radar (SHARAD) sounding observations of the Medusae Fossil Formation, Mars. *Icarus*, Vol. 199, 295-302.

Chambat, F., Y. Ricard, and B. Valette (2010). Flattening of the Earth: further from hydrostaticity than previously estimated. *Geophysical Journal International*, Vol. 183, 727-732.

Dehant, V. et al. (2011). Geodesy on GEMS (GEophysical Monitoring Station). *EPSC Abstracts*, Vol. 6, EPSC-DPS2011-1551.

Dreibus, G. and H. Wanke (1985). Mars, a Volatile-Rich Planet. *Meteoritics*,Vol. 20, Issue 2, 367-381.

Elkins-Tanton, L. T., P. C. Hess, and E. M. Parmentier (2005). Possible formation of ancient crust on Mars through magma ocean processes. *Journal of Geophysical Research*, Vol. 110, E12S01, doi: 10.1029/2005JE002480.

Francis, P. and C. Oppenheimer (2004). Extraterrestrial volcanoes, p. 397-403 in *Volcanoes*, 2nd ed., 521 pp., Oxford University Press, New York.

Frey, H. and R. A. Schultz (1988). Large impact basins and the mega-impact origin for the crustal dichotomy on Mars. *Geophysical Research Letters*, Vol. 15, 229-232.

Frey, H. V. et al. (2002). Ancient lowlands on Mars. *Geophysical Research Letters*, Vol. 29, no. 10, 1384.

Goettel, K. A. (1981). Density of the Mantle of Mars. *Geophysical Research Letters*, Vol. 8, No. 5, 497-500.

Hartmann, W. K. and G.Neukum (2001). Cratering chronology and the evolution of Mars. *Space Science Review*, Vol. 96, 165-194.

Hynek, B. M. et al. (2011). Geological evidence for a migrating Tharsis plume on early Mars. *Earth and Planetary Science Letters*, Vol. 310, 327-333.

Kiefer, W. S. (2003). Melting in the martian mantle: Shergottite formation and implications for present-day mantle convection on Mars. *Meteoritics & Planetary Science*, Vol. 39, Nr 12, 1815-1832.

Marinova, M. M., O. Aharonson, and E. Asphaug (2008). Mega-impact formation of the Mars hemispheric dichotomy. *Nature*, Vol. 453, doi:10:1038/nature07070, 1216-1219.

McGovern, P. J., et al. (2002). Localized gravity/topography admittance and correlation spectra on Mars: Implications for regional and global evolution. *Journal of Geophysical Research*, Vol. 107(E12), 5136, doi: 10.1029/2002JE001854.

McKenzie, D., D. N. Barnett, and D. N. Yuan (2002). The relationship between Martian gravity and topography. *Earth and Planetary Science Letters*, Vol. 195, 1-16.

McSween, H. Y. (1985). SNC Meteorites: Clues to Martian Petrologic Evolution? *Reviews of Geophysics*, Vol. 23, No. 4, 391-416.

Neumann, G. A. et al. (2004). Crustal structure of Mars from gravity and topography. *Journal of Geophysical Research*, Vol. 109, E08002, doi: 10.1029/2004JE002262.

Nimmo, F., S. D. Hart, D. G. Korycansky, and C. B. Agnor (2008). Implications of an impact origin for the martian hemispheric dichotomy. *Nature*, Vol. 453, doi:10.1038/nature07025, 1220-1223.

Nunes, D. C., Smrekar, S. E., and A. Konopliv (2009). Survey of Gravity Admittance for Mars from the High-Resolution Mars Reconnaissance Orbiter Data. *Lunar Planetary Science Conference XXXX, abstract #2011.*

Phillips, R. J. et al. (2001). Ancient Geodynamics and Global-Scale Hydrology on Mars. *Science*, Vol. 291, 2587-2591.

Rapp (1989). The decay of the spectrum of the gravitational potential and the topography for the Earth. *Geophysical Journal International*, Vol. 99, 449-455.

Roberts, J. H. and S. Zhong (2006). Degree-1 convection in the Martian mantle and the origin of the hemispheric dichotomy. *Journal of Geophysical Research*, Vol. 111, E06013, doi: 10.1029/2005JE002668.

Roberts, J. H. and S. Zhong (2007). The cause for the north-south orientation of the crustal dichotomy and the equatorial location of Tharsis on Mars. *Icarus*, Vol. 190, 24-31.

Seu, R. et al. (2007). The SHAllow RADar (SHARAD) Experiment, a subsurface sounding radar for MRO. *Memoire della Supplementi, Societa Astronomica Italiana*, Vol. 11, 26-36.

Sohl, F. and T. Spohn (1997). The interior structure of Mars: Implications from SNC meteorites. *Journal of Geophysical Research*, Vol. 102, No. E1, 1613-1635.

Solomon, S. C. et al. (2005). New Perspectives on Ancient Mars. *Science*, Vol. 307, 1214-1220.

Sramek, O. and S. Zhong (2010). Long-wavelength stagnant lid convection with hemispheric variation in lithospheric thickness: Link between Martian crustal dichotomy and Tharsis? *Journal of Geophysical Research*, Vol. 115, E09010, doi: 1029/2010JE003597.

Sramek, O. and S. Zhong (2012). Martian crustal dichotomy and Tharsis formation by partial melting coupled to early plume migration. *Journal of Geophysical Research*, Vol. 117, E01005, doi: 10.1029/2011JE003867.

Smith, D. E. et al. (1998). Investigation overview and first results from the Mars Orbiter Laser Altimeter. *Lunar Planetary Science Conference XXIX, abstract #1682.*

Smith, D. E. et al. (1999a). The Global Topography of Mars and Implications for Surface Evolution. *Science*, Vol. 284, 1495-1503.

Smith, D. E. et al. (1999b). The Gravity Field of Mars: Results from Mars Global Surveyor. *Science*, Vol. 286, 94-97.

Smith, D. E. et al. (2001). Mars Orbiter Laser Altimeter: Experiment summary after the first year of global mapping of Mars. *Journal of Geophysical Research*, Vol. 106, No. E10, 23689-23722.

Stevenson, D. J. (2001). Mars' core and magnetism. *Nature*, Vol. 412, Issue 6843, 214-219.

Tanaka, K. L. (1986). The Stratigraphy of Mars. *Journal of Geophysical Research*, Vol. 91, No. B13, E139-E158.

Turcotte, D. L. and G.Schubert (2002). *Geodynamics*, 2nd ed., 456 pp., Cambridge University Press, New York.

Tyler, G. L. et al. (1992). Radio Science Investigations with Mars Observer. *Journal of Geophysical Research*, Vol. 97, No. E5, 7759-7779.

Wahr, J. (1996). *Geodesy and Gravity,Class Notes*, 294 pp., Samizdat Press, Golden, Colorado.

Wieczorek, M. A. (2007). Gravity and Topography of the Terrestrial Planets, in *Treatise on Geophysics*, T. Spohn and G. Schubert (eds.), Vol. 10, 165-206, Elsevier.

Wieczorek, M. A. and R. J. Phillips (1998). Potential anomalies on a sphere: Applications to the thickness of the lunar crust. *Journal of Geophysical Research*, Vol. 103, No. E1, 1715-1724.

Wieczorek, M. A. and M. T. Zuber (2004). The thickness of the Martian crust: Improved constraints from geoid-to-topography ratios. *Journal of Geophysical Research*, Vol. 109(E1), E01009, doi: 10.1029/2003JE002153.

Wilhelms, D. E. and S. W. Squyres (1984). The martian hemispheric dichotomy may be due to a giant impact. *Nature*, Vol. 309, 138-140.

Zhong, S. (2009). Migration of Tharsis volcanism on Mars caused by differential rotation of the lithosphere. *Nature Geoscience*, Vol. 2, doi: 10.1038/NGEO392, 19-23.

Zhong, S. and M. T. Zuber (2001). Degree-1 mantle convection and the crustal dichotomy on Mars. *Earth and Planetary Science Letters*, 189, 75-84.

Zuber, M. T. (2001). The crust and mantle of Mars. *Nature*, Vol. 412, 220-227.

Zuber, M. T. et al. (1992). The Mars Observer Laser Altimeter Investigation. *Journal of Geophysical Research*, Vol. 97, No. E5, 7781-7797.

Zuber, M. T. et al. (2000). Internal Structure and Early Thermal Evolution of Mars from Mars Global Surveyor Topography and Gravity. *Science*, Vol. 287, 1788-1793.

Zuber, M. T. et al. (2004). An improved model of the crustal structure of Mars. *Lunar Planetary Science Conference XXXV, abstract #1827.*